LONG TERM TRENDS IN THE NORTHERN INDIAN OCEAN CYCLONES; A REANALYSIS ON FAVOURING MECHANISMS AND ITS IMPACTS ON BIOLOGICAL PRODUCTION

by

AKSHAYA C

(2016-20-022)

THESIS

Submitted in partial fulfilment of the

requirements for the degree of

B.Sc. – M.Sc. (Integrated) Climate Change Adaptation

Faculty of Agriculture

Kerala Agricultural University

COLLEGE OF CLIMATE CHANGE AND ENVIRONMENTAL SCIENCE

KERALA AGRICULTURAL UNIVERSITY

VELLANIKKARA, THRISSUR – 680656

KERALA, INDIA

2021

DECLARATION

I, Akshaya, C. (2016-20-022) hereby declare that this thesis entitled **"LONG TERM TRENDS IN THE NORTHERN INDIAN OCEAN CYCLONES; A REANALYSIS ON FAVOURING MECHANISMS AND ITS IMPACTS ON BIOLOGICAL PRODUCTION "** is a bonafide record of research work done by me during the course of research and the thesis has not previously formed the basis for the award to me of any degree, diploma, associateship, fellowship or other similar title, of any other University or Society.

Place: Vellanikkara Akshaya C

Date: (2016-20-022)

CERTIFICATE

Certified that this thesis entitled **"LONG TERM TRENDS IN THE NORTHERN INDIAN OCEAN CYCLONES; A REANALYSIS ON FAVOURING MECHANISMS AND ITS IMPACTS ON BIOLOGICAL PRODUCTION"** is a record of research work done independently by AKSHAYA C (2016-20-022) under my guidance and supervision and that it has not previously formed the basis for the award of any degree, diploma, fellowship or associateship to her.

Place: Vellanikkara

Date:

Mr. Muraleedharan K.R.

Principal Scientist

Physical Oceanography Department

CSIR-National Institute of Oceanography

Regional Center, Kochi

Ernakulam-682018

CERTIFICATE

We, the undersigned members of the advisory committee of Miss Akshaya, C., (2016-20-022) a candidate for the degree of the **B.Sc - M.Sc (Integrated) Climate Change Adaptation** agree that the thesis entitled **"Long Term Trends in the Northern Indian Ocean Cyclones; A Reanalysis on Favouring Mechanisms and its Impacts on Biological Production"** may be submitted by Miss Akshaya, C. (2016-20-022), in partial fulfilment of the requirement of the degree.

Mr. Muraleedharan K.R.
Principal Scientist
Physical Oceanography Department
CSIR-National Institute of
Oceanography (NIO)
Regional Center, Kochi
Ernakulam-682018

Dr. P. O. Nameer
Dean
College of Climate Change and
Environmental Science
Kerala Agricultural University
Vellanikkara
Thrissur

Dr. Madhu N.V.
Senior Scientist
CSIR-National Institute of
Oceanography (NIO)
Regional Center, Kochi
Ernakulam-682018

Dr. Phiros Shah
Assistant Professor
Kerala University of Fisheries
and Ocean Studies (KUFOS)
Panangad
Ernakulam-682506

(EXTERNAL EXAMINER)

ACKNOWLEDGEMENT

Over the five years of my journey in Kerala Agricultural University. I have been supported and encouraged by many people. First and Foremost I would like to express my sincere gratitude and obligation to ***Mr. Muraleedharan K.R.,*** *Principal Scientist, Physical Oceanography Department, CSIR-National Institute of Oceanography (NIO), Regional Centre (RC), Kochi, and my mentor, for his sincere guidance, motivation, patience and unconditional support, which enabled me to complete my M.Sc thesis work successfully.*

I would like to convey my sincere gratitude to my advisory committee members, ***Dr. P.O. Nameer****, Dean, College of Climate Change and Environmental Science (CCCES), KAU,* ***Dr. Madhu N.V****., Senior Scientist, NIO-RC, Kochi, and* ***Dr. Phiros Shah****, Assistant Professor, Kerala University of Fisheries and Ocean Studies for sparing their valuable time to help me conduct my thesis smoothly and for their constant encouragement.*

I express my heartfelt thanks to ***Mr. Ravikumar C. Nair****, Project Associate, NIO for being my unofficial mentor and helping me to complete my thesis on time with his constant support and guidance. I would also like to thank* ***Mr. Abdul Azeez S****., Project Associate, NIO-RC, Kochi,* ***Ms.Parvathy V. S*** *and* ***Miss. Jenix*** *(CCCES) for their valuable help and guidance.*

I am also extremely thankful to my friends ***Aiswarya Soji Joseph****,* ***Akshara T, Aswathykrishna P.N, Greeshma Saju, Gopika Gopi, and, Smrithy M.G****. and all my classmates for constant encouragement and physical and mental help during my tough times.*

I am grateful to ***College of Climate Change and Environmental Science*** *for providing me opportunity to undertake this work. I would like to thank all teaching and non-teaching staffs for their support especially* ***Ms. Krishnapriya C.B*** *and* ***Mr. Jineesh V. K****.*

Last but not least, I want to thank my ***parents, and my brother*** *for being my pillars of support and inspiration during my study.*

A sincere apology to those I have not personally thanked, and a heartfelt thank you to everyone who assisted in the successful completion of my study.

Above all I worship the ***almighty*** *for the blessings and providing strength during for successful completion of work.*

Akshaya C

TABLE OF CONTENTS

LIST OF FIGURES

SYMBOLS AND ABBREVATIONS

AGGI	Annual Greenhouse Gas Index
APDRC	Asia-Pacific Data Research Centre
AS	Arabian Sea
BoB	Bay of Bengal
CS	Cyclonic Storm
D	Depression
DD	Deep Depression
DMI	Dipole Mode Index
ECMWF	European Centre for Medium-Range Weather Forecast
EIO	Equatorial Indian Ocean
ENSO	El Nino Southern Oscillation
EPV	Ekman Pumping Velocity
ESCS	Extremely Severe Cyclonic Storm
HadISST	Hadley Centre Global Sea Ice and Sea Surface Temperature
IMD	Indian Meteorological Department
IO	Indian Ocean
IOD	Indian Ocean Dipole
IPCC	Intergovernmental Panel on Climate Change
JTWC	Joint Typhoon Warning Centre
L	Low Pressure Area
LHF	Latent Heat Flux
MLD	Mixed Layer Depth
MJO	Madden Julian Oscillation
MODIS	Moderate-resolution Imaging Spectroradiometer
NHF	Net Heat Flux
NIO	Northern Indian Ocean
NOAA	National Oceanic and Atmospheric Administration
NPP	Net Primary Productivity

ONI	Oceanic Nino Index
PAR	Photosynthetically Active Radiation
SCS	Severe Cyclonic Storm
SH	Specific Humidity
SHF	Sensible Heat Flux
SLHF	Surface Latent Heat Flux
SOI	Southern Oscillation Index
SSHF	Surface Sensible Heat Flux
SST	Sea Surface Temperature
SSTA	Sea Surface Temperature Anomaly
SuCS	Super Cyclonic Storm
TCG	Tropical Cyclone Genesis
TP	Total Precipitation
VGPM	Vertically Generalized Production Model
VSCS	Very Severe Cyclonic Storm
VWS	Vertical Wind Shear
WOA	World Ocean Atlas

CHAPTER 1

INTRODUCTION

The tropical cyclone is one of the most devastating weather phenomena that have adverse impacts on the locale's society, economy, environment, and human well-being. It is the generic term for a non-frontal synoptic-scale, low-pressure system originating over the tropical or subtropical waters with organized convection and definite cyclonic surface wind circulation (Bhaskar Rao *et al.,*2019). One of the imperative elements responsible for developing tropical cyclones is high Sea Surface Temperature (SST) which should be higher than 26.5 ^{o}C (Bhardwaj and Singh, 2019). The tropical cyclones with wind speed lower than 17 ms^{-1} are termed tropical depressions, and those with windspeed smaller than 33ms^{-1} are termed tropical storms (Montgomery and Farrell, 1993). The latent heat liberated by condensation of the water vapor strengthens the tropical cyclones (Bhardwaj and Singh, 2019). Certain environmental conditions have to exist before cyclogenesis and further development. The upper-ocean water must be warm with at least 26.5 ^{o}C through a depth of 50 meters to power the tropical cyclone heat engine. There must be an atmosphere where the temperature drops quickly with height, which is unstable to moist convection. The heat accumulated in the ocean is delivered in the advancement of tropical cyclones by precipitating convection, which generally holds the form of thunderstorm complexes. The mid-troposphere must be comparatively moist, and the dry middle levels make it complex for widespread thunderstorm activity to intensify. There should be a least possible distance of 500 kilometres from the equator because the presence of a sufficient amount of Coriolis force must be there for near-gradient wind equilibrium to form tropical cyclogenesis. There must be a near-surface disturbance with ample vorticity and convergence that already exists. For a tropical cyclone to be developed, they desire a poorly organized system with ample spin and low-level inflow. Vertical Wind Shear (VWS) between the surface of the ocean and upper troposphere should be less than 10ms^{-1}. Large VWS interrupts a developing cyclone and counter its genesis. It can dwindle or exterminate that has already

developed by hindering the deep convection around the centre of the cyclone (Landsea,2000).

The ancient evidence affirms that globally, around 80-90 Tropical cyclones appear annually (Bhardwaj and Singh, 2019). Northern Indian Ocean (NIO) has 2 dominant tropical seasons, and they are most active during the post-monsoon season (October-November) and pre-monsoon season (April-May) (Balaguru *et al.*, 2014). In the Bay of Bengal (BoB), the post-monsoon season cyclones during October and November are particularly devastating (Singh,2007). BoB witnesses Tropical Cyclones all over the year, with nominal recurrence in December-February and with a maximum frequency in April-May and October-November (Sarma *et al.,* 2019). The NIO accounts for 7% of global tropical cyclones, and approximately 80% of NIO tropical cyclones appear in the BoB (Bhardwaj and Singh, 2019). Even though the frequency of Tropical Cyclones in NIO is very low, an energetic Tropical Cyclone in this area might be extremely lethal due to its adjacency to massively populated areas (Kikuchi and Wang, 2010). Studies reveal an increasing trend in SST over the global ocean basin with the highest rate in the NIO (Sebastian and Behera,2015).

The east coast of India, Sri Lanka, Bangladesh and Myanmar coasts are exposed to severe post-monsoon season cyclones (Singh,2007). Fourth Assessment Report of Intergovernmental Panel on Climate Change wrapped up that the global temperature has risen over the past half-century due to enhancement in greenhouse gas concentration. This was further reinforced by the US Climate Change Science Program 3.3 report (Knutson *et al.,* 2010). SST is a crucial physical property that helps to figure out features like current flows, precipitation, biological production, surface air properties, upwelling etc (Dinesh Kumar *et al.*, 2016). Over the past few decades, SST in most cyclone development regions has risen by several tenths of a Degree Celsius (Knutson *et al.,* 2010). Tropical cyclones are likely to be more frequent and severe in this warming scenario (Byju and Prasanna Kumar, 2011). There is a rising concern that the increase in sea level due to global warming would augment the risk of flooding of coastal regions as tropical cyclones become more

frequent (Singh *et al.,* 2000*).* According to an extensively accepted thermodynamic approach, the cyclone is a natural Carnot engine that procures energy from a warm tropical ocean (Sebastian and Behera,2015). Studies acknowledge that later in 1950, over the Southern sector of the BoB, there was a substantial boost in the amount of Severe Cyclonic Storms (SCS) at the time of the post-monsoon season. Over the BoB, there is a considerable decrement in the rate of dissipation of SCS. To form SCS, comparatively high SST (28-30^{o}C) with a thermodynamically unstable atmosphere and weak tropospheric wind shear was required (Mahala *et al.*, 2015). The intensification of tropical cyclones comprises multiple mechanisms, including atmospheric circulation, upper ocean interactions and Tropical Cyclone dynamics. Due to the intricacy and errors generated in the track forecasting of Tropical cyclones and are rendered to the intensity prediction, the definiteness of the intensity prediction has trailed behind the tropical cyclone tracking (Goni *et al.*, 2009). Elevated ocean heat content contributes a steady and continual source of sensible and latent heat fluxes to the atmosphere from the surface of the ocean, which aids in the intensification of cyclones (Deshpande *et al*., 2021)

El Nino Southern Oscillation (ENSO) is a coupled air-sea interaction phenomenon that has been the driving factor of interannual climatic variability. Through Atmospheric and Oceanic teleconnections, ENSO variability induces anomalous SST over the Indian Ocean (Singh *et al.,* 2013). During the El Nino years, cooling is recorded throughout most regions of the Indian Ocean in the winter season. The SST levels are seen as the first signs of warming during the pre-monsoon season. All along the monsoon season, progressive warming is noticed, and in the time of the post-monsoon season, warming is predominant over most parts of the Indian Ocean. Throughout La Nina years, significant warming is recorded over the Indian Ocean during the winter season. In the interim of the pre-monsoon season, the spatial extent of warming was recorded to decrease gradually. During monsoon, there is a gradual decrement in SST values and the course of the post-monsoon season, there is a significant cooling trend (Medha Khole, 2003).

Tropical cyclone activity in the NIO is also altered due to interannual climate variabilities such as El-Nino Southern Oscillation (ENSO) and Indian Ocean Dipole (IOD) (Aneesh and Sijikumar, 2018). ENSO and IOD have long-reaching effects that stretch far apart from the basins they emerged, namely Tropical Pacific and the Indian Ocean, respectively (Mahala *et al.*, 2015). In virtue of changes in atmospheric circulation, the El Nino induces abnormal warming, whereas La Nina induces anomalous cooling over the Tropical Indian Ocean (Aneesh and Sijikumar, 2018). ENSO events endure about 12-18 months and happen every 2-7 years with a wide intensity range (Mahala *et al.*, 2015). According to researchers, large-scale parameters associated with tropical cyclones are less conducive in BoB for the cyclone development amid El Nino and the situation overturn during La Nina (Sattar and Cheung, 2019). Considering the influence of IOD, the frequency of tropical cyclones is highest during years with negative IOD and years with no IOD (Mahala *et al.*, 2015mah). The positive phase of IOD is characterized by anomalous cooling in the Tropical Eastern Indian Ocean and anomalous warming in the Tropical Western Indian Ocean. However, the negative phase of IOD is characterized by anomalous cooling in the Tropical Western Indian Ocean and anomalous warming in the Tropical Eastern Indian Ocean (Girishkumar and Ravichandran, 2012). With a substantial east-west gradient in the sea surface temperature along the equator, the dipole mode attains its peak phase by October-November (Chowdary and Gnanaseelan, 2007). Conforming to research, later 1970 most of the El Nino episodes appear with IOD events, and practically all positive IOD occurs with El Nino years and also in comparison to La Nina and neutral ENSO years, the average lifetime of a Tropical Cyclone is lesser over El Nino years (Mahala *et al.*, 2015). Heat content anomaly is negative in the Western Indian Ocean and positive in the Eastern Indian Ocean while El Nino only years, nevertheless it is antagonistic in IOD only and co-occurrence years (Chowdary and Gnanaseelan, 2007). According to Mahala *et al.* (2015), tropical cyclone activity in the BoB (warm phase of ENSO) was found to decrease during November and May, and it implies that the extreme tropical cyclone cases are higher all along the years of positive IOD, followed by the years of negative IOD and no IOD years.

The air-sea interaction influences the flow of the environment that further modulates the tropical cyclone activity. The air-sea contact is the prerequisite for the advancement of tropical cyclones, and the warmth transported to the atmosphere from the ocean is the major energy source of tropical cyclones (Yuan and Cao, 2013). Human-induced changes in climate bring about an increase in the sea surface temperature, which can improve the severity of the cyclones (Krishna, 2009). In a world with double the amount of carbon dioxide, researchers discovered an increase in the intensity and frequency of Tropical Cyclones in the NIO. Contrarily, some research revealed a considerable decrease in the frequency of BoB Tropical Cyclones during monsoon season, despite the rising SST in recent times (Ng and Chan, 2012).

The earth's environmental system relies heavily on the primary production from the ocean because the phytoplankton generates 50% of the oxygen for the world and further is the foundation of the ocean's food web (Lin *et al*., 2003). Even though the Tropical Cyclones are recognized for wrecking life and properties onshore, they frequently enhance marine life by transporting the nutrients towards the euphotic zone (Byju and Prasanna Kumar, 2011; Lin *et al*., 2003). The nutrient-rich water is carried to the euphotic zone relying upon the storm's power and is used by the phytoplankton that promotes the primary production (Maneesha *et al*., 2021). As a result of strong stratification induced by river water influx, the BoB is considered as a low biologically productive zone, while the AS is found to be a high biologically productive zone (Kuttippurath *et al*., 2021). Primary Production is supported by phytoplankton or planktonic algae, whereas secondary and tertiary production is supported by zooplankton and fish correspondingly (Qasim, 1977). The upward transport of nutrients from the subsurface via the wind stress curl was the process that enabled higher biological production, and cold nutrient-rich water that reached the top ocean through upward Ekman pumping was rich in carbon dioxide (Byju and Prasanna Kumar, 2011). As per analyses, extended storm passage time introduces increased blooms of phytoplankton. Although if there is entrainment of nutrients to the surface water, the bloom is influenced by the accessibility of the light. The solar energy spectrum within 400nm and 700 nm is

the Photosynthetically Active Radiation (PAR), which the photosynthetic organisms can utilize for photosynthesis and the cloud/ water vapor have a great influence on its value. The strong mixing and upwelling provoked by the cyclones generally elevate the chlorophyll concentration either by supplying nutrients to the upper layer or directly mixing up the previously existing deep chlorophyll (Chacko 2017). Nitrogen is the major nutrient element limiting phytoplankton biomass throughout most world oceans (Falkowski, 1994). Another important biochemical factor supporting the growth of the phytoplankton is light, and the euphotic zone is the region where most of the chlorophyll-a is concentrated. In principle, the euphotic zone and nutrients can be influenced by a physical process, especially after the passage of tropical cyclones (Zhao, H., & Wang, Y. 2018; Liang et al., 2018). The intake of carbon dioxide, a significant greenhouse gas that is one of the key sources of anthropogenic and natural climate change, is often influenced by the ocean's primary production (Lin *et al*., 2003).

The main objective of this study is to analyze the long-term trends in the SST over the NIO. The variations in SST were analyzed from 1900 to 2020. The study also focuses on the long-term trend in the frequency of NIO Tropical Cyclones and its occurrence at the time of El Nino, La Nina and IOD events from 1900-2020, and the impacts of Tropical Cyclones on the primary production of NIO was also examined.

The objectives of the study are:

i. to study the long-term variability of Sea Surface Temperature
ii. to analyze the long-term trend in cyclogenesis, their intensification and its connection with El Nino, La Nina and Indian Ocean Dipole (IOD) events
iii. to quantify the biological production and their carbon fixation due to the tropical cyclones in the Northern Indian Ocean

CHAPTER 2

REVIEW OF LITERATURE

Tropical Cyclones

Tropical Cyclones are one of the world's most interesting meteorological phenomena that have a major capacity to control the weather and climate of tropical countries (Singh *et al.*, 2000). A Tropical Cyclone emerges over Tropical Oceans and is fuelled by ocean heat transfer. After the generation of the storm, it advances westward and to some extent poleward with the speed of 2-10ms^{-1}. Just as they progress over cold water or land surface, they dissipate promptly, nonetheless over warm water, they disperse under disadvantageous atmospheric wind systems interactions (Kerry Emanuel, 2003). A mature Tropical Cyclone has quite a warm core vertical circulation that seems to be anticyclonic in the upper troposphere, and it is found to be cyclonic in the lower troposphere. Winds and precipitation are particularly energetic in the core region (Frank, 1977). Eyes or essentially cloud-free parts of the storm are witnessed in well-developed Tropical Cyclones. The air in the eyes steadily subsides at a rate of 5-10cms^{-1} and all along with the accelerated intensification of the storm, the air might diminish expeditiously. Although some reasonably intense storms miss defined eyes, and weaker ones hardly comprise them, the eyes are most commonly encountered in storms with maximum wind speeds. The eyewall is the band of deep convective clouds that spread 20-50km outward the eye, where the maximum up-flow occurs. Spiral Rainbands are bands of cumulus clouds that coil towards the storm centre that at times meet the eyewall, which are tens of kilometres and are usually raining (Kerry Emanuel, 2003).

India Meteorological Department classified cyclonic disturbances in the NIO depending on their maximum sustained wind speed

Weather System	**Maximum Sustained Surface Wind Speed in kmph (knots)**

Low Pressure Area(L)	Less than 31(<17)
Depression(D)	31-49 (17-27)
Deep Depression (DD)	50-61 (28-33)
Cyclonic Storm (CS)	62-88 (34-47)
Severe Cyclonic Storm (SCS)	89-117 (48-63)
Very Severe Cyclonic Storm (VSCS)	118-166 (64-89)
Extremely Severe Cyclonic Storm (ESCS)	167-221 (90-119)
Super Cyclonic Storm (SuCS)	Greater than or equal to 222 (≥120)

Tropical Cyclones and Climate Change

Globally from the 1950s, the elevated temperature generated an upsurge in climate and weather extremes, including sea-level rise, alterations in wind patterns, precipitation, and shift in global monsoon systems, thawing of glaciers and sea ice, ocean acidification with changes in marine and terrestrial ecosystems. By the end of the century, it is envisioned that the warming will exceed 3^{o}C, even though all Nationally Determined Contributions promised under Paris Agreement are fulfilled. The fluctuation in temperature will be at a higher rate in some regions when compared to others. Additional modifications in the climate system, including fluctuating precipitation and escalating extremes in temperature, will be considerably accelerated due to the greater temperature shifts. In 1951-2015, the tropical Indian Ocean experienced an average of 1 ^{o}C increment in sea surface temperature, which is significantly greater than the global mean SST rise of 0.7 ^{o}C (Krishnan *et al*., 2020). Tropical Cyclones and the accompanying storm surges are among the serious concerns confronting the coastal communities in the climate change scenario. Because of expanded SST, the severity of cyclones has increased tremendously in recent decades (Rao *et al*., 2020). According to Kumari *et al*., 2021, if the advancement is at the same rate, there will be an enhancement in the vapor pressure saturation, which might stimulate the water vapor and latent heat

that will further intensify the cyclones. Coastal regions are vulnerable to coastal flooding that arises because of storm surges. The urbanization of rural areas is primarily boosting the coastal population, especially in emerging nations such as India (Rao *et al*., 2020). In the climate change-induced global warming scenario, there is a shift in the global pattern of winds, expansion in Ocean Heat Content, etc., that involves a serious influence on the cyclogenesis, the track of cyclones, and its resulting biological production (Kuttippurath *et al*., 2021). At the time from 1951-2018, in the NIO basin, detected a significant reduction in the annual frequency of tropical cyclones whereas, from 2000-2018, the occurrence of very severe cyclonic storms has expanded dramatically during the post-monsoon season. As per the climate projections, all along the 21st century, there has been an enhancement in the intensity of tropical cyclones (Krishnan *et al*., 2020).

El Nino Southern Oscillation

In the Tropical Pacific Ocean, the sea surface temperature anomalies are mainly correlated to the phenomenon acknowledged, El Nino (Philander, 1983). ENSO is the most prevalent interannual phase of the coupled ocean-atmosphere system in the tropics. El Nino and La Nina, the extremes of ENSO, represent a diverse spectrum of climatic circumstances. In the interim of ENSO, the Walker circulation is disrupted by the cause of the atmospheric response to SST anomalies in the Equatorial Pacific, which seriously influences oceanic and atmospheric events worldwide. Amid El Nino years, research has revealed that in the BoB, Tropical Cyclone activity during severe cyclone months such as November and May exhibited a significant reduction (Girishkumar and Ravichandran, 2012). ENSO episodes endure approximately 12-18 months and transpire every 2-7 years with a wide intensity range. The cold phase of ENSO, acknowledged as La Nina is characterized by enhanced upwelling combined with shallow thermocline and surface divergence that is more powerful than normal.

Conversely, the El Nino, the warm phase of ENSO, is described by reduced upwelling associated with deep thermocline and feeble surface divergence. Throughout the Central and Eastern Pacific, the intensity of upwelling is generally depicted by Nino 3.4 Index, which is a critical governing factor in the ENSO phase. World Meteorological Organisation identifies the El Nino and La Nina years as those in which the Oceanic Nino Index (ONI) increased over 0.5^{o} C and dropped below -0.5^{o} C for at least 5 consecutive months (Mahala *et al*., 2015). ENSO is accountable for fluctuations in global climate by reason of coupling among sea level pressure, articulated as winds, wind stress and sea surface temperature anomalies affiliated to ENSO, including its spatial and timing teleconnections (Wahiduzzaman *et al.,* 2020).

Southern Oscillation Index (SOI) is a reliable predictor for characterizing variability in ENSO. SOI is the difference in sea level pressure across Tahiti and Darwin. Several prior pieces of research have employed SOI to investigate and model the ENSO impacts on Tropical Cyclone activity throughout Tropical Southwest Pacific, Northwest Pacific and Eastern Indian Ocean (Wahiduzzaman *et al.,* 2020). Walker Circulation and the moisture flow through the troposphere are altered by ENSO teleconnections, which influence the rainfall during protracted rains (Hoell *et al*., 2014).

Indian Ocean Dipole

A significant pattern of climate variability in the Indian Ocean on interannual durations is Indian Ocean Dipole (IOD), further termed as Indian Ocean Zonal Mode. The Tropical Eastern Indian Ocean is cooler than usual, while the Tropical Western Indian Ocean is warmer than normal, along with the positive phase of IOD. On the other hand, the negative IOD period is marked by water that seems warmer than normal in the Tropical Eastern Indian Ocean and cooler than usual over the Tropical Western Indian Ocean. Throughout the positive years of IOD, the typical convection over the Eastern Indian Ocean spreads to the west culminating in an

easterly wind anomaly in the Equatorial Indian Ocean (EIO), whereas the trend at the time of negative IOD years gets reversed (Girishkumar and Ravichandran, 2012). In the Tropical Eastern Indian Ocean, south-easterly trade winds in May-June direct the emergence of positive IOD events. After the development, the positive IOD anomalies are enhanced and sustained by the cause of ocean-atmosphere feedbacks. The reversal of trade winds in October-November occurs, allowing the events to peak and quickly dissipate. The Dipole Mode Index (DMI) is dependent on the SST anomaly difference amid the Equatorial Western Indian Ocean and Southern Indian Ocean and is often used to describe the IOD variability (Abram et al. 2020). In May-June, the emergence of IOD takes place, which reaches the zenith during October-November and subsides in December. The event is termed as positive IOD while the DMI is positive, and when the DMI is negative, the episode is termed negative IOD. In the BoB, just as La Nina occurrences, a negative IOD episode might induce extreme tropical cyclone conditions (Mahala *et al*., 2015mah).

Surface wind anomalies in the Central Equatorial Indian Ocean are significantly related to the SST anomalies at IOD occurrence. They considerably impact the sea level and thermocline anomalies, probably via oceanic adjustment processes (Saji and Yamagata, 2003). IOD episodes have implications on the tropical cyclones of the NIO in such a way that it alters the conditions for the genesis of tropical cyclones through modifications in steering flow which affects the trajectory of succeeding tropical cyclones (Yuan and Cao, 2013). IOD occurrences were unrelated to ENSO, and ENSO events were unrelated to IOD in a considerable number of cases. The occurrence of IOD events in the absence of ENSO resulted in a greater percentage of variance in Indian Ocean variability than those co-occurred with ENSO (Saji and Yamagata, 2003).

Madden-Julian Oscillation

Madden-Julian Oscillation (MJO) is a coupled ocean-atmosphere interaction, defined by perturbations of winds, clouds, pressure and rainfall that shifts eastward along the equator (Roxy *et al*., 2019). With a temporal duration of 30 to 60 days, it is marked by tropical convective anomalies and related circulation anomalies that propagate towards the east (Matthews, 2000). Over a particular region, the intensity and phase of MJO can boost or repress tropical rainfall variability, which can regulate or prompt extreme weather events. About 55% of instability in the meteorological variables is by virtue of MJO and regulates ENSO and tropical cyclogenesis and further influences the American, African, Australian and Asian monsoons. MJO occurrences commence over the Indian Ocean and proceed eastward over the maritime continent to the Pacific. Few of the storms diminish or dissipate over the continent or Central Pacific; however, the rest stretch further east and occasionally to the Atlantic (Roxy *et al*., 2019).

MJO can modify favourable large-scale circumstances for the genesis, strengthening and persistence of tropical cyclones. Lowered Vertical Wind Shear, midlevel moisture, improved low-level convergence, small eddies, cyclonic relative vorticity, deep convection, and synoptic disturbances act as embryos for tropical cyclones are the triggering factors for the MJO impacts on tropical cyclones (Zhang, 2013). Abnormal energetic surface winds enhance the evaporation combined with diminished solar insolation in the west of the convectively active zone reduces the sea surface temperature, whereas the SST to the east is enhanced due to excessive solar insolation and weakened surface winds. As per research, the MJO episodes frequently show up consecutively, implying that one MJO occurrence might contribute to another (Matthews, 2000). Over the Equatorial Indian Ocean, the influence of MJO on the SST is considerable. SST diminishes in the course of the active phase of MJO by loss of heat from the ocean by reason of net heat flux is negative whereas net heat flux is positive, and there appears enhancement in the SST in the interim of the suppressed phase of MJO (Raj Parampil *et al*., 2016)

MJO is influential in determining the interannual fluctuation in Tropical Cyclone Genesis (TCG). The Indian Ocean, the maritime continent and the

Western Pacific are hotspots for the MJO's active phase. Whenever the MJO's convectively active phase originates over the Indian Ocean and Maritime continent, the incidence of TCG has improved drastically (Tsuboi and Takemi, 2014).

Sea Surface Temperature

The climate can be described by the SST, which seems to be a prime determinant of energy balance that controls the circulation. The variables including net shortwave radiation, net longwave radiation, ocean currents, latent heat flux, sensible heat flux, eddy advection, wind stress curl, and mixed layer depth determine SST fluctuations. SST and the components of SST such as latent heat flux, sensible heat flux and radiative heat flux at the sea surface play a pivotal role in exchanging energy among the ocean and atmosphere. The NIO turns into the hottest among the world's oceans all along April-May. Intensification of surface winds and the enhancement of latent heat flux that culminate in the lowering of SST over the AS take effect in June, just as monsoon turns up, even though the temperature lowering is not homogenous across the AS. The Indian monsoon rainfall and the surface winds have quite a massive effect on the SST of the AS. Enhancement of evaporation, upwelling and expansion of coastal waters off the coasts of Arabia and Somalia, culminating in the expansion of cold water to the central part of the AS, is in behalf of the intensified winds. The slower cooling of SST in the BoB is attributed to significant rainfall, freshwater discharge, and the accompanying stratification in the interim of the South-West monsoon. The freshwater availability is higher in the BoB than that of the AS, at the hand of runoff from river and rainfall, which generates a less saline environment in BoB (Dinesh Kumar *et al.*, 2016).

Heavy winds combined with Tropical Cyclones have generated a drop in sea surface temperature below the storm for years. A small-scale SST decrease may extend to greater scales in the future. In the Northern hemisphere, the highest decline in the SST is observed to the right side of the track of Tropical Cyclones,

while the maximum SST drop in the Southern hemisphere is discovered to the left of the cyclone track. The amount of time required to regain the normal SST differs among Tropical Cyclones, extending from several days to weeks. Cyclone strength and the speed of translation are the main aspects of Tropical Cyclone that influence the lowering of SST, and the reduction in SST of greater magnitude are attributed to severe and slow-moving cyclones (Dare and McBride, 2011).

Heat Flux

A portion of heat accumulated in the ocean is discharged into the atmosphere, primarily through latent evaporation and longwave radiation (Yu *et al*., 2007). The combination of several heat transfer mechanisms at the ocean's surface comprising the warming attributed to Net Outgoing Longwave radiation, Short Wave Radiation, Latent Heat Flux and Sensible Heat Flux is the Net Heat Flux into the ocean. Except for Sensible Heat Flux, which relies on the temperature gradient, the Short-Wave Radiation contributes to the gain of heat by ocean, whereas the other mechanisms result in loss of heat (Rahul and Gnanaseelan, 2012). Shortwave radiation and Latent Heat fluxes are the two most prominent heat fluxes, whereas the Sensible Heat Flux and Longwave radiation make minor contributions (Tomita and Kubota, 2004). Even though the average of different flux products fluctuates with all of them demonstrating a decline in Net Heat Flux into the Indian Ocean and the drop is seen due to the enhancement in the turbulent heat flux out of the ocean, specifically the Latent Heat Flux (Rahul and Gnanaseelan, 2012).

Over the Tropical Oceans, Surface Latent Heat Flux (SLHF) acts as an essential mechanism in the coupled ocean-atmosphere interactions, accounting for the second most significant contributor of energy budget (Zhang and Mcphaden, 1995). As in the 1960s, all through the Indian Ocean, the SLHF stayed relatively steady (Jones *et al.*, 1995). Throughout most of the areas, there found negative values of SLHF, which implies that movement of heat is to the atmosphere from the ocean. Strong winds and considerable specific humidity variations generate

significant latent heat exchange (Tomita and Kubota, 2004). Strong winds and considerable temperature variations exacerbate SHF. As a result, a greater knowledge of SHF's temporal and spatial variability benefits in the identification of the heat exchange process, which is a fundamental mechanism in climate change (Cyriac et al., 2016). Contrary to LHF, the variations in SHF are relatively in a lower degree (Tomita and Kubota, 2004).

The global warming-induced temperature elevation over the NIO increases the heat from the atmosphere from the ocean, allowing the cyclones to strengthen quickly. The ocean mainly fuels tropical Cyclones by transferring latent heat and sensible heat flux within the ocean and atmosphere. Enhanced latent heat flux is significant for strengthening cyclones, where the higher latent heat flux moistens the boundary layer, permitting the development of cyclogenesis (Singh and Roxy, 2020).

Net primary productivity

The CO_2 outgassing to the atmosphere from the ocean is induced by the Tropical Cyclones, as it results in the movement of cold CO_2-rich water from the subsurface to the warm surface layer (Roy *et al*., 2020). The most important primary producer in the marine environment is the phytoplankton that produces organic materials by photosynthesis from nutrients, carbon dioxide in the presence of light energy along with the use of chlorophyll (Byju and Prasanna Kumar, 2011). Elevation in the SST indicates the increase in stratification, which eventually restricts the mixing and hinders the nutrient upwelling into the euphotic zone. This will further limit the productivity of the ocean and have detrimental effects on the fisheries. Climate change adversely affects the ocean's primary production worldwide by reducing the primary production of certain areas, diminishing the catch soon. ENSO has a significant impact on the SST, Net Primary Productivity, the concentration of Chlorophyll-a and fisheries, as it promotes fluctuations in the ocean and affects the marine ecosystems (Kumari *et al*., 2021). During Very Severe

Cyclonic Storms, a quick temperature drop can only be achieved by upward pumping of nutrient-rich cold water as a result of strong entrainment that allows enhanced biological production (Patra et al., 2007)

Because of the considerable discharge of freshwater in the BoB, which diminishes productivity and significant stratification, the BoB is generally considered a basin with low productivity compared to the AS. Heavy winds all along the Southwest monsoon season boost the productivity in the Western AS, whereas the productivity was comparatively lower over the Eastern AS (Singh and Roxy, 2020). Intense upwelling arises over the AS, while abrupt temperature fall happens because of entrainment induced by heavy winds. However, strong stratification develops as a result of heavy precipitation along with the runoff from the rivers. In addition, by cause of poor vertical mixing that occurs due to weak winds encourages the mixed layer depth that is shallow, which is the reason that the BoB appears to be less productive (Patra et al., 2007). Over the NIO, the AS is indeed one among the oxygen-depleted areas worldwide and a producer of Nitrous oxide; however, the BoB discharges less nitrogen oxide and Carbon Dioxide (Patra et al., 2007).

CHAPTER 3

MATERIALS AND METHODS

STUDY AREA

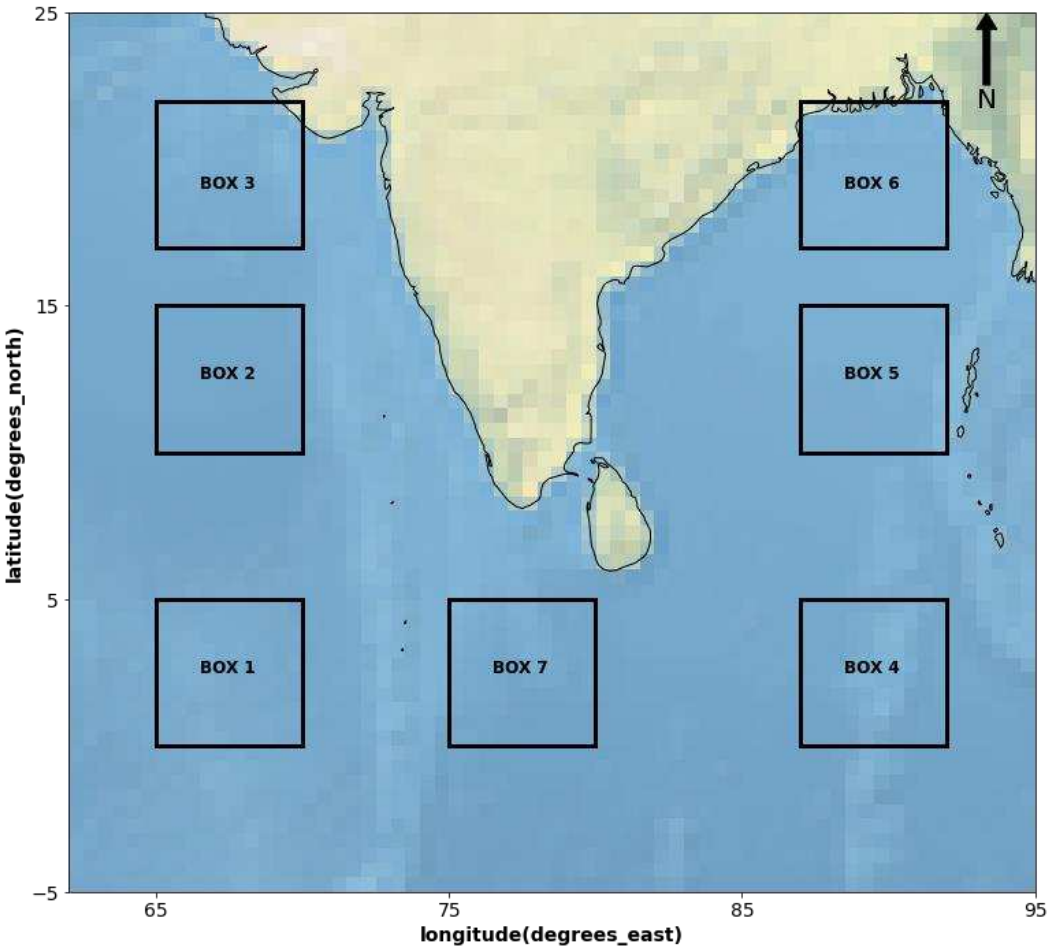

Figure 3.1 Study area: The Northern Indian Ocean comprising the Bay of Bengal and Arabian Sea. The analyses are carried out in the seven 5x5 latitude-longitude boxes. The Southern, Central and the Northern Arabian Sea was depicted using the Box 1,2 and 3 respectively. The Box 4,5 and 6 portray the Southern, Central and Northern Bay of Bengal respectively and the Box 7 illustrated the Central Indian Ocean Region.

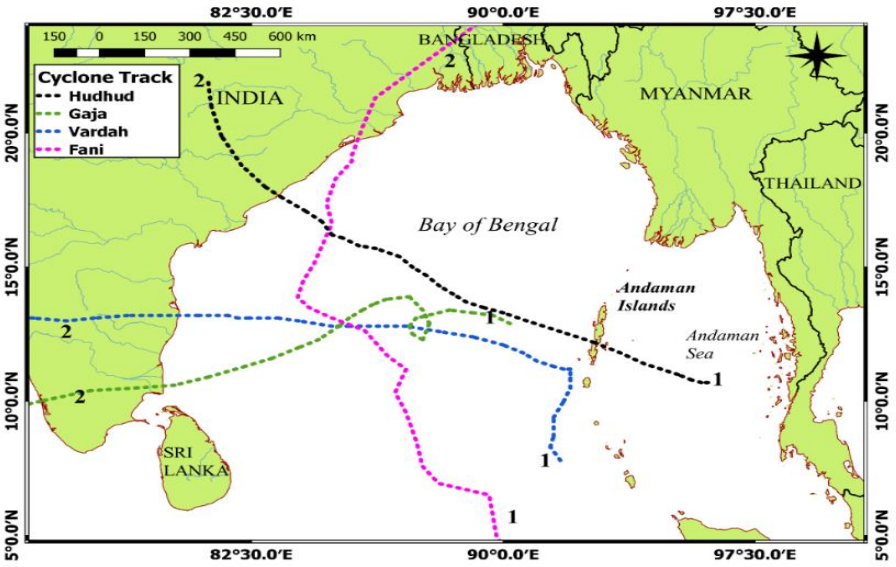

Figure 3.2 Study area of primary production with cyclone tracks (1 represents the formation area and 2 represent the dissipation region)

The Indian Ocean (IO) is a hotspot for climate research because the sea surface temperature is the key factor in shaping several climatic characteristics (Yoo *et al*., 2005). The Indian subcontinent landmass divides the NIO region into two basins, the Bay of Bengal (BoB) to the east and the Arabian Sea (AS) to the west (Sebastian and Behera,2015). The frequency of BoB tropical cyclones is more when compared to the AS by cause of high sea surface temperature and humidity that is sympathetic during both pre-monsoon and post-monsoon seasons. Global warming introduces further warming, which culminates in the intensification of BoB tropical cyclones. BoB cyclones turn into one of the deadliest tropical cyclones due to the shallow bottom and the triangular shape of the bay. There is a constant inflow of fresh warm water from perennial rivers, making it impossible to mix with cooler waters below.

The AS is one of the fastest-warming basins and most productive basins across the world. It has a monsoon climate. The AS is calm compared to BoB, which under strong winds that help dissipate heat and facilitate mixing with cold water beneath, thus reducing the temperature.

The area used for the study is the part of the NIO which comprises the AS and the BoB. The region of study is broken down into seven 5°x 5° latitude-longitude grids between 0-23°N and 65-92°E stated as,

i. 0-5°N, 65-70°E
ii. 10-15°N, 65-70°E
iii. 17-23°N, 65-70°E
iv. 0-5°N, 87-92°E
v. 10-15°N, 87-92°E
vi. 17-23°N, 87-92°E
vii. 0-5°N, 75-80°E

DATA

Sea Surface Temperature (SST)

Monthly Sea Surface Temperature (SST) from HadISST with a grid resolution of 1°x1° from 1900 to 2020 was obtained from Asia-Pacific Data-Research Centre (APDRC).

Oceanic Nino Index (ONI)

ONI was obtained from National Oceanic and Atmospheric Administration (NOAA) for the period 1900 to 2020 from the site https://psl.noaa.gov/gcos_wgsp/Timeseries/Data/nino34.long.anom.data

Precipitation

Daily averaged Total Precipitation data from ERA5, the fifth generation European Centre for Medium-Range Weather Forecast (ECMWF) for global climate and

weather. The data was recorded for 42 years with the unit metre from 1979-2020 with a regular latitude-longitude grid and horizontal resolution of 0.25° x 0.25°.

Surface Latent Heat Flux

Surface Latent Heat Flux is latent heat from the phase shifts like evaporation or condensation between the atmosphere and Earth's surface. The ERA5 dataset implemented by ECMWF with the unit Joules per square metre was obtained for 42 years from 1979-2020. The data have a regular latitude-longitude grid with a horizontal resolution of 0.25° x 0.25°.

Surface Sensible Heat Flux

Surface Sensible Heat Flux describes heat transmission from Earth's surface to atmosphere under turbulent air motion by removing the heat transfer from evaporation or condensation. The ERA5 data was gathered for a period of 42 years from 1979-2020. The unit is Joules per metre square, and the data has a regular latitude-longitude grid with 0.25° x 0.25° horizontal resolution.

Specific Humidity

Specific Humidity is the mass of water vapour per kilogram of moist air. ERA5 dataset was obtained for a period from 1979-2020 with a horizontal resolution of 0.25° x 0.25° with a regular latitude-longitude grid.

Wind

u and v components of wind are gathered from the ERA5 dataset. U component is the eastward component of wind, and the v component is the northward component.

The dataset with a unit metre per second was procured from 1979-2020 with a 0.25° x 0.25° horizontal resolution.

IOD

The IOD years was obtained from the study to analyse the impacts of IOD on global climate (Saji and Yamagata,2003) and the Bureau of Meteorology from the site

http://www.bom.gov.au/climate/enso/history/ln-2010-12/IOD-what.shtml

MJO

The MJO events were obtained from the study of Roxy *et al*.

https://github.com/RoxyKoll/warmpool-mjo/tree/master/MJO_events

FREQUENCY OF DEPRESSIONS, CYCLONIC STORMS AND SEVERE CYCLONIC STORMS

The data of the frequency of depressions, Cyclonic Storms and Severe Cyclonic Storms was procured from Cyclone- eAtlas – IMD, Tracks of Cyclones and Depressions over the NIO, 1891-2020 provided by the Regional Meteorological Centre, Chennai under Indian Meteorological Department, Ministry of Earth Sciences, Government of India.

TROPICAL CYCLONE DATA

The Tropical Cyclone data, including the track points with Latitude and Longitude, Cyclone Intensity, Pressure, Wind and Cyclone Stages, are obtained from Joint Typhoon Warning Center (JTWC) (Chu et al. 2002). We were only considering the very severe cyclonic (VSC) and extremely severe cyclonic (ESC) events for this study. They are Hudhud (ESC) in Oct 2014, Vardah (VSC) in Dec 2016, Gaja

(VSC) in Nov 2018 and Fani (ESC) in April 2019. The first three cyclones were formed and developed over the Andaman region and travelled more than five days before the landfall over the Indian subcontinent. Cyclone Fani was formed over the southern BoB region, and it also travelled more than 5 days before it reached the Indian coast.

REMOTE SENSING DATA AND MODEL DATA

The 8-day average of wind field data (wind speed) was calculated from the daily data extracted from the ERA 5 datasets obtained from the Copernicus climate data store (https://cds.climate.copernicus.eu/), with a spatial resolution of 0.25◦ × 0.25◦. The 8-day average sea surface Chlorophyll-a concentration (Chl-a) was merged using the MODIS Aqua and MODIS Terra L3 products (http://oceancolor.gsfc.nasa.gov/) with a spatial resolution of 4 × 4 km. From the World Ocean Atlas 2018 (WOA18), climatological nitrate profiles were taken.

MATERIALS AND METHODS

Sea Surface Temperature

A large SST of greater than 27°C is required for the development of Tropical cyclones. The SST over the Indian Ocean for 120 years was analysed. Monthly SST and yearly average SST were figured out from 1900 to 2020, and the trend was scrutinised. Further, the trend analysis was carried out by calculating the standard deviation of the yearly average SST. The SST variation in this region was evaluated by establishing the mean sea surface temperature of 1900 as a base value, and the fluctuation of SST was recorded and presented.

The Surface Latent Heat flux, Surface Sensible Heat Flux, Specific Humidity, Wind and Total Precipitation datasets were used, and their variations over the study

area from 1980-2020 were evaluated. The daily average, yearly average, and standard deviation of these datasets were calculated and presented. The variation of these variables from the base value, the value in 1900, was also analysed and displayed.

Oceanic Nino Index

The El Nino and La Nina years were identified using the ONI. The years with values equal to or above +0.5° anomaly for 5 successive seasons is described as El Nino years, and the years with values equal to or below -0.5° anomaly is described as La Nina years. It is further considered as weak, moderate and strong El Nino and La Nina events when the SST anomaly is between 0.5-0.9, 1-1.4 and greater than 1.5, respectively.

SST anomaly for the El Nino and La Nina years were calculated as,

Anomaly = Actual value of average temperature – Long term average temperature

The ONI from 1900 to 2020 was determined and marked to estimate the SST anomaly in the Pacific during El Nino and La Nina years. To ascertain its effect on the Indian Ocean, the SST anomaly for the seven areas mentioned above was estimated. The trend in Indian Ocean Sea Surface Temperature Anomaly amid El Nino and La Nina years was evaluated.

Primary Productivity

To assess the impact on primary productivity, the Vertically Generalized Production Model from Behrenfeld and Falkowski [1997] was used to estimate the increase in primary production due to cyclone-induced phytoplankton bloom

events. For the VGPM, net primary production is a function of chlorophyll, available light, and the photosynthetic efficiency

The Ekman pumping velocity (EPV) is calculated from the 8-days average ERA-5 datasets (positive indicates upwards):

$$\mathbf{EPV} = \boldsymbol{Curlz}\left(\frac{\tau}{fx\rho w}\right) \ldots\ldots\ldots\ldots\ldots\ldots\ldots\ldots \mathbf{(1)}$$ (Xu *et al.,* 2019)

where f is the Coriolis parameter, ρw is the density of sea water (refers to 1025.0 kg/m3).

The depth of the euphotic zone (Ze) is defined as the depth at which the photon flux equals 1% of the flux measured just above the air–sea interface

$$\mathbf{Ze} = \mathbf{35} \times \mathbf{C_{Chl}^{-0.35}} \ldots\ldots\ldots\ldots\ldots\ldots\ldots \mathbf{(2)}$$ (Liu *et al*., 2020)

THE METHODOLOGY OF THE STATISTICAL APPROACH

Hydrodynamics, hydrographic and atmospheric parameters in a given period at a location is variable from one year to another. The variability depends on many parameters and the length of the considered period. Probability distributions are widely used in understanding the variation of dynamics patterns and the computation of probabilities. Under stable hydrologic conditions, traditional probabilistic techniques to defining risk, reliability, and return periods presume that extreme events arise from serially independent time series with a probability distribution with fixed moments and parameters. Risk, reliability, and return periods are often employed in the analysis of extreme events in hydrology. Various other environmental hazards include temperatures, wind speeds, sea levels, cyclones, wave height, earthquakes, tsunamis, etc. This is well used for the fields of water resource systems planning and management as well as for flood and drought risk assessment and mitigation. The proper database is needed to assess the variability of a parameter in a region, the absence of which can lead to erroneous

planning and design. Long-period data can provide reliable management of a proposed project. The major statistical equations and interpretations are explained below

PROBABILITY

The probability formula is used to compute the probability of an event to occur.

P(A) is the probability of an event "A",

$$P(A) = \frac{\text{Number of favourable outcomes}}{\text{Total number of favourable outcomes}} \text{ ---------- (3)}$$

The present study computed the statistical probabilities using Weibull's plotting position formula and applied to the favourable parameters. In this method, we arranged the parameters in descending order and assigned 1st rank to the highest value and subsequent rank to lower values to compute another statistical parameter explained below.

RETURN PERIOD

A return period of an event is the interval between two extreme events, where an event is anything exceeding a known threshold value. A return period, also known as a recurrence interval or repeat interval, is an average time or an estimated average time between events such as earthquakes, floods, landslides, or river discharge flows to occur. It is a statistical measurement typically based on historical data over an extended period and is used usually for risk analysis. Examples include deciding whether a project should be allowed to go forward in a zone of a certain risk or designing structures to withstand events with a certain return period.

The probability of exceedance of an event return period (T),

$$T = \frac{\mathrm{N+1}}{\mathrm{m}}$$ ---------- (4)

Where m is the order or rank and N is the total number of events.

BINOMIAL THEORY

Consider the case of planning for a random future annual maximum extreme event X, where the design quantile Xp is the threshold of exceedance and determines whether an event with exceedance probability P, occurs in a given year. According to the binomial theorem, in a given period of n years, the probability of a given number of r events of a return period T is given by the binomial distribution as

$$nC_r\, P^r Q^{(n-r)}$$ ---------- (5)

Where P is the probability of occurring an event and Q is the probability of not occurring an event.

RISK

Risk is the probability of harmful consequences or expected losses (deaths, injuries, property, livelihood, economic activity disrupt or environment damaged) resulting from the interaction between natural or human-induced hazards and vulnerable conditions. Risk of failure over a planning period here as in most introductory hydrology textbooks [Bras, 1990; Viessman and Lewis, 2003; Mays, 2001] and hydrology handbooks [Stedinger et al.,1993; Interagency Committee on Water Data (IAWCD), 1982; Chow, 1964], as the likelihood of experiencing at least one event exceeding the design event over a given proposed project life of n years:

$$Risk = 1 - (1 - P)^n$$ ---------- (6)

RELIABILITY

Risk is a combination of probability and the consequences of adverse events. The main parameter for the relationship between reliability and risk can be considered a duration of an event. The longer the duration, the higher the reliability and the less the risk and vice versa. If we think about risk, we should consider how reliable a proposed project plan. Reliability over a planning period is defined as the probability that a system will remain in a satisfactory state [Hashimoto et al., 1982; Salas and Obeysekera, 2014] during its lifetime, i.e., that an exceedance event will not occur within a project life of n years.

$$Reliability = (1 - P)^n \quad \text{---------- (7)}$$

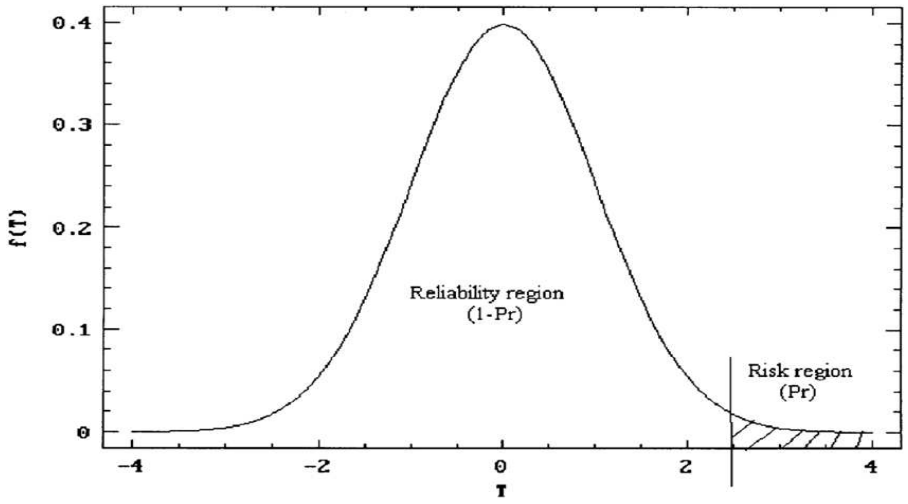

Figure 3.3 Graphical representation of probability distribution with reliability and risk

CHAPTER 4

RESULTS

4.1 SEA SURFACE TEMPERATURE

a)

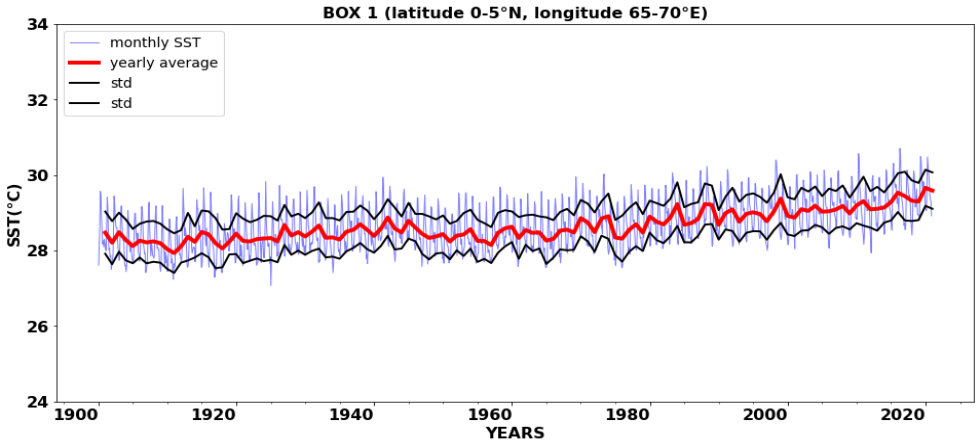

b)

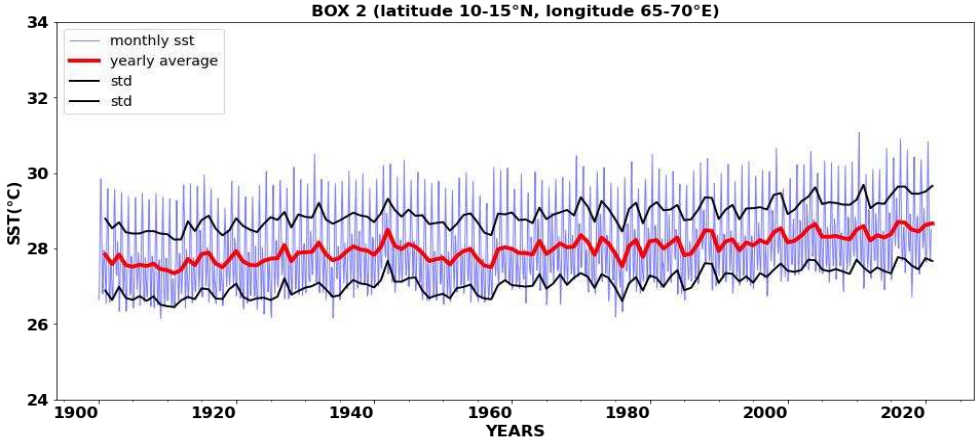

c)

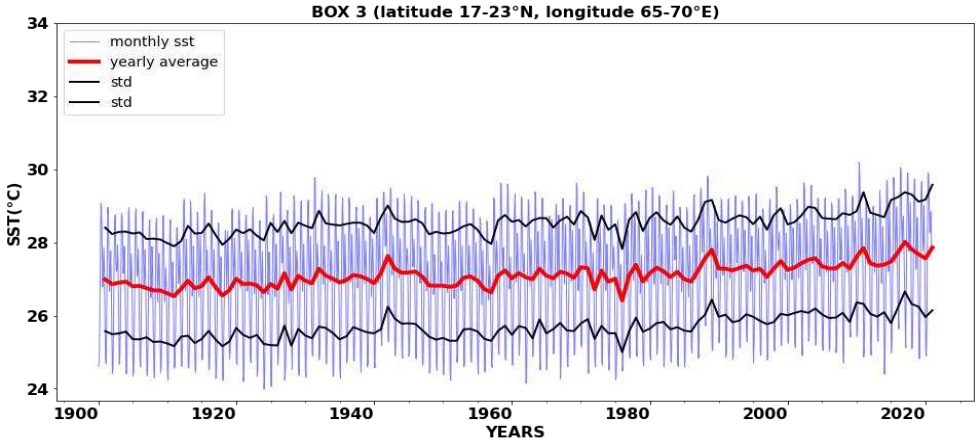
BOX 3 (latitude 17-23°N, longitude 65-70°E)
monthly sst
yearly average
std
std
SST(°C)
YEARS
34
32
30
28
26
24
1900
1920
1940
1960
1980
2000
2020

d)

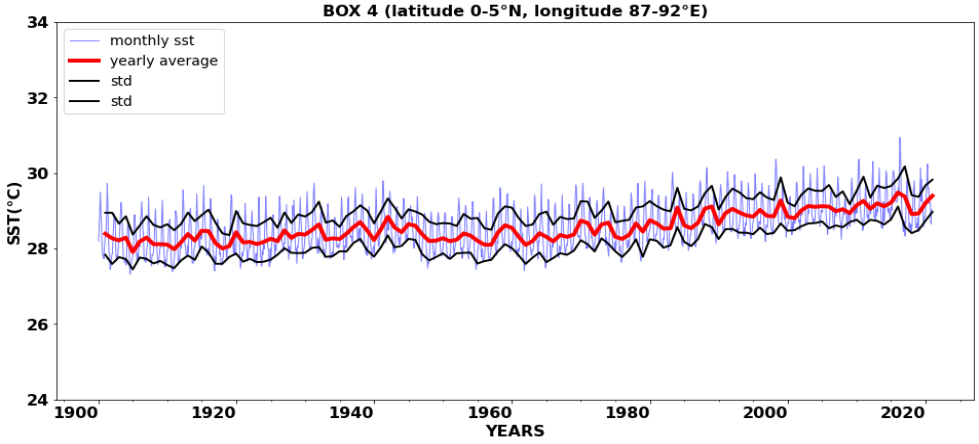
BOX 4 (latitude 0-5°N, longitude 87-92°E)
monthly sst
yearly average
std
std
SST(°C)
YEARS
34
32
30
28
26
24
1900
1920
1940
1960
1980
2000
2020

e)

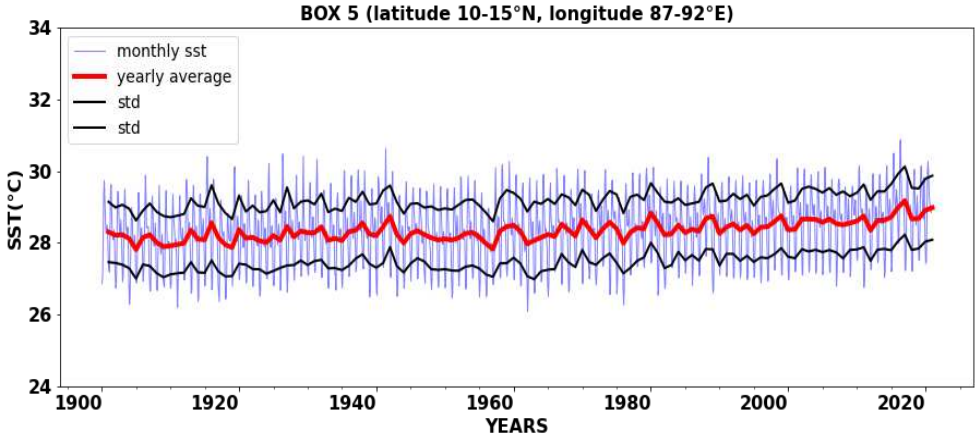
BOX 5 (latitude 10-15°N, longitude 87-92°E)
monthly sst
yearly average
std
std
SST(°C)
YEARS
34
32
30
28
26
24
1900
1920
1940
1960
1980
2000
2020

f)

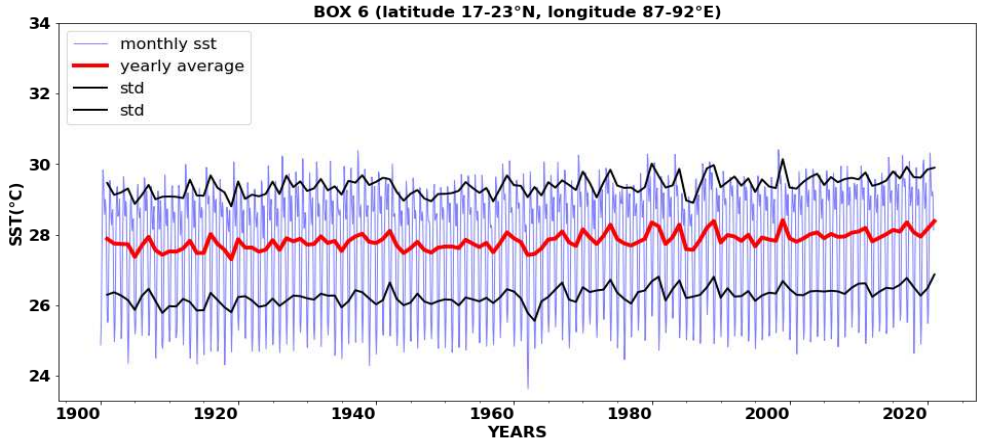

g)

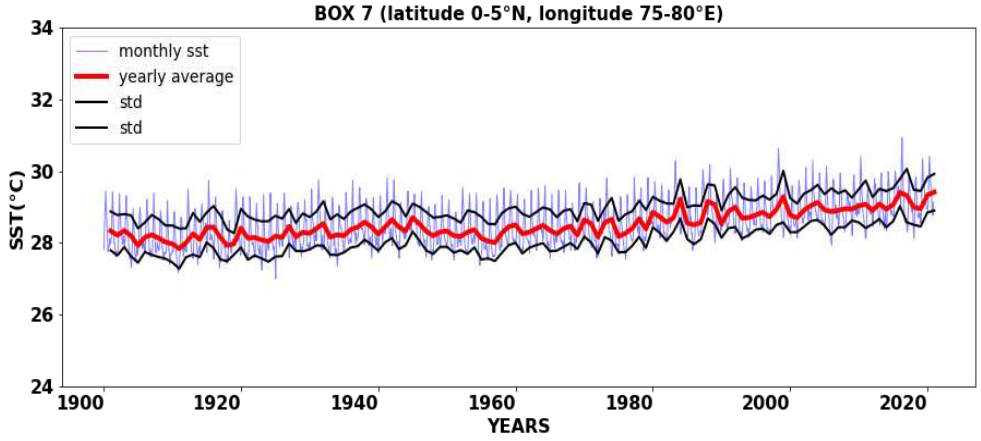

Figure 4.1(a-g) Variation in Sea Surface Temperature from 1900-2020 over the NIO

SST of greater than 27 ºC is one of the decisive aspects for the formation of tropical cyclones. Figure 4.1 (a-g) illustrates the variation in SST in the seven 5x5 latitude-longitude boxes over the Indian Ocean. In Box 1, the SST exhibited a positive trend, where the increase was a bit more pronounced after the 1970s. Over Box 2, a slight increase in SST was recorded and there was a steady increase in the temperature in this region. In Box 3, an increasing trend in SST was observed, with warming more evident after 1990. The SST exhibited an increasing trend over Box 4 where the temperature increased tremendously after the 1980s. Over Box 5, the SST displayed a slight rapid increase after 2010. In Box 6, the SST advertised an increasing trend with not much variation over the

years. Over Box 7, the pattern of SST was increasing with a marked increase after 1980.

The SST over Box1, 4 and 7 which was located over the same latitudinal range (0-5^{o}N) exhibited a similar pattern of increase with a temperature range of 27 and 31 ^{o}C. Likewise, the SST progression was very much alike over Box 2 and Box 5, over the latitude 10-15 ^{o}N, where the SST was between 26 and 31 ^{o}C. The SST was between 24 and 31 ^{o}C over Box 3 and Box 6 in the latitude range of 17-23 ^{o}N. Figure 4.1 presented that the SST over all the seven boxes were not uniform and the pattern of SST over the years fluctuated asymmetrically. The Standard Deviation, that is the measure of variation from the mean was identified to vary differently in all seven boxes. The deviation was greater over Box 6 and then Box 3, whereas it was found to be minimum over Box 1, Box 4 and Box7. The SST variation from the mean was observed to be very high in the Northern BoB and AS, whereas the Southern BoB, AS and the Central Indian Ocean region exhibited only a small deviation from the normal.

4.1 A. VARIATION IN SEA SURFACE TEMPERATURE RELATIVE TO 1900

a)

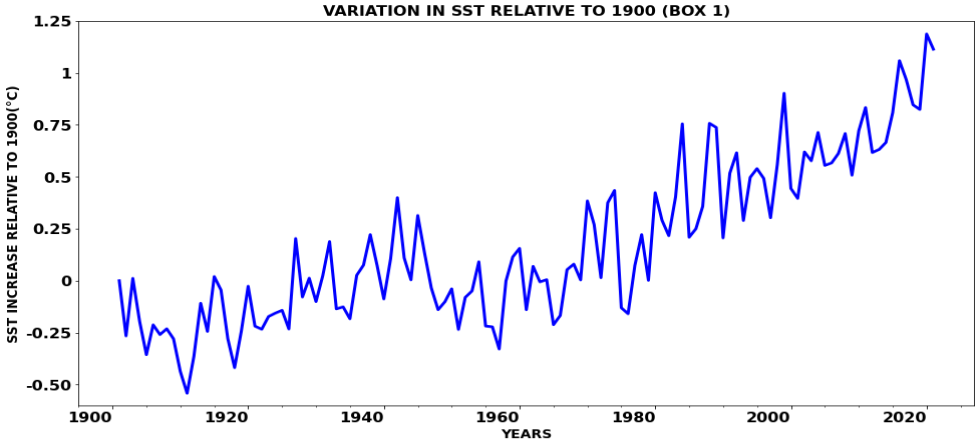

b)

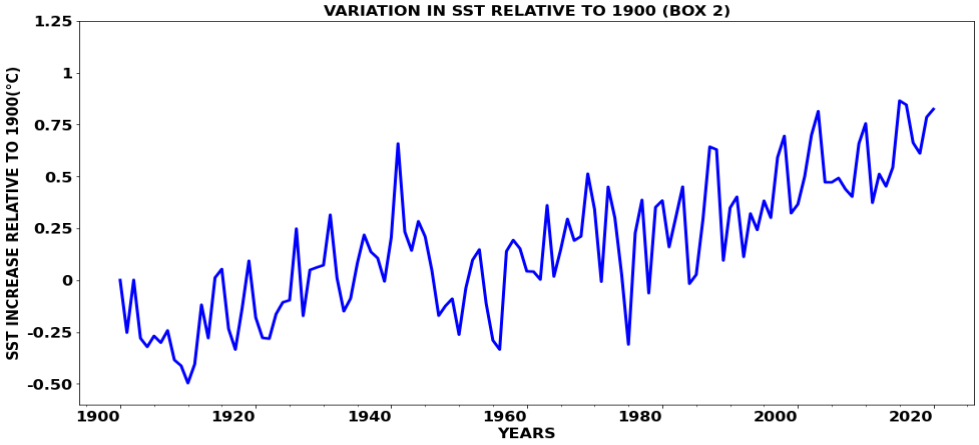
VARIATION IN SST RELATIVE TO 1900 (BOX 2)
SST INCREASE RELATIVE TO 1900(°C)
1.25
1
0.75
0.5
0.25
0
-0.25
-0.50
1900
1920
1940
1960
1980
2000
2020
YEARS

c)

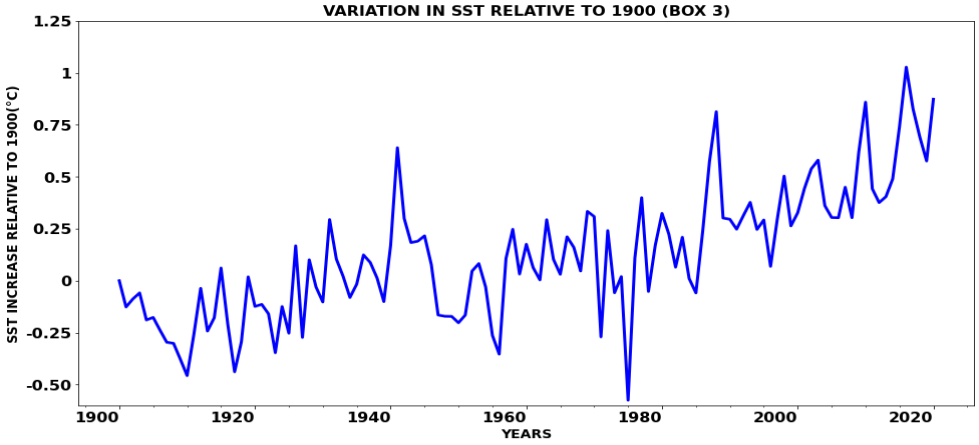
VARIATION IN SST RELATIVE TO 1900 (BOX 3)
SST INCREASE RELATIVE TO 1900(°C)
1.25
1
0.75
0.5
0.25
0
-0.25
-0.50
1900
1920
1940
1960
1980
2000
2020
YEARS

d)

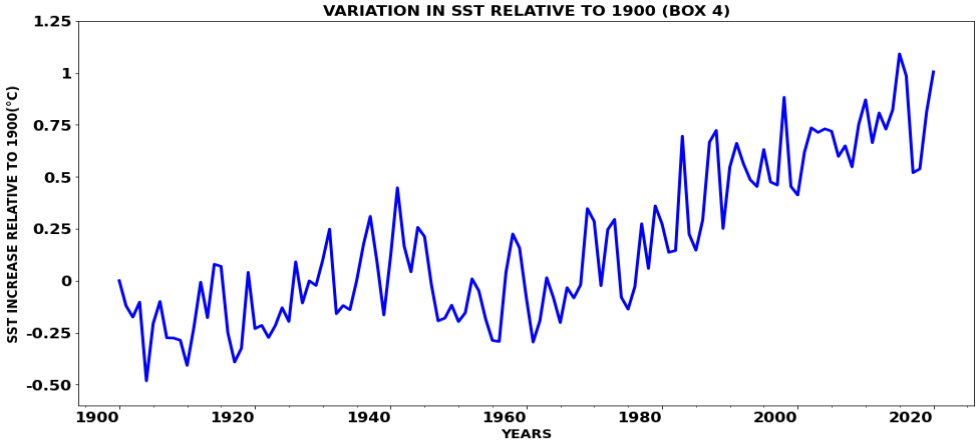
VARIATION IN SST RELATIVE TO 1900 (BOX 4)
SST INCREASE RELATIVE TO 1900(°C)
1.25
1
0.75
0.5
0.25
0
-0.25
-0.50
1900
1920
1940
1960
1980
2000
2020
YEARS

e)

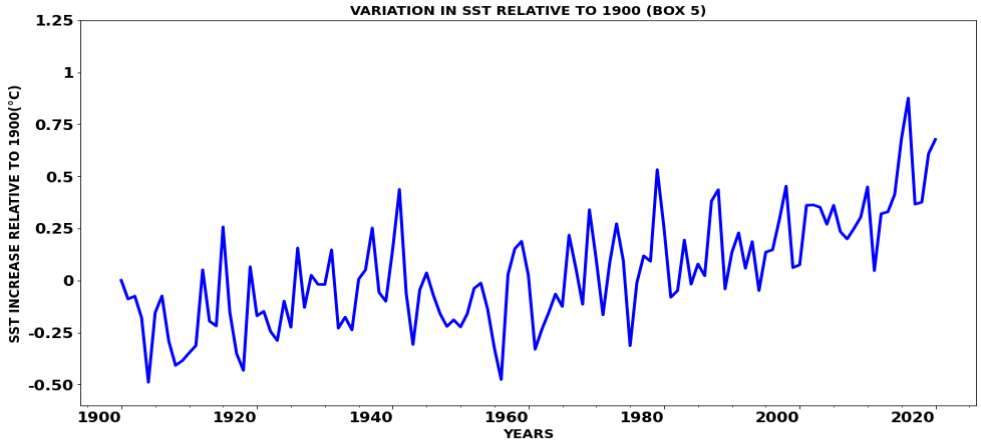

f)

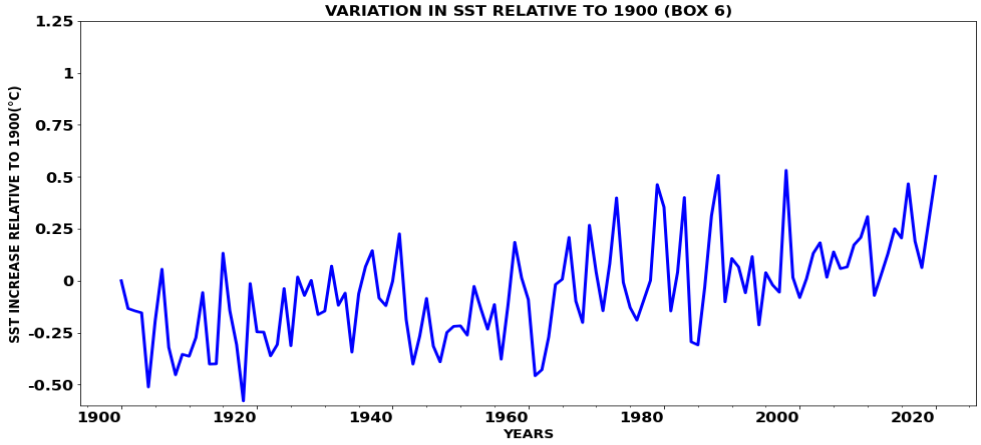

g)

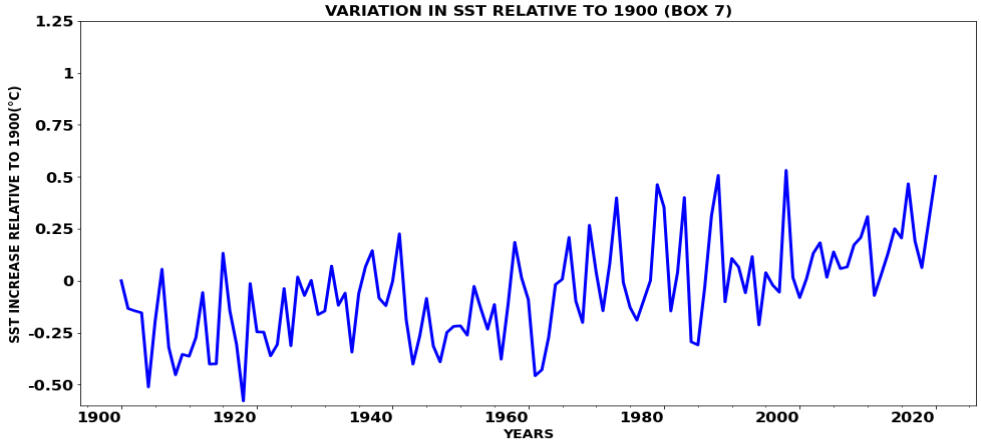

Figure 4.1 A (a-g) Variation in Sea Surface Temperature relative to the Sea Surface Temperature of 1900 over the NIO

Figure 4.1 A represents the deviation in SST from the SST of 1900. The temperature difference from 1900-2020 was investigated. The variation in SST in all the boxes depicted a clear increase over the years. In Box 1, there was an increase of about 1.25 ^{o}C by the end of 2020. From 1900 to 1940, the increase was not so rapid whereas, after 1980, the temperature was observed to advance expeditiously. From 1940-1960, not much increase was examined. Over Box 2, the increase in the temperature relative to the SST of 1900 was examined to increase and by 1940 the temperature rise was about 0.75 ^{o}C. From 1940-1960, there was a decrement in the temperature. The temperature had a maximum decline of about 0.5^{o}C in 1915. The SST was again discovered to advance from 1960 and there a was greater than 0.75^{o}C rise in SST by 2020. The SST variation in Box 3 was detected to have an overall increasing trend. The temperature rise was observed to boost till 1940, where the temperature elevation was above 0.5^{o}C and further there was an enhancement in the SST after 1980 where the increase in temperature was about 1^{o}C by the end of 2020 and the greatest decrease of greater than 0.5^{o}C was identified in 1975. In Box 4, the pattern of increase of SST displayed an increasing trend with a more pronounced increase after 1980 where the rise in temperature by 2020 was greater than 1^{o}C above the levels of 1900. The SST in the interim of 1940-1960 had a decline whereas there was an increment of up to 0.5^{o}C from 1900-1940. The temperature rise had an overall advancing pattern over Box 5. By the end of 2020, the rise in the SST compared to that of the SST in 1900, was greater than 0.75^{o}C. The increase was more evident after 2000. The maximum decrement in the SST from 1900 was observed with a decrease of about 0.5^{o}C from the 1900 levels. Over Box 6, the elevation in temperature was about 0.5^{o}C by 2020 which was less than the reduction from the SST from 1900, where the decline in the SST was higher than 0.5^{o}C. There was an overall increase in the SST in Box 7 and the increase was not pronounced from 1940-1960. The decrement in the SST was greater than 0.5^{o}C whereas the SST increment was only up to 0.5^{o}C by 2020.

4.2 SURFACE LATENT HEAT FLUX

a)

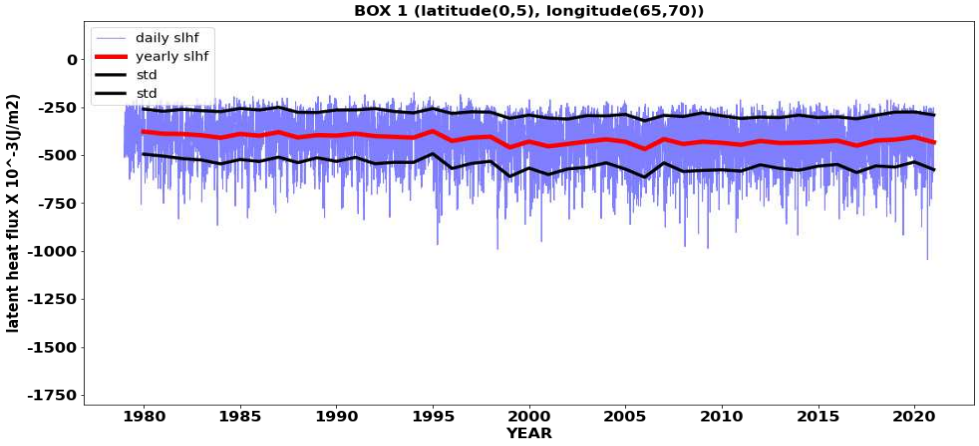
BOX 1 (latitude(0,5), longitude(65,70))
daily slhf
yearly slhf
std
std
latent heat flux X 10^-3(J/m2)
0
-250
-500
-750
-1000
-1250
-1500
-1750
1980
1985
1990
1995
2000
2005
2010
2015
2020
YEAR

b)

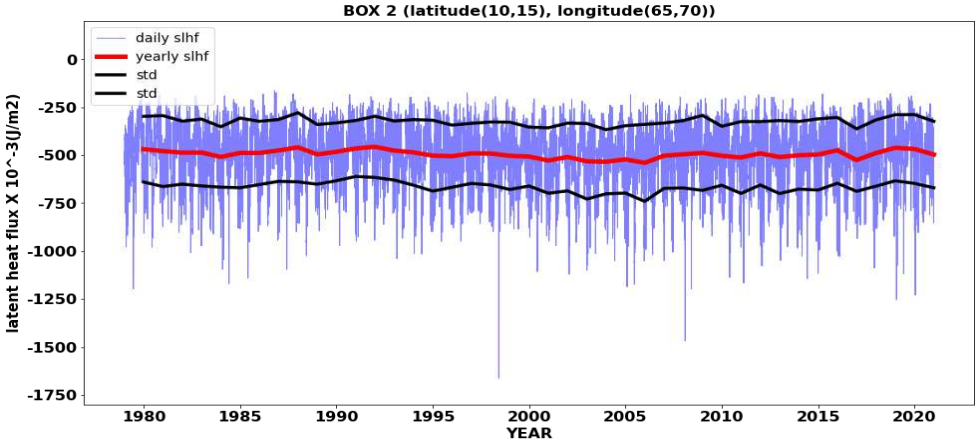
BOX 2 (latitude(10,15), longitude(65,70))
daily slhf
yearly slhf
std
std
latent heat flux X 10^-3(J/m2)
0
-250
-500
-750
-1000
-1250
-1500
-1750
1980
1985
1990
1995
2000
2005
2010
2015
2020
YEAR

c)

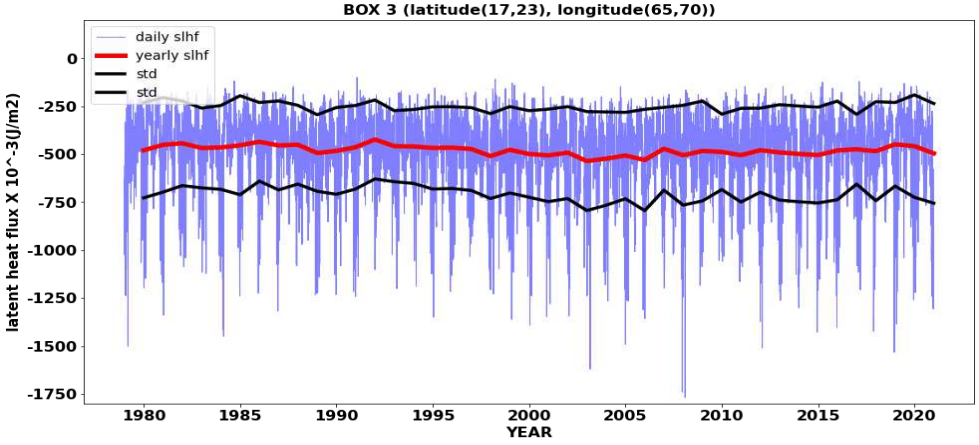
BOX 3 (latitude(17,23), longitude(65,70))
daily slhf
yearly slhf
std
std
latent heat flux X 10^-3(J/m2)
0
-250
-500
-750
-1000
-1250
-1500
-1750
1980
1985
1990
1995
2000
2005
2010
2015
2020
YEAR

d)

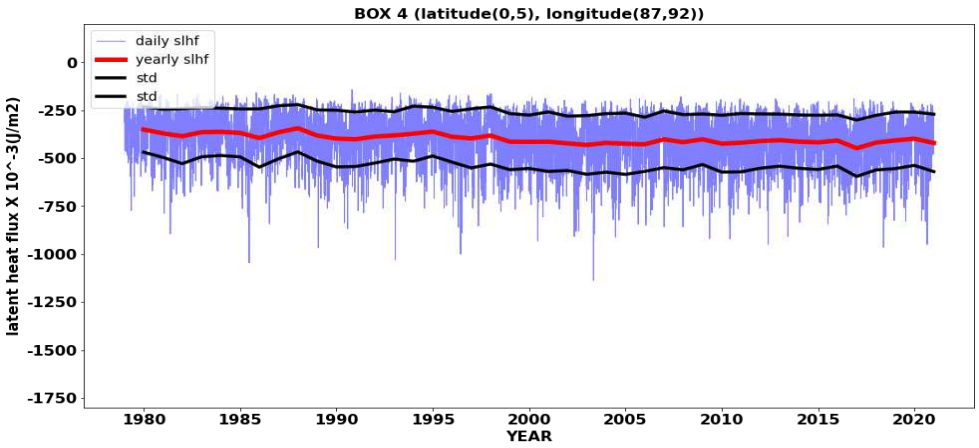
BOX 4 (latitude(0,5), longitude(87,92))
daily slhf
yearly slhf
std
std
latent heat flux X 10^-3(J/m2)
0
-250
-500
-750
-1000
-1250
-1500
-1750
1980
1985
1990
1995
2000
2005
2010
2015
2020
YEAR

e)

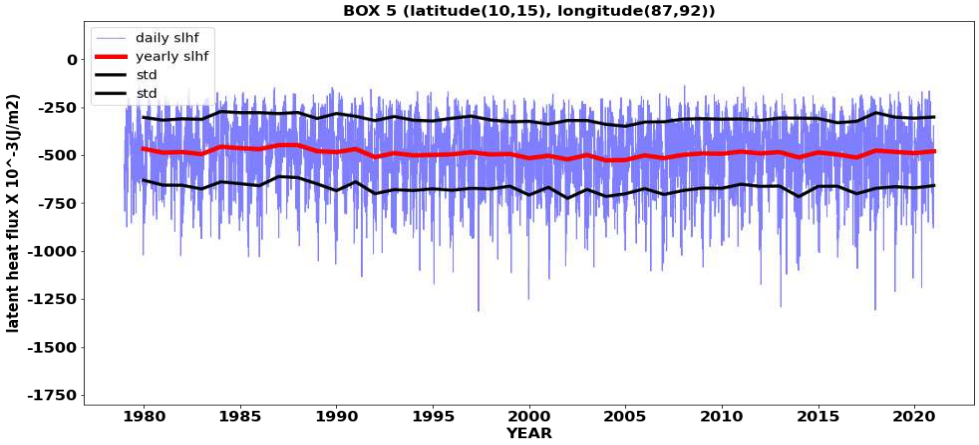
BOX 5 (latitude(10,15), longitude(87,92))
daily slhf
yearly slhf
std
std
latent heat flux X 10^-3(J/m2)
0
-250
-500
-750
-1000
-1250
-1500
-1750
1980
1985
1990
1995
2000
2005
2010
2015
2020
YEAR

f)

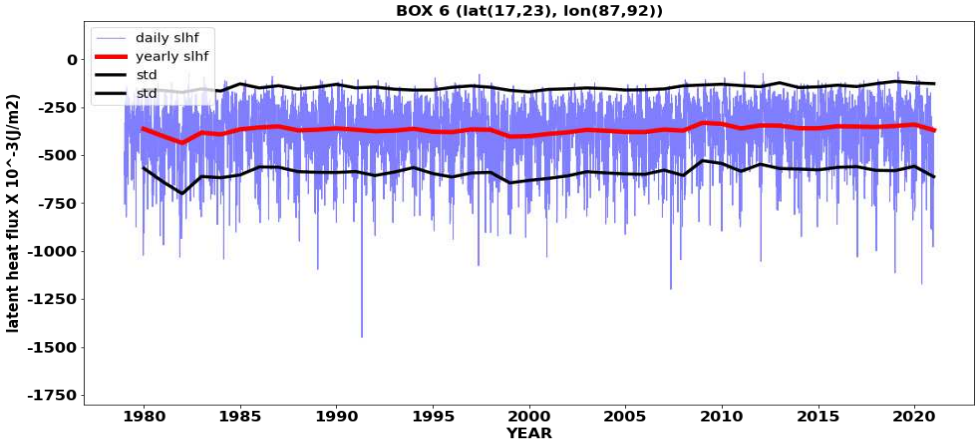
BOX 6 (lat(17,23), lon(87,92))
daily slhf
yearly slhf
std
std
latent heat flux X 10^-3(J/m2)
0
-250
-500
-750
-1000
-1250
-1500
-1750
1980
1985
1990
1995
2000
2005
2010
2015
2020
YEAR

g)

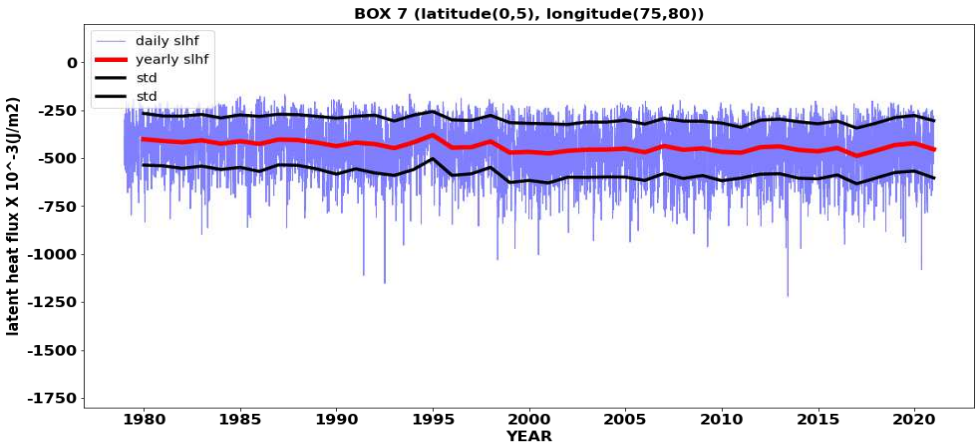

Figure 4.2 (a-g) Variation in Surface Latent Heat Flux from 1979-2020 over the NIO

The energy lost or gained by the water through evaporation or condensation as water flows from a higher energy state to lower or vice versa is referred to as latent heat flux. Figure 4.2 (a-g) illustrates the surface latent heat flux over 7 boxes. The Box1 has a latent heat flux that ranges between -1000×10^{-3} and -150×10^{-3} J/m^2. There is no consistent increasing pattern in the surface latent heat flux of this region. Over Box 2, an increase in the latent heat flux with the year was not found. The value of surface latent heat flux in this domain ranges from -1250×10^{-3} J/m^2 and -200×10^{-3} J/m^2 where this value in certain years reached up to -1750×10^{-3} J/m^2. Box 3, has the latent heat flux values generally fluctuating between -1300×10^{-3} J/m^2 and -100×10^{-3} J/m^2 with no clear evidence of steep increase over this region. The values of latent heat flux amid certain years extended up to -1800×10^{-3} J/m^2. The surface latent heat flux was displayed in Box 4 where the latent heat flux value in this region exhibited a variation between -1150×10^{-3} J/m^2 and -150×10^{-3} J/m^2. Box 5 have the latent heat flux values between -1300×10^{-3} J/m^2 and -150×10^{-3} J/m^2. The surface latent heat flux over Box 6 was fluctuating and the values extended between -1200×10^{-3} J/m^2 and -100×10^{-3} J/m^2 and in certain years it reached up to -1500×10^{-3} J/m^2. Over Box 7, the value of surface latent heat flux fluctuated between -1250×10^{-3} J/m^2 and -150×10^{-3} J/m^2. The pattern of Surface Latent Heat Flux over all the seven boxes were not uniform. The standard deviation in all the

boxes was different from one another where the standard deviation was maximum in Box 3 and Box 6. The variation of SLHF was found to be maximum over the Northern and Central BoB and AS.

4.3 SURFACE SENSIBLE HEAT FLUX

a)

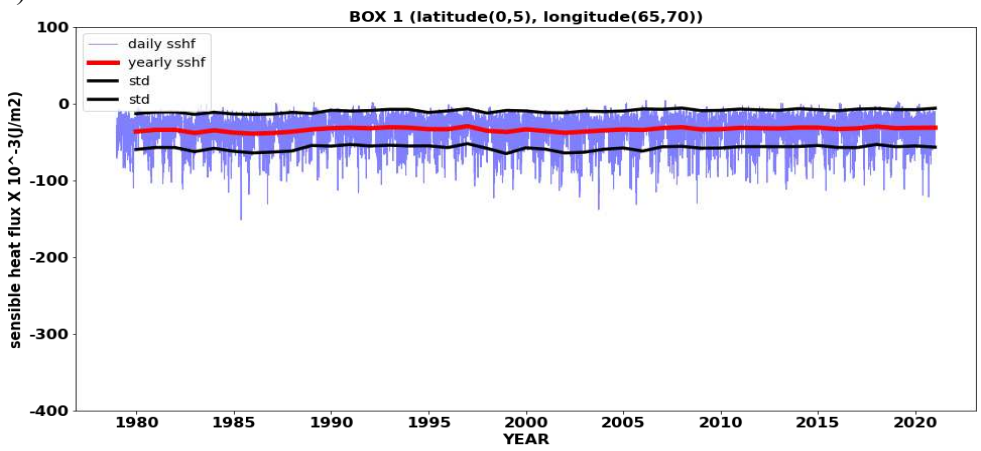

b)

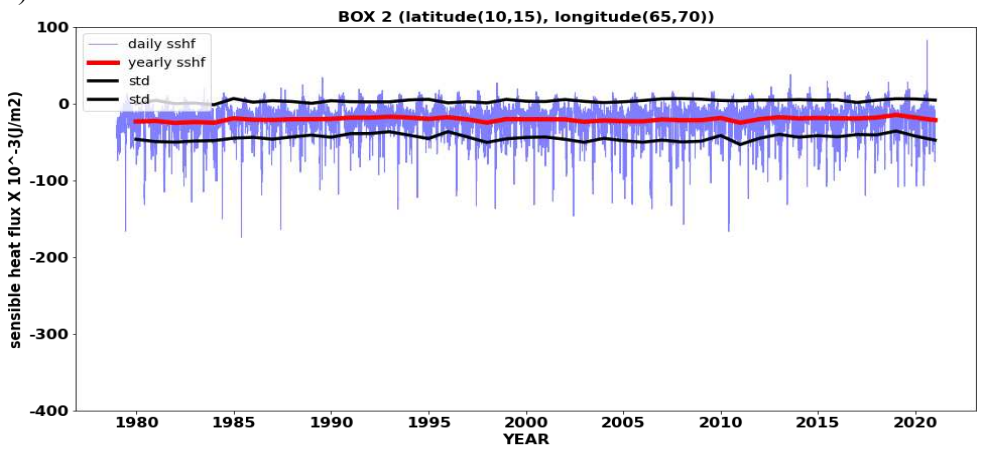

c)

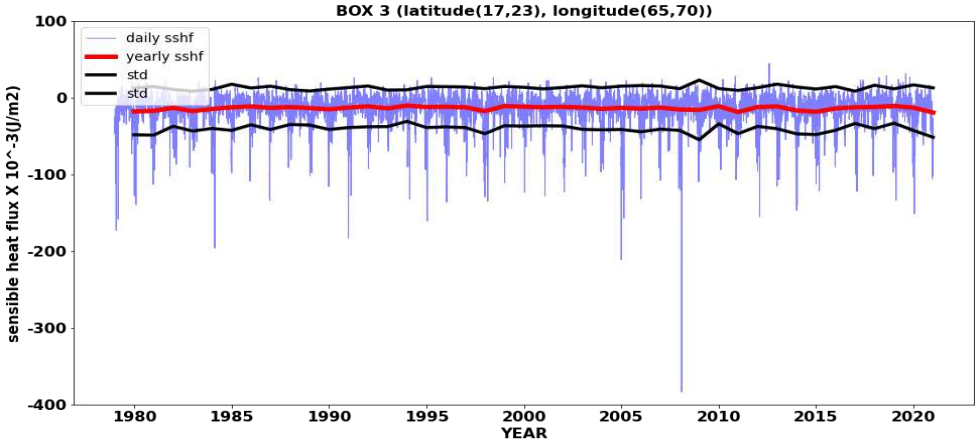
BOX 3 (latitude(17,23), longitude(65,70))
daily sshf
yearly sshf
std
std
sensible heat flux X 10^-3(J/m2)
YEAR

d)

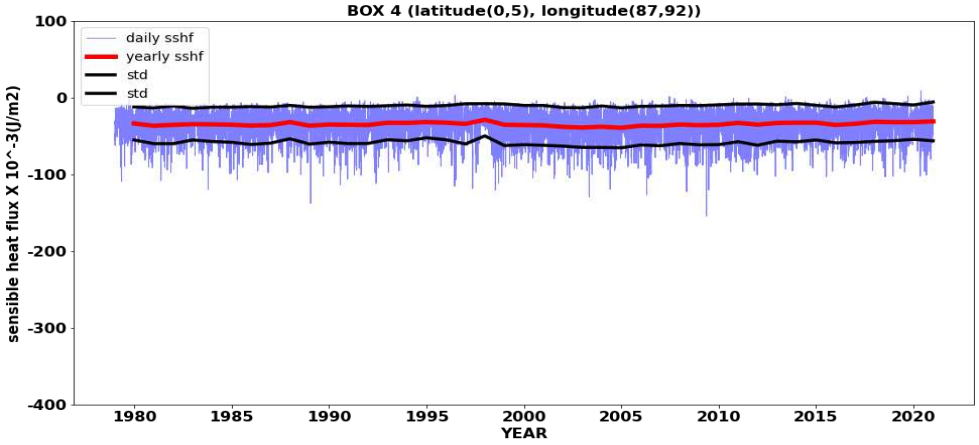
BOX 4 (latitude(0,5), longitude(87,92))
daily sshf
yearly sshf
std
std
sensible heat flux X 10^-3(J/m2)
YEAR

e)

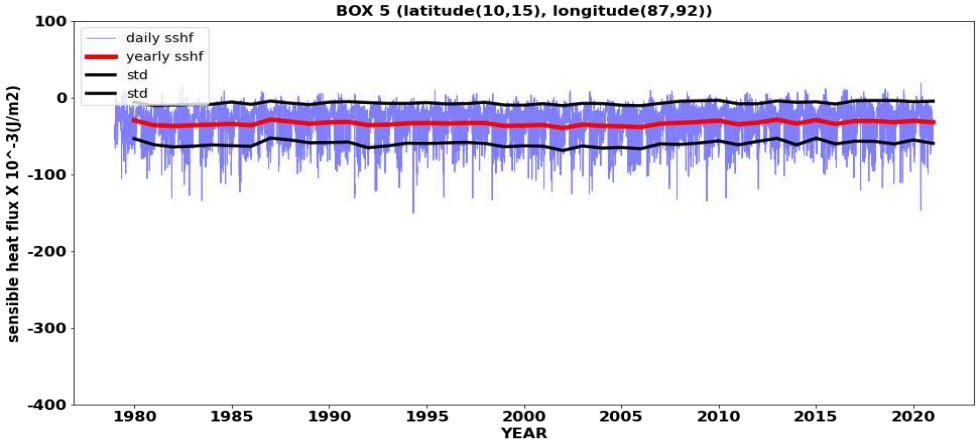
BOX 5 (latitude(10,15), longitude(87,92))
daily sshf
yearly sshf
std
std
sensible heat flux X 10^-3(J/m2)
YEAR

f)

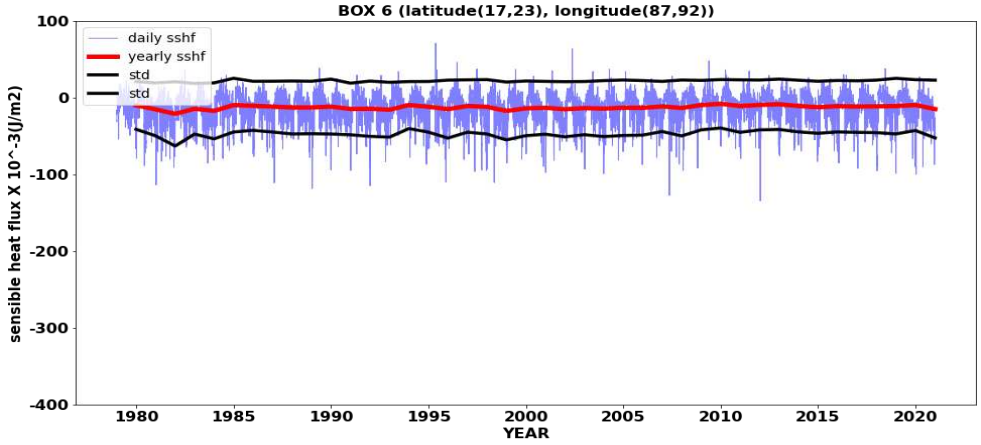

g)

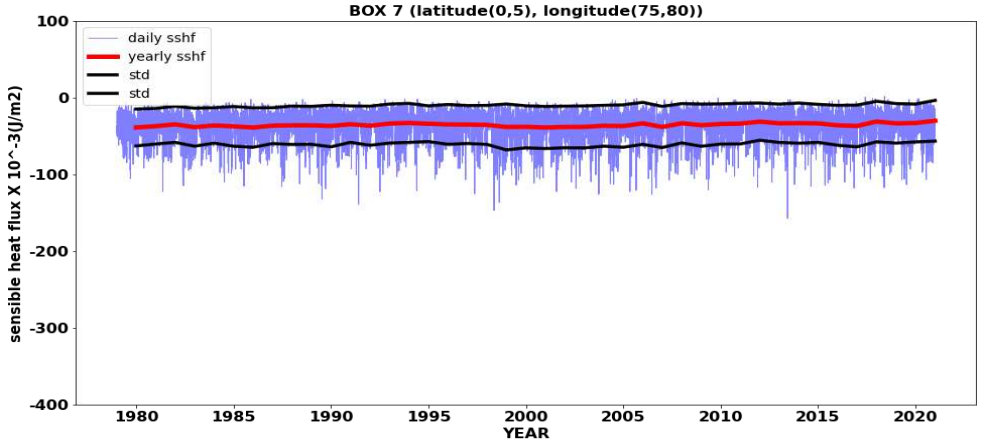

Figure 4.3 (a-g) Variation in Surface Sensible Heat Flux from 1979-2020 over the NIO

The transmission of heat-induced by the difference in temperature among the water surface and atmosphere is referred to as the sensible heat flux. The sensible heat flux (SSHF) variation over different boxes in the NIO is laid out in Figure 4.3 (a-g). The sensible heat flux in Box 1, has no clear increasing or decreasing trend and the SSHF values varied between -150 $x10^{-3}$ J/m^2 and 50 $x10^{-3}$ J/m^2. In Box 2, there were fluctuation in daily surface sensible heat flux values, but over the years, a trend cannot be established and the SSHF values over the region extended from -200 $x10^{-3}$ J/m^2 to 100 $x10^{-3}$ J/m^2. Over Box 3, the surface sensible heat flux in the region range between -200 $x10^{-3}$ J/m^2 and 50 $x10^{-3}$ J/m^2 where in some years it reached up to -400 $x10^{-3}$ J/m^2. The sensible heat flux depicted in Box 4 where the

heat flux was concentrated between -150 $x10^{-3}$ J/m^2 and 20 $x10^{-3}$ J/m^2 with no specific trend over the years. Box 5 was the region where the surface sensible heat flux was found between -150 $x10^{-3}$ J/m^2 and 20 $x10^{-3}$ J/m^2. Over Box 6, the daily sensible heat flux values were fluctuating with no pronounced variation over the years and the values over the region range between -150 $x10^{-3}$ J/m^2 and 100 $x10^{-3}$ J/m^2. Box 7 was the area where there was no pronounced trend in sensible heat flux over the years and the values range between -200 $x10^{-3}$ J/m^2 and 50 $x10^{-3}$ J/m^2. The pattern of daily SSHF and the standard deviation had an enormous change in each box. The daily SSHF variation was maximum over Box 3 whereas the standard deviation was observed to be the greatest over Box 6. The maximum variation in the SSHF was exhibited by the Northern BoB, whereas it was minimum in the Southern BoB and AS.

4.4 SPECIFIC HUMIDITY

a)

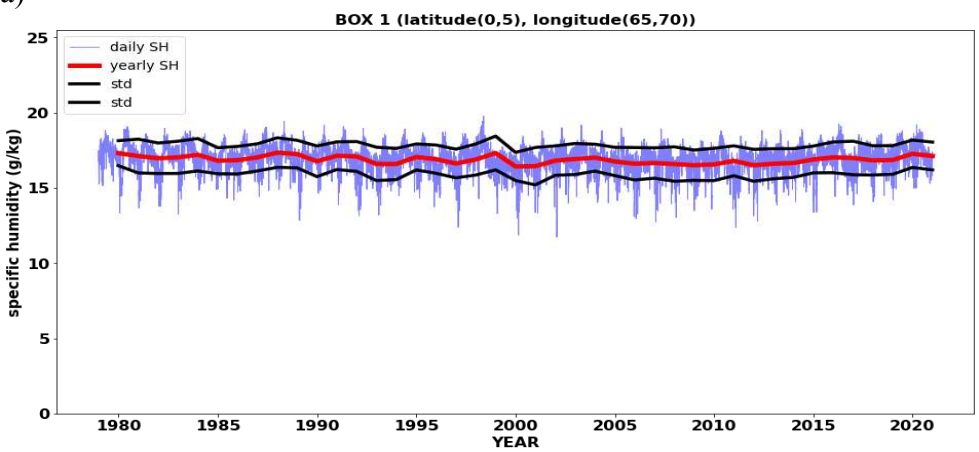

b)

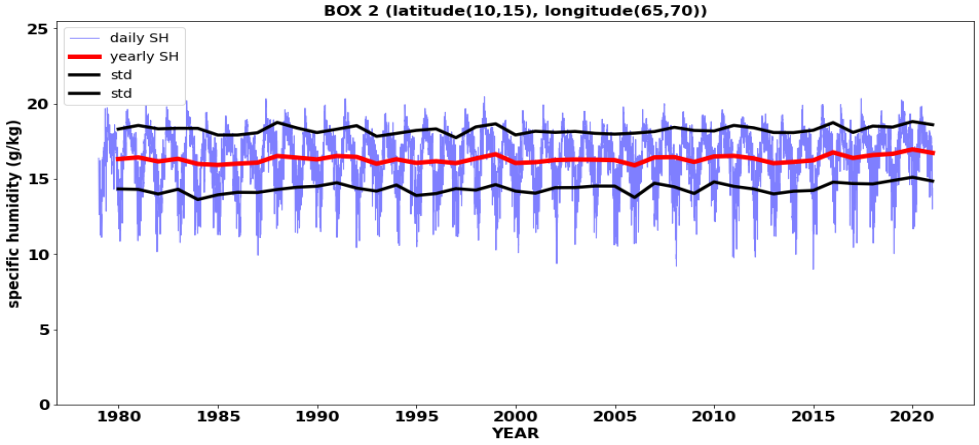
BOX 2 (latitude(10,15), longitude(65,70))
daily SH
yearly SH
std
std
specific humidity (g/kg)
YEAR

c)

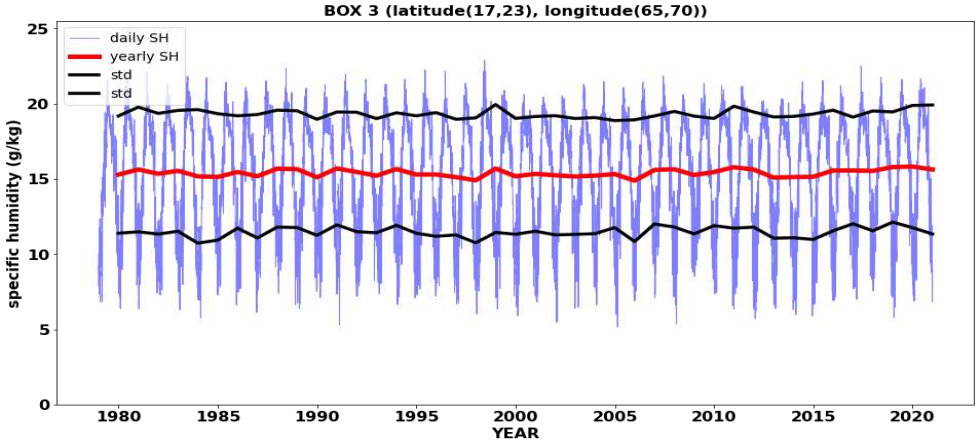
BOX 3 (latitude(17,23), longitude(65,70))
daily SH
yearly SH
std
std
specific humidity (g/kg)
YEAR

d)

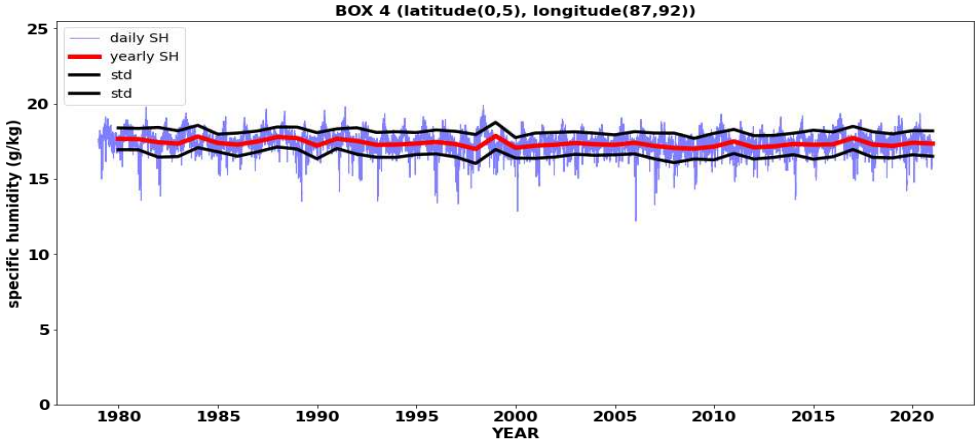
BOX 4 (latitude(0,5), longitude(87,92))
daily SH
yearly SH
std
std
specific humidity (g/kg)
YEAR

e)

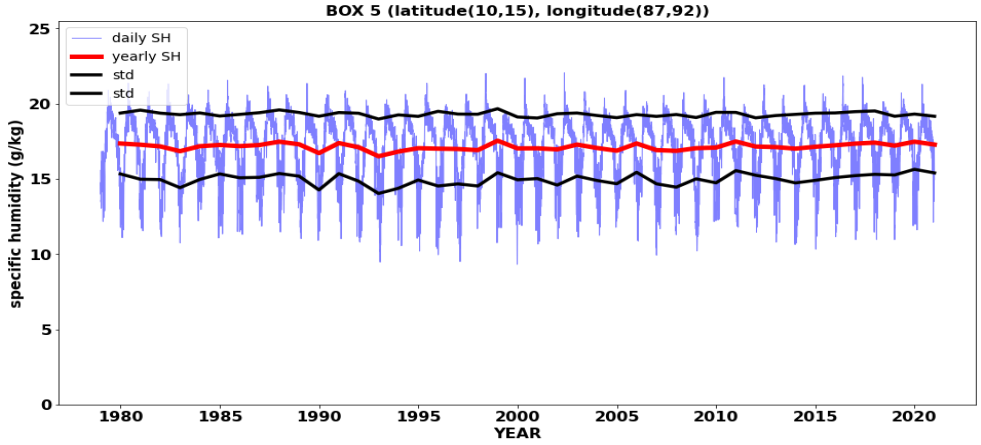

f)

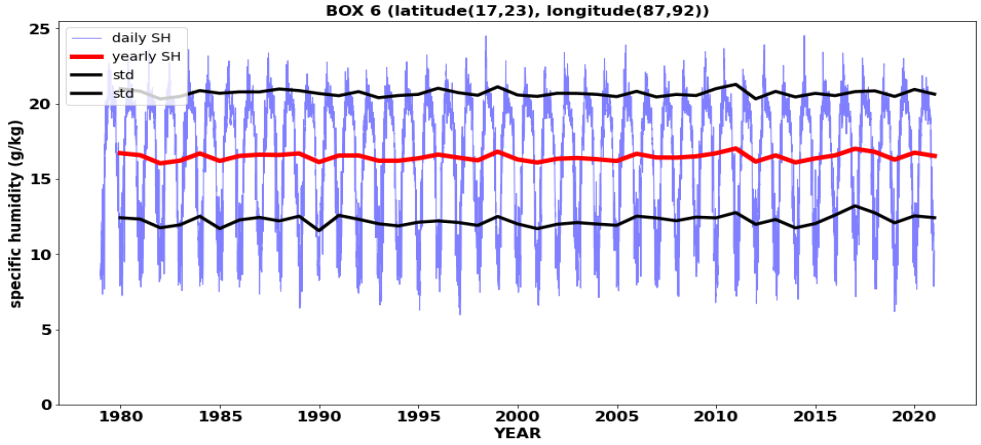

g)

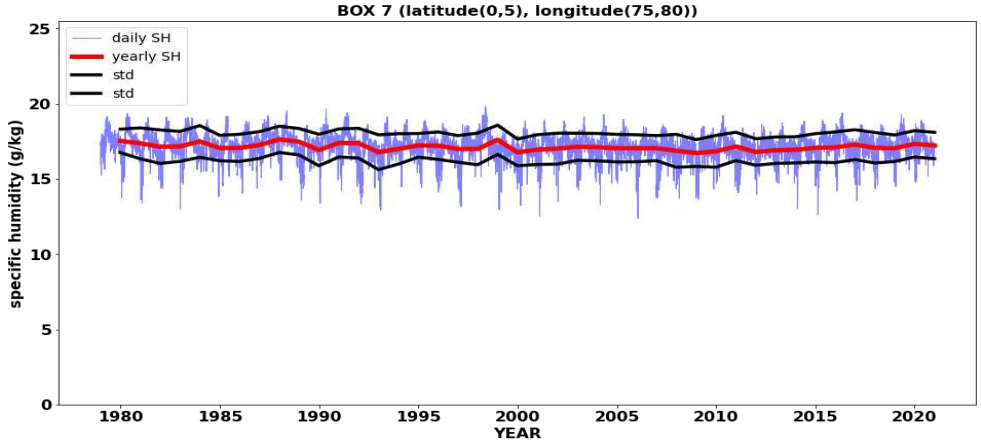

Figure 4.4 (a-g) Variation in Specific Humidity from 1979-2020 over the NIO

Specific Humidity (SH) is the ratio of the mass of water vapour to the total mass of the air parcel. It is means of evaluating how much moisture is present in

the air. The 7 boxes evaluate the specific humidity over the NIO. Box 1 depicted the specific humidity, where the daily specific humidity has fluctuations, but there was no pattern of increase or decrease in specific humidity over the years and this region had specific humidity between 10 g/kg to 20g/kg. Over Box 2, the daily fluctuation was found with the specific humidity values ranging between 8 g/kg to 22 g/kg. Box 3 has a huge variation in the specific humidity value compared to the other boxes where the values ranged between 5g/kg to 25 g/kg. The specific humidity illustrated in Box 4 had a pattern that was similar to that appeared in Box 1 with the values of specific humidity ranging between 10 g/kg and 20 g/kg. Box 5 had a similarity in the pattern to that of Box 2 with the values of Specific Humidity between 8 g/kg and 23 g/kg. The region in Box 6 where the trend in specific humidity was found to be related to that of Box 3 where the values extended between 5 g/kg and 25 g/kg. Box 7 had specific humidity values that were analogous to those in Box 1 and Box 4 where the values ranged from 10 g/kg and 20 g/kg. The daily Specific Humidity and the Standard Deviation was found to be distinct over each box, but they had a similar pattern of variation over Box 1, 4 and 7, Box 2 and 5, Box 3 and 6. The variation in SH was found to be greatest over the Northern BoB and AS, and Central BoB and AS also displayed variation, but not as exhibited by the Northern region.

4.5 WIND

a)

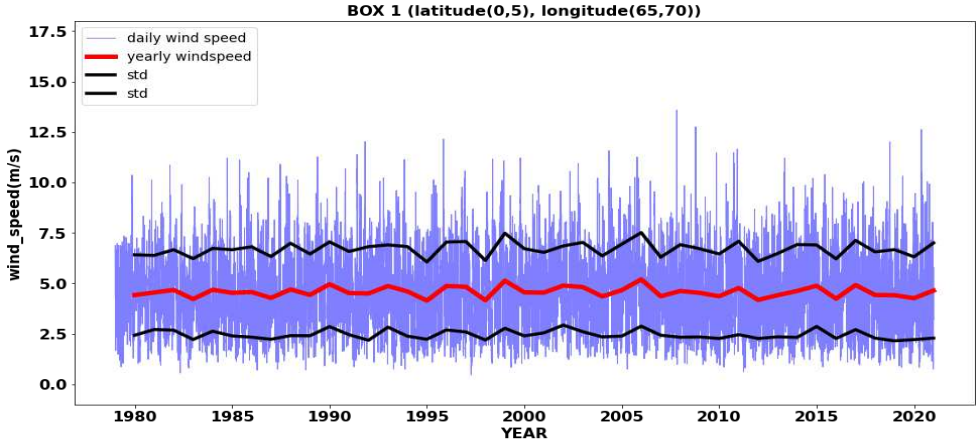
BOX 1 (latitude(0,5), longitude(65,70))
daily wind speed
yearly windspeed
std
std
wind_speed(m/s)
YEAR

b)

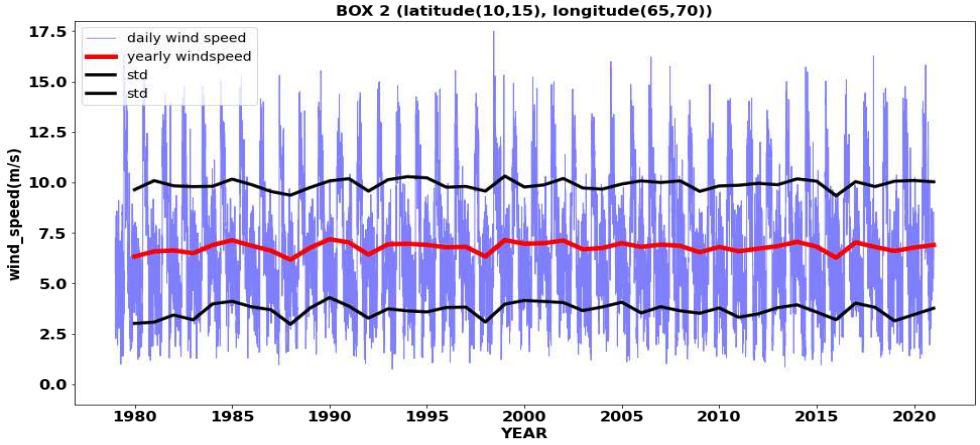
BOX 2 (latitude(10,15), longitude(65,70))
daily wind speed
yearly windspeed
std
std
wind_speed(m/s)
YEAR

c)

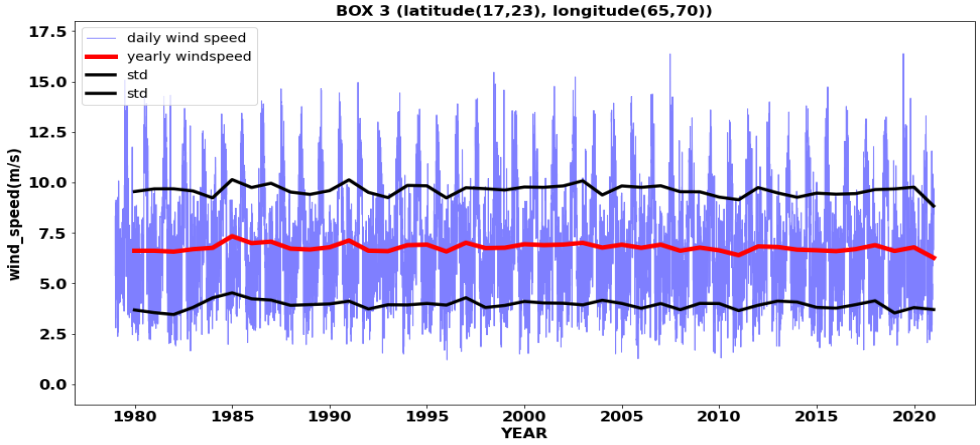
BOX 3 (latitude(17,23), longitude(65,70))
daily wind speed
yearly windspeed
std
std
wind_speed(m/s)
YEAR

d)

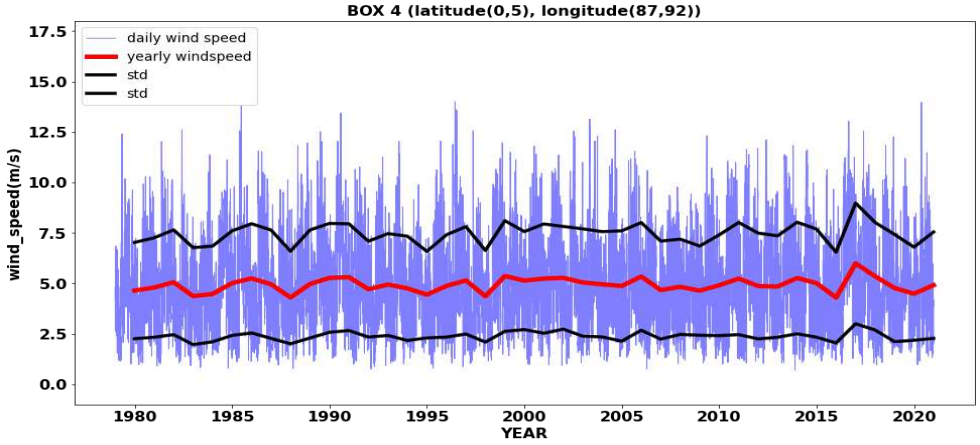
BOX 4 (latitude(0,5), longitude(87,92))
daily wind speed
yearly windspeed
std
std
wind_speed(m/s)
YEAR

e)

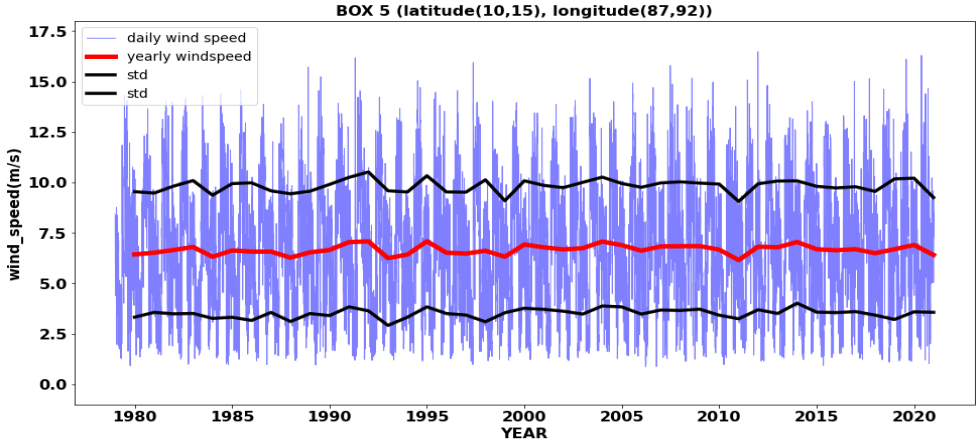
BOX 5 (latitude(10,15), longitude(87,92))
daily wind speed
yearly windspeed
std
std
wind_speed(m/s)
YEAR

f)

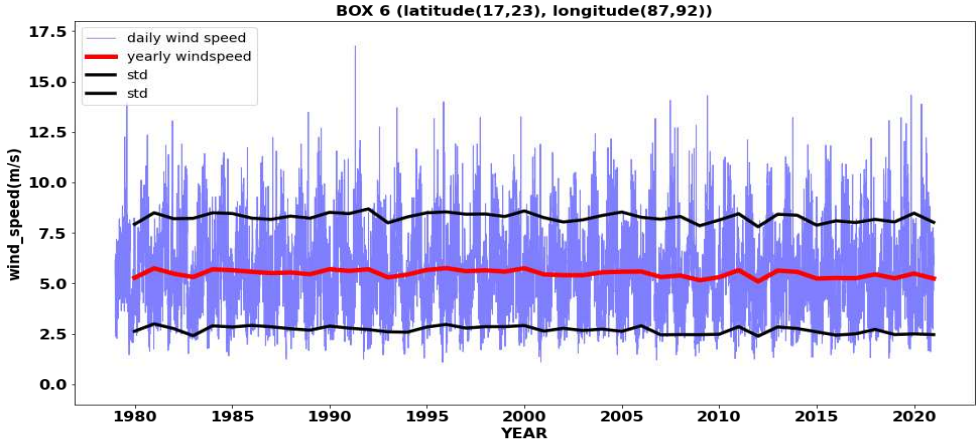
BOX 6 (latitude(17,23), longitude(87,92))
daily wind speed
yearly windspeed
std
std
wind_speed(m/s)
YEAR

g)

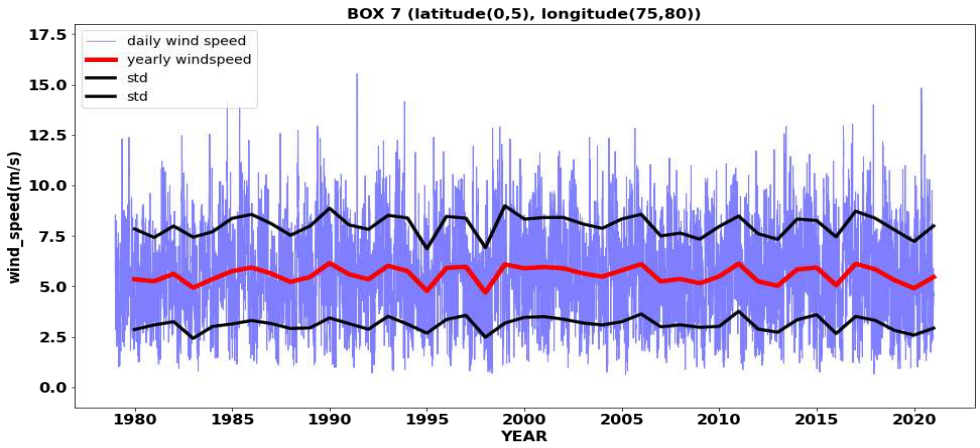

Figure 4.5 (a-g) Variation in Wind Speed from 1979-2020 over the NIO

Across the ocean, the exchange of moisture, heat, particles and gases between the ocean and atmosphere is regulated by the winds. The entire spectrum of water movement is influenced by the winds. The ocean and atmosphere interaction build and maintain the global and regional climate. Figure 4.5 (a-g) represent the wind speed over the NIO from 1979-2020. The wind speed over the Box 1 extended from 0.5 m/s to 15 m/s. There was no specific pattern of variation of wind speed in this region. Box 2 was the region where the wind speed ranged between 0.5 m/s and 18 m/s. The wind speed over Box 3 fluctuated from 0.5 m/s to 17 m/s. Box 4 has a pattern similar to that of Box 1 where the wind speed extended between 0.5 m/s and 15 m/s. Over Box 5, the wind speed varied between 0.5 m/s and 17 m/s where there is no specific pattern in the wind speed over the years. Box 6 have a wind speed that ranges between 0.5 m/s and 17.5 m/s. Over Box 7, the wind speed extended between 0.5 m/s and 16 m/s with fluctuation of wind speed over the years. The wind speed in all the boxes have a varying degree of fluctuations and the pattern in each box was different from one another. Similarly, the standard deviation in all the boxes was also distinct with maximum standard deviation found over Box 2 and Box 5. Considerable deviation of wind from the mean was observed in all the boxes, with the maximum variation exhibited by the Central AS and BoB.

4.6 TOTAL PRECIPITATION

a)

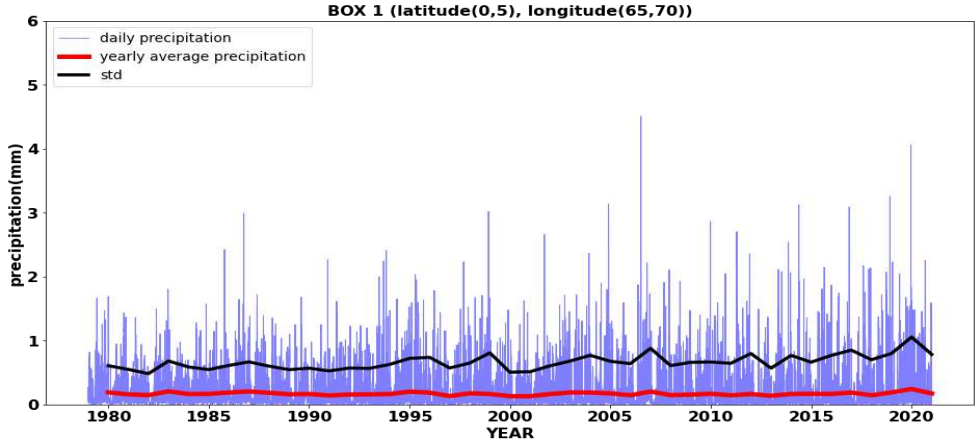

b)

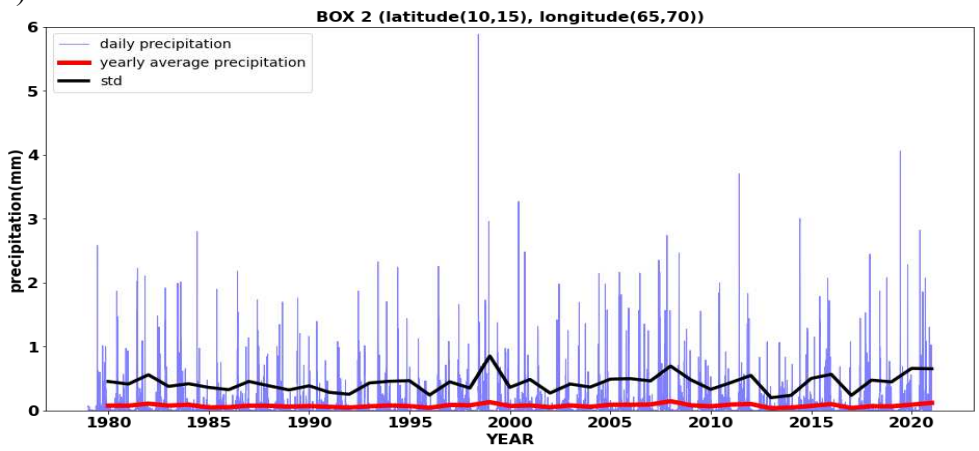

c)

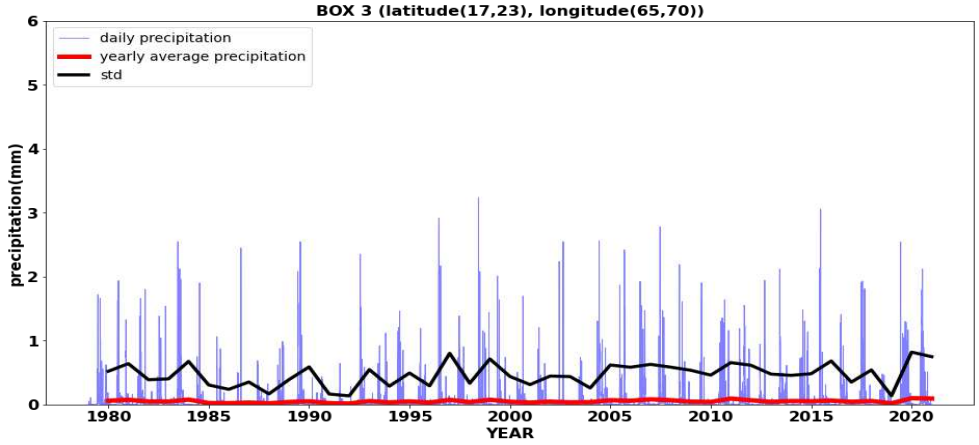

d)

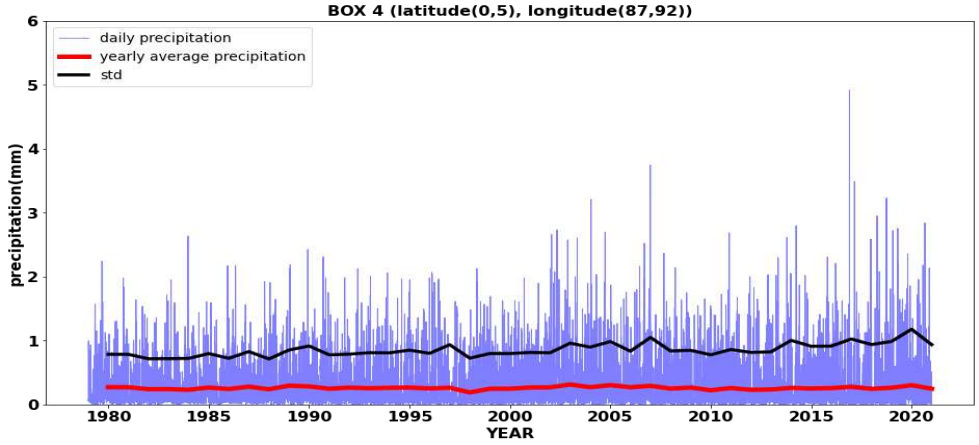
BOX 4 (latitude(0,5), longitude(87,92))
daily precipitation
yearly average precipitation
std
precipitation(mm)
YEAR
0
1
2
3
4
5
6
1980
1985
1990
1995
2000
2005
2010
2015
2020

e)

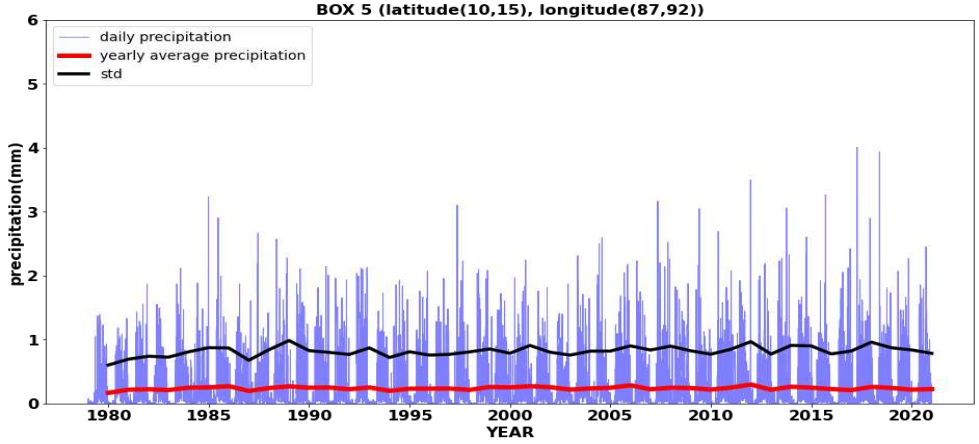
BOX 5 (latitude(10,15), longitude(87,92))
daily precipitation
yearly average precipitation
std
precipitation(mm)
YEAR
0
1
2
3
4
5
6
1980
1985
1990
1995
2000
2005
2010
2015
2020

f)

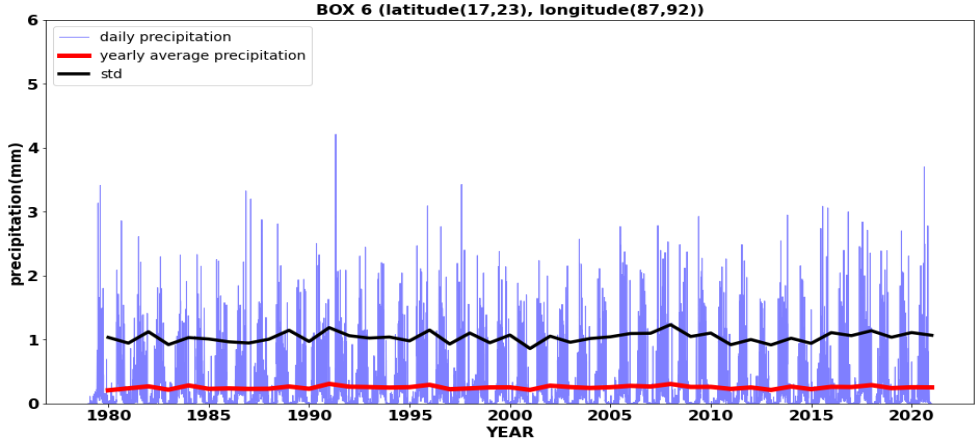
BOX 6 (latitude(17,23), longitude(87,92))
daily precipitation
yearly average precipitation
std
precipitation(mm)
YEAR
0
1
2
3
4
5
6
1980
1985
1990
1995
2000
2005
2010
2015
2020

g)

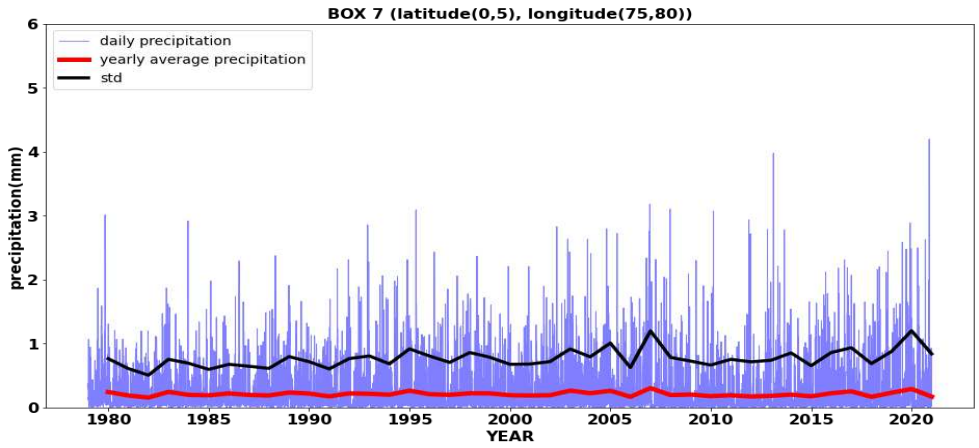

Figure 4.6 (a-g) Variation in Total Precipitation (mm/day) from 1979-2020 over the NIO

All across the planet, the precipitation patterns are influenced by the temperature of the ocean on account the atmosphere and ocean are interconnected. Figure 4.6 (a-g) illustrate the precipitation over different parts of the NIO. Box 1 is the region where the precipitation value ranges between 0 mm and 5 mm. Over the years, there was no pattern of increase in the amount of precipitation, but post-2005, the amount of precipitation was found to be greater than those before 2005 and also the years with the highest precipitation was recorded during 2006-07. Over Box 2, the precipitation extended between 0 mm and 6 mm. In this domain, the highest precipitation was documented in the interim of 1998-99. The precipitation in this region fluctuated with an increase in some and decrease in other years, but the number of years with greater precipitation had increased. In Box 3, the value of precipitation varied from 0 mm to 4 mm. It was the study region in the AS where the lowest amount of precipitation was recorded. The year in which the greatest precipitation was recorded was 1998-99. Box 4 is the region where the precipitation fluctuates between 0 mm and 5 mm. The highest precipitation in this region was recorded during 2017-18 and the years with greater precipitation has increased when compared to previous years. The precipitation over Box 5 had its values ranging between 0 mm and 4 mm and the number of years with more precipitation had increased from 2005 even though a clear increase in precipitation was not

documented. The year with the highest precipitation in this domain was 2017-18 followed by 2018-19. Box 6 was the region where the rainfall ranged from 0 mm to 5 mm and the highest amount of precipitation was recorded during 1991-92. Over Box 7, the precipitation extended from 0 mm to 5 mm. The years with the greater amount of precipitation increased from 2000 with the highest amount of precipitation in 2019-20 followed by 2013-14. The pattern of precipitation displayed that the BoB and Central Indian Ocean received a considerable amount of precipitation whereas, over the AS, only Southern AS had significant precipitation, while the precipitation was less over the Central and Northern AS.

4.7 EL NINO AND LA NINA YEARS

a)

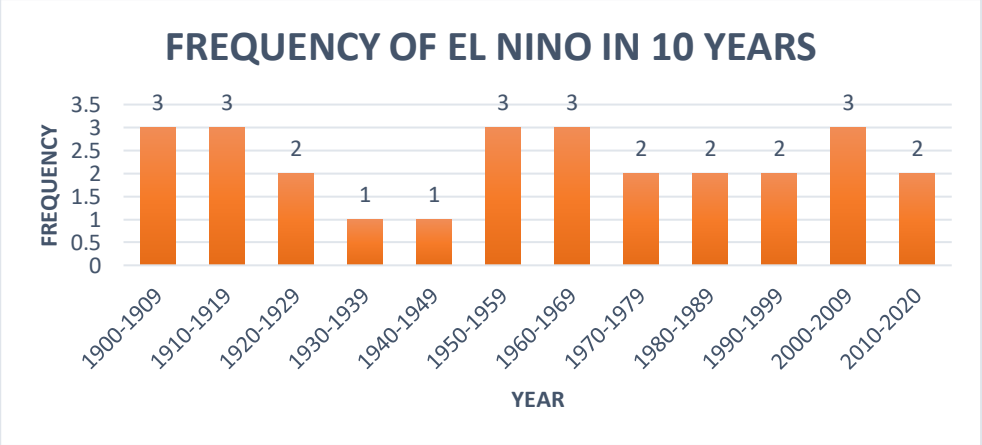

Figure 4.7 (a) Frequency of El Nino years during every 10 years from 1900-2020.

b)

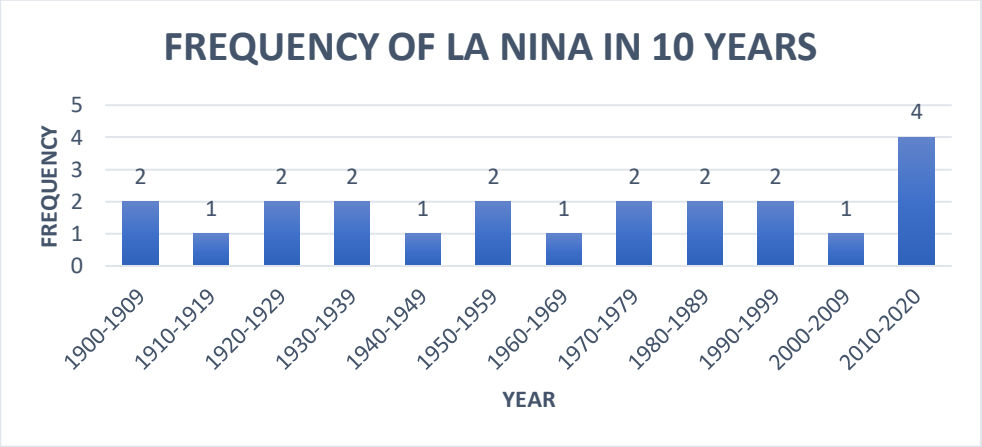

Figure 4.7 (b) Frequency of La Nina years during every 10 years from 1900-2020.

The warm and cold episodes of ENSO are recognised as El Nino and La Nina. ENSO is the repeating pattern of climate over the Eastern and Central Pacific Ocean that involves fluctuations in the Sea Surface Temperature, Sea level Pressure, Precipitation and upper and lower wind patterns. El Nino is a phenomenon in the Pacific Ocean that is characterised by warmer than usual sea surface temperatures. Figure 4.7 (a) illustrated the occurrence of El Nino within 10 years. A maximum of three El Nino events happened in the 10-year interval. Later 1950, within the 10 years, there was at least 2 El Nino events and a maximum of three episodes of El Nino. In the interim of 1930-1950, there were only 2 El Nino events formed whereas, after 1950, most of the 10-year interval had 2-3 El Nino occurrences.

La Nina is the cold phase of ENSO where the Pacific Ocean is characterised by cooler than normal sea surface temperature. The frequency of La Nina within 10 years from 1900-2000 was depicted in Figure 4.7 (b). A maximum of four La Nina episodes was formed in the course of 2010-2020 and at least one La Nina event had developed every 10 years.

4.7 A. SST ANOMALY DURING EL NINO AND LA NINA YEARS

a)

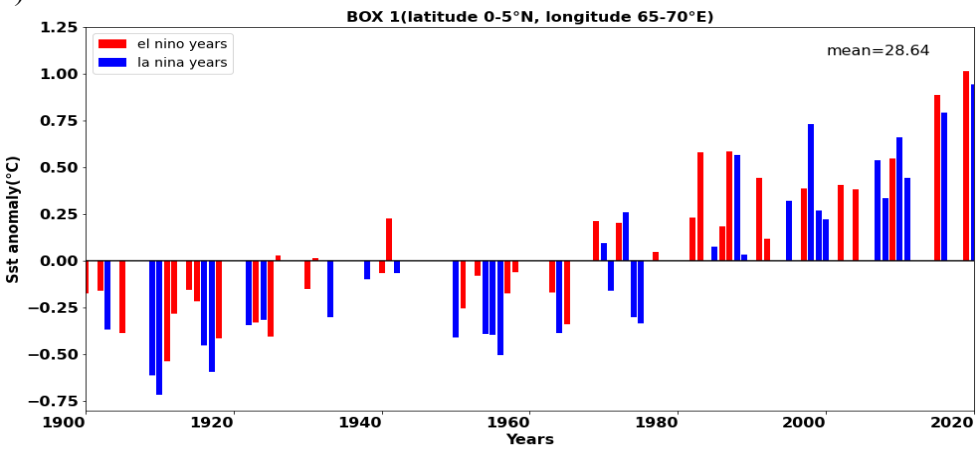
BOX 1(latitude 0-5°N, longitude 65-70°E)
el nino years
la nina years
mean=28.64
Sst anomaly(°C)
Years

b)

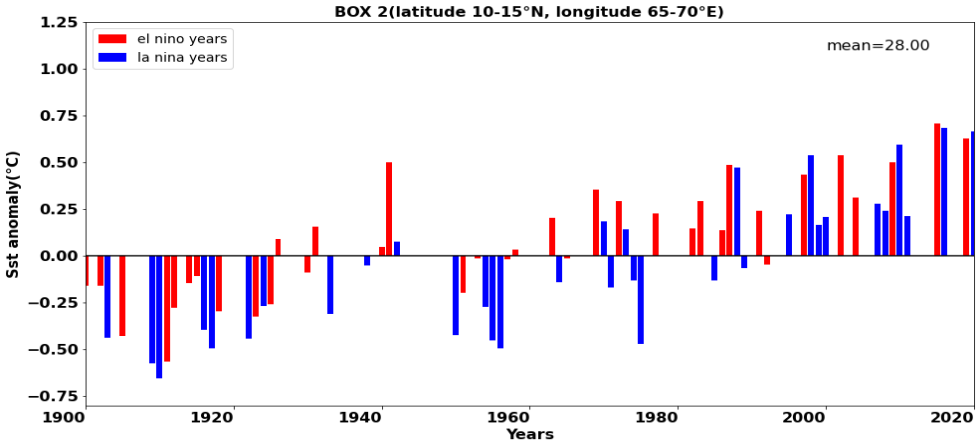
BOX 2(latitude 10-15°N, longitude 65-70°E)
el nino years
la nina years
mean=28.00
Sst anomaly(°C)
Years

c)

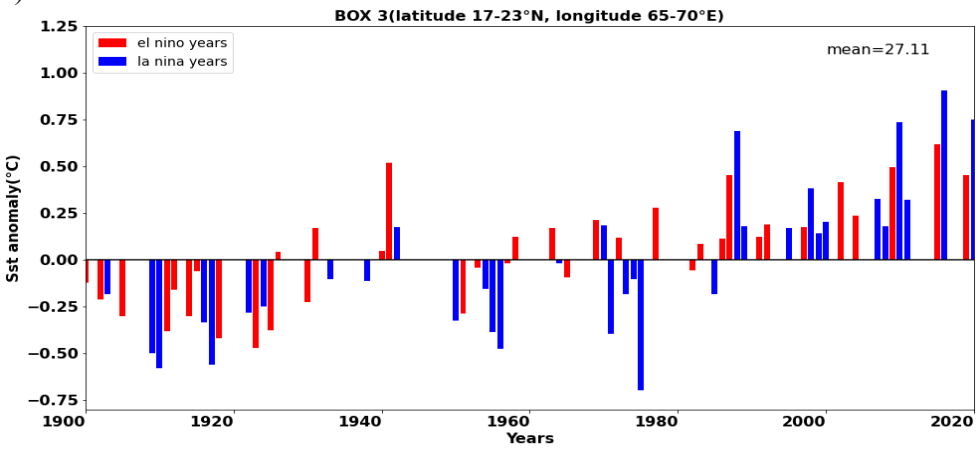
BOX 3(latitude 17-23°N, longitude 65-70°E)
el nino years
la nina years
mean=27.11
Sst anomaly(°C)
Years

d)

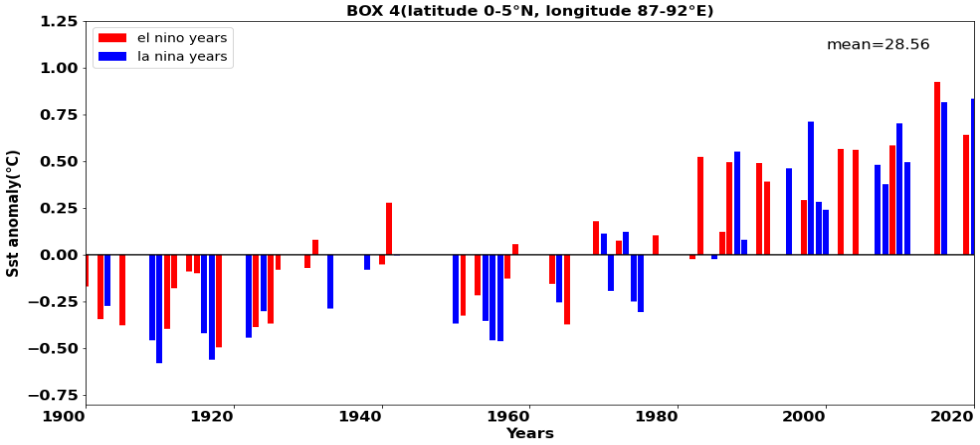
BOX 4(latitude 0-5°N, longitude 87-92°E)
el nino years
la nina years
mean=28.56
Sst anomaly(°C)
Years

e)

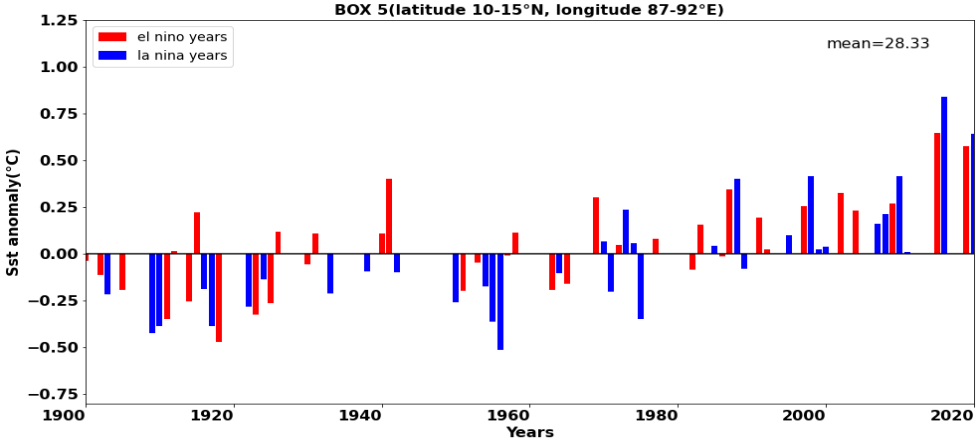
BOX 5(latitude 10-15°N, longitude 87-92°E)
el nino years
la nina years
mean=28.33
Sst anomaly(°C)
Years

f)

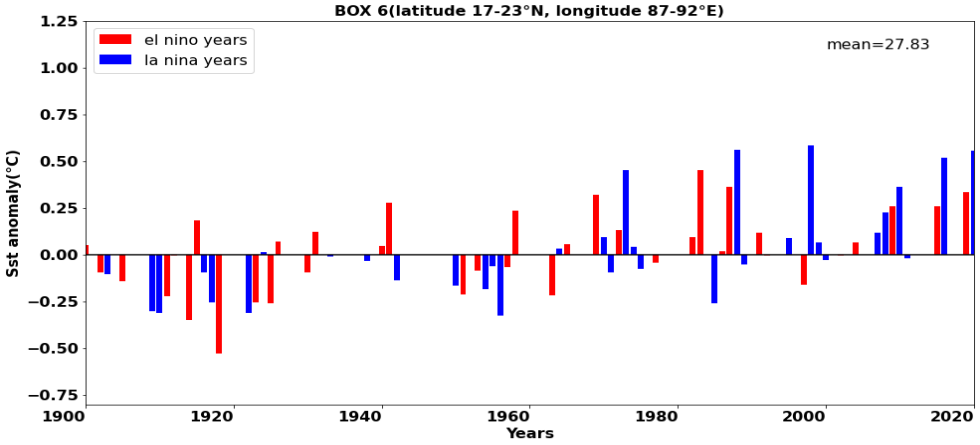
BOX 6(latitude 17-23°N, longitude 87-92°E)
el nino years
la nina years
mean=27.83
Sst anomaly(°C)
Years

g)

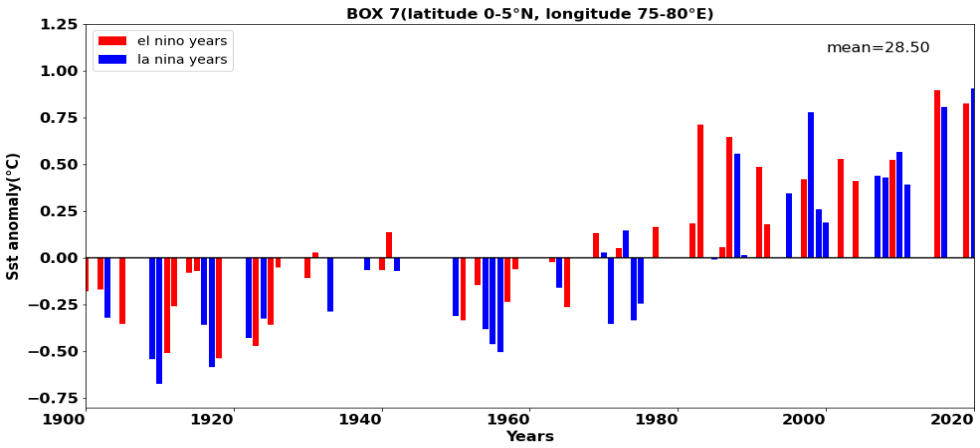

Figure 4.7 A (a-g) Sea Surface Temperature Anomaly over Northern Indian Ocean during El Nino and La Nina years from 1900-2020

The Sea Surface Temperature Anomaly (SSTA) is the departure of SST from the normal conditions. Figure 4.7 A (a-g) displays the SSTA over the NIO from 1900-2020. Box 1 displayed the SSTA range between -0.8°C and 1 °C from the mean SST of 28.64 °C. Before 1980, the SSTA over the region was negative. The SSTA value became less negative over the years and also there were some years with positive anomaly before 1980, notably during 1940-41 which was an El Nino year. After 1980, the SSTA was positive in this region and the values were more positive over the years. There was a positive trend in SSTA over this region. The greatest positive anomaly was during 2018-19 and the greatest negative anomaly was in 1908-09. In Box 2 where the SSTA range between -0.8 °C and 0.8 °C from the mean SST of 28 °C and there was an increasing trend of SSTA. In this region, negative SSTA values dominate prior to 1970 where there were some exceptions of a positive anomaly during that period. After 1970, most of the SSTA values were positive. A Positive anomaly was the highest during 2015-16 and the highest negative anomaly in this region was recorded during 1910-11. There appeared a positive trend in the SSTA over Box 3 where a continuous positive SSTA was identified after the 1980s and the SSTA over this region fluctuated between -0.8 °C and 1 °C from the mean SST of 27.11. Most of the years before 1980 exhibited a negative SSTA where some of them displayed a positive SSTA. The maximum

positive SSTA was observed during 2016-17 which was a La Nina year and the maximum negative SSTA was noticed during 1975-76. Box 4 was the region where the SSTA value vary between -0.6 ^{o}C and 1 ^{o}C from the mean SST of 28.56 ^{o}C. There was a positive trend in SSTA over the region where the values were negative before 1980. After 1980, the values were positive with the highest positive SSTA occurred during 2015-16 and the highest negative SSTA during 1910. The SSTA over Box 5 displayed a positive trend with a continuous positive SSTA value after 1980 and the years before 1980 exhibited negative SSTA where some of them had positive SSTA value. The SSTA value in this region extended from -0.6 ^{o}C to 1 ^{o}C from the mean of 28.33 ^{o}C with the maximum positive SSTA value during 2015-16 and the maximum negative SSTA during 1956-57. There was a positive trend in SSTA over Box 6, where the SSTA value range between -0.6 ^{o}C to 0.7 ^{o}C from the mean SST of 27.83 ^{o}C. Though the SSTA over this region was exhibiting an increasing trend, the SSTA was less positive when compared to other regions. The maximum positive SSTA was identified during 1998-99 which was much less when in comparison with other boxes and the maximum negative SSTA was observed during 1918-19. In Box 7 where the SSTA values fluctuated between -0.7^{o}C and 1 ^{o}C from the mean SST of 28.50 ^{o}C. There was a clear positive trend with the positive SSTA values after 1980. The greatest positive SSTA was witnessed during 2019-20 and the greatest negative SSTA was observed during 1910-11.

4.7 B. NINO 3.4 SST ANOMALY

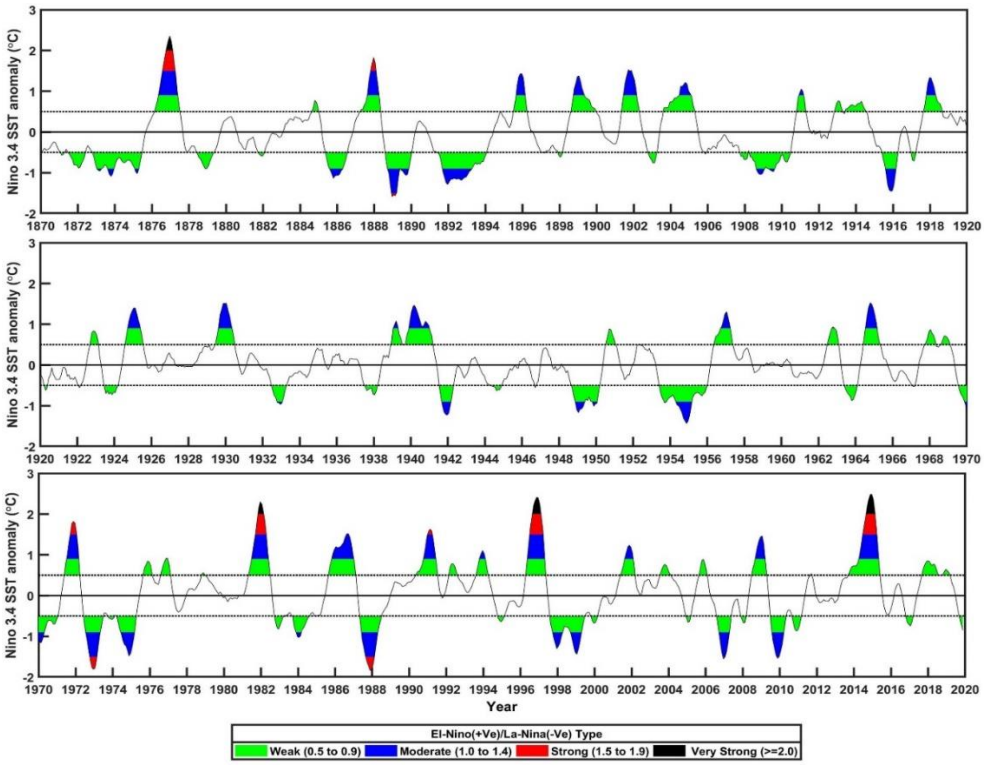

Figure 4.7 B El Nino and La Nina SST anomaly from 1870-2020

Figure 4.7 B illustrated the SST anomaly at the time of El Nino and La Nina. The anomaly that was observed to be greater than 0.5 ^{o}C was recognized as the El Nino year, whereas those below -0.5 ^{o}C was known to be the La Nina years. The green colour represented the Weak El Nino and Weak La Nina where the SST range from 0.5 to 0.9^{o}C and -0.5 to -0.9 ^{o}C respectively. The Moderate El Nino and Moderate La Nina were represented in blue colour where the SST anomaly was within 1and 1.4 ^{o}C and -1 and -1.4 ^{o}C. The SST anomaly was between 1.5 – 1.9 ^{o}C during Strong El Nino and -1.5 to -1.9 ^{o}C at the time of Strong La Nina, which was depicted in red colour in Figure 4.7 B. The black colour displayed the Very Strong El Nino and Very Strong La Nina, where the SST anomaly was above 2 ^{o}C and -2 ^{o}C. In the interim of 1870-1920, there observed only one Very Strong El Nino and two Strong El Nino events, however, there were only Moderate La Nina events identified during this period. From 1920-1970, the occurrence of El Nino and La

Nina was limited and also the intensity of the events was small, i.e. there were only Weak and Moderate El Nino and La Nina events. Throughout 1970-2020, there was the occurrence of three Very Strong El Nino events and four Strong El Nino events, while there were 2 Strong La Nina events observed within this time.

4.7 C. PROBABILITY DISTRIBUTION OF EL NINO AND LA NINA

a)

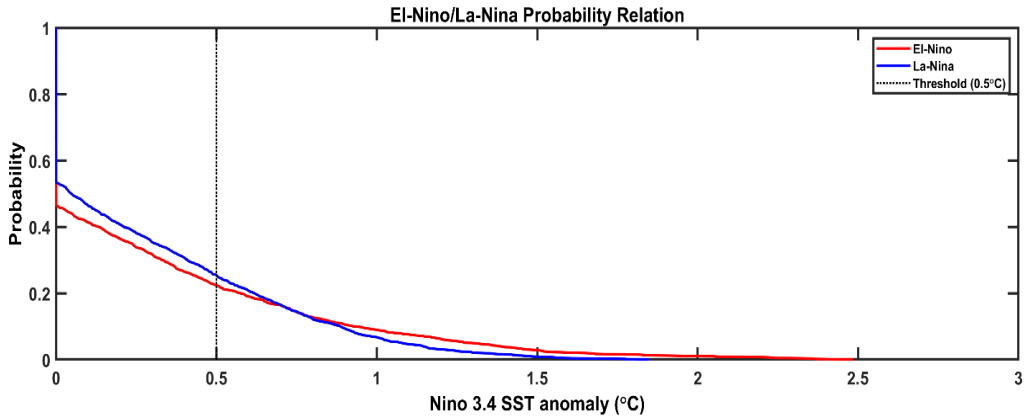

b)

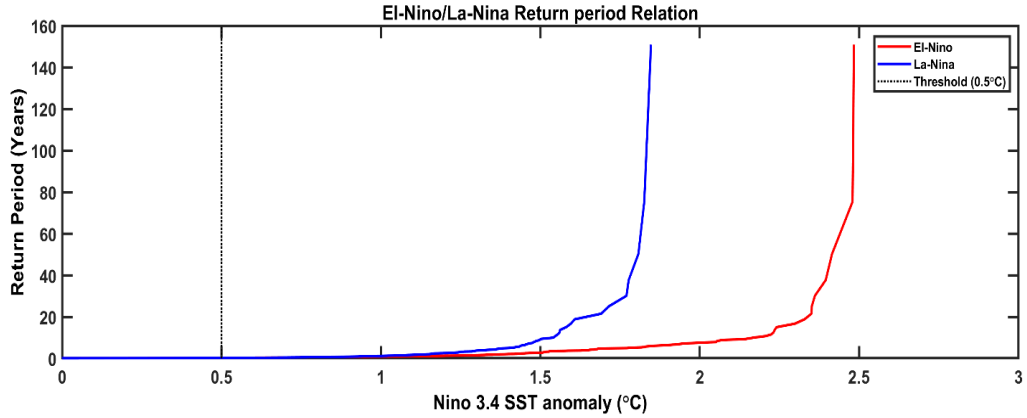

c)

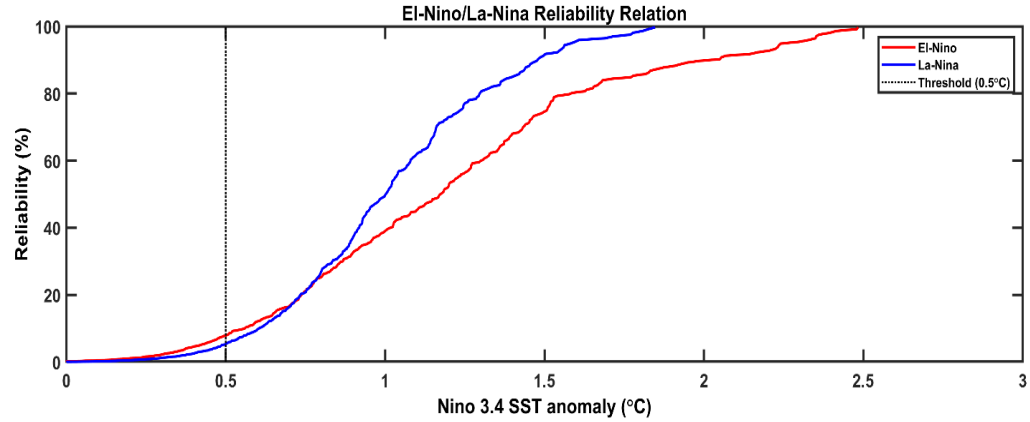

d)

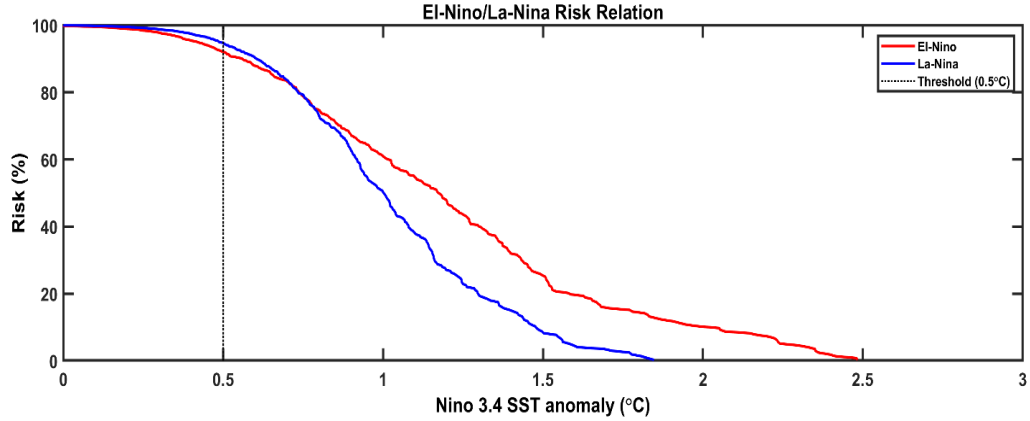

Figure 4.7 C (a) Total Probability of occurrence El-Nino/La-Nina during the past 150 years, (b) Return period of El-Nino/La-Nina, (c) Reliability of El-Nino/La-Nina, (d) Risk of El-Nino/La-Nina

Figure 4.7 C (a-d) illustrated the probability of occurrence of El Nino and La Nina, the return period, the reliability and risk of El Nino and La Nina events. The threshold value was considered as 0.5 ^{o}C. The analysis presented that the probability of occurrence of El Nino with the threshold value of SST anomaly was about 20%, whereas there was a 25% probability of occurrence of La Nina with threshold SST anomaly. There was less than a 20% probability identified for the occurrence of Weak El Nino and Weak La Nina (0.5 – 0.9 ^{o}C). Less than 10% probability was examined for Moderate El Nino and La Nina events (1 – 1.5 ^{o}C),

where the probability of moderate El Nino was a bit greater than that of moderate La Nina events. The was no probability of Strong La Nina events, while there was a small probability of occurrence of Strong El Nino event (1.5 - 2 ^{o}C). Figure 4.7 C (b) depicted the return period of El Nino and La Nina, which exhibited that the Weak El Nino and Weak La Nina can happen every year, as the return period was observed to be zero. The return period of Moderate El Nino was identified to be about 3 years; however, the return period of Moderate La Nina was observed to be about 10 years. Strong El Nino was examined to appear within 5 years, whereas the Strong La Nina events were observed to be within 30 and 160 years. There was no probability of occurrence of Very Strong La Nina, while the Very Strong El Nino was identified with the return period between 10 and 160 years. Figure 4.7 C (c) exhibited the reliability of El Nino and La Nina events. The reliability of Weak El Nino was 5-40%, while that of Weak La Nina was 0-50%. There identified 40-80% reliability of Moderate El Nino and the reliability of Strong El Nino was within 80-90%. The Moderate La Nina presented 50-90% reliability. There observed 90-100% reliability for Strong La Nina and Very Strong El Nino events. The Risk of El Nino and La Nina events was displayed in Figure 4.7 C (d). The risk was identified to be maximum for Weak El Nino (60-90%) and Weak La Nina (50-90%) events. The risk of Moderate La Nina events was 10-50%, whereas the Strong La Nina had a risk of 0-5%. The Moderate El Nino event had a risk of 60-20%. There was about 10-20% exhibited by the Strong El Nino events, whereas the Very Strong El Nino event displayed a risk of 0-10%. As the return period of Strong El Nino and La Nina events are high, the risk of the event was identified to be limited, with greater reliability.

e)

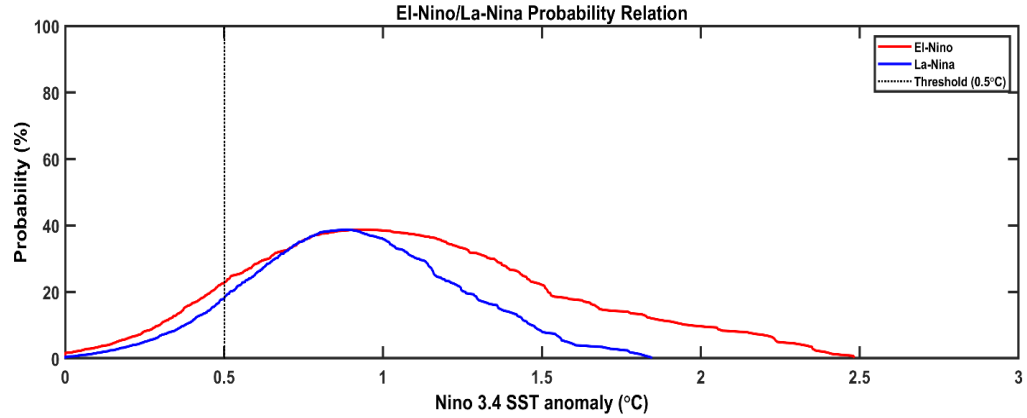

f)

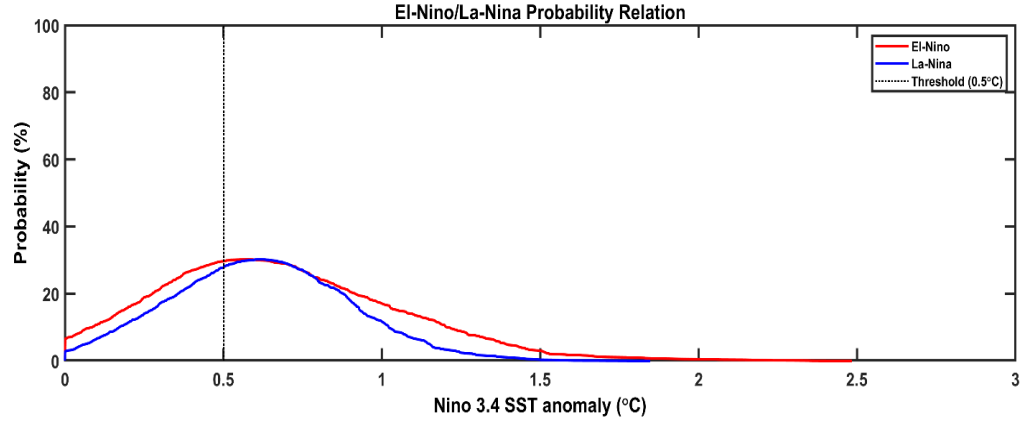

Figure 4.7 C (e) Probability distribution of occurring El-Nino/La-Nina once in the next successive ten years, (f) Probability distribution of occurring El-Nino/La-Nina twice in the next successive ten years

Figure 4.7 C (e) exhibited the probability of occurrence of El Nino and La Nina once in the next successive years. The Figure presented that, there is about 40% probability for the appearance of both Weak El Nino and Weak La Nina events once in the next successive ten years. There was about a 20-40% probability of formation of Moderate El Nino, whereas the probability of occurrence of Moderate La Nina event was 10-30%. The probability of Strong La Nina events once in net successive ten years was observed to be 0-10%. The Strong El Nino event had the probability of 10-20%, while the probability of a Very Strong El Nino event once

in the next ten years was found to be 0-10%. Figure 4.7 C (f) represented the probability of occurrence of El Nino and La Nina events twice in the next successive ten years. The probability of formation of Very Strong El Nino and Strong La Nina event twice in the next successive ten years was zero, whereas the probability of Strong El Nino was about 0-2%. There was about a 30% probability of appearance of Weak El Nino and La Nina events twice in the next successive ten years. The probability of occurrence of Moderate El Nino was 2-20%, whereas the probability of Moderate La Nina was 0-10%.

4.8 INDIAN OCEAN DIPOLE

a)

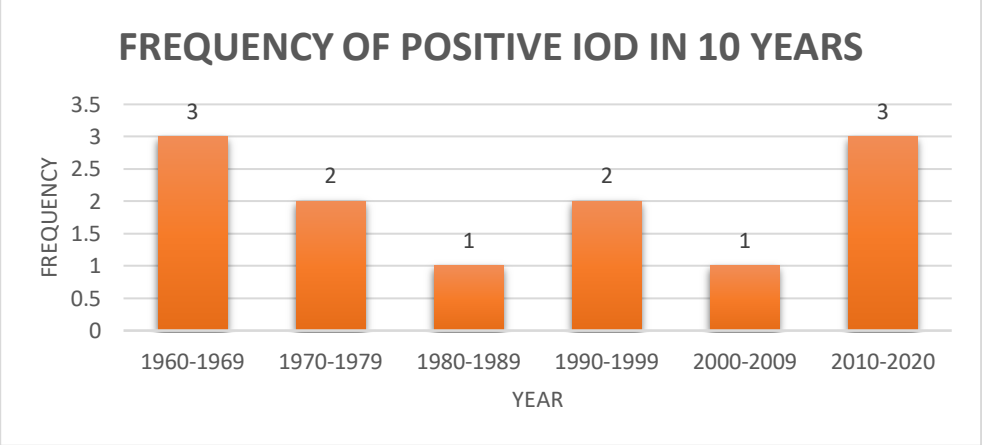

b)

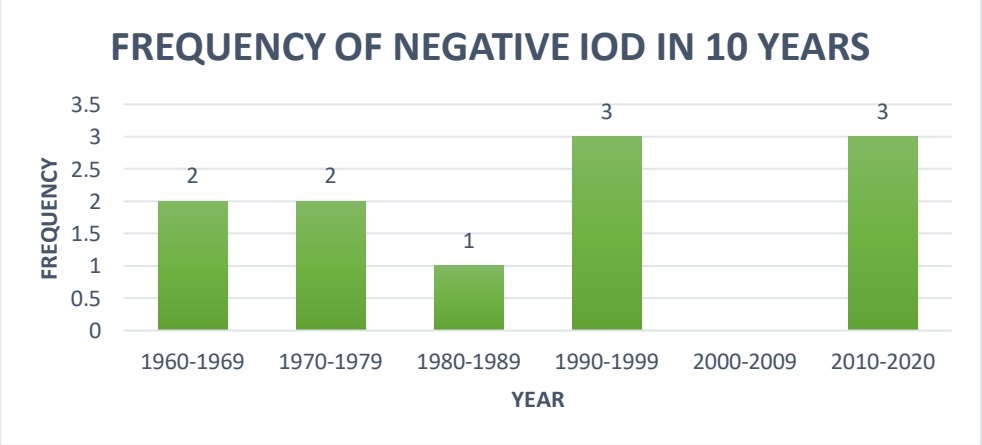

Figure 4.8 (a) Frequency of Positive IOD years during every 10 years from 1960-2020, (b) Frequency of Negative IOD years during every 10 years from 1960-2020

Indian Ocean Dipole (IOD) is the SST difference between the Western Indian Ocean and the Eastern Indian Ocean. Figure 4.8 (a) displayed the frequency of positive IOD events from 1960-2020. The frequency of Positive IOD was the greatest all along 1960-1969 and 2010-2020 and the minimum occurrence of Positive IOD years was in the interim of 1980-1989 and 2000-2009. There was a decrement in the incidence of Positive IOD till 1990 and then it had enhanced after 1990. Figure 4.8 (b) presented the frequency of negative IOD events from 1960-2020. The frequency of the negative IOD years was the highest during 1990-1999 and 2010-2020. There was the absence of negative IOD all along 2000-2009. There was also an increasing trend in the development of negative IOD years since 1990, but with an absence in 2000-2009.

4.9 MADDEN-JULIAN OSCILLATION

a)

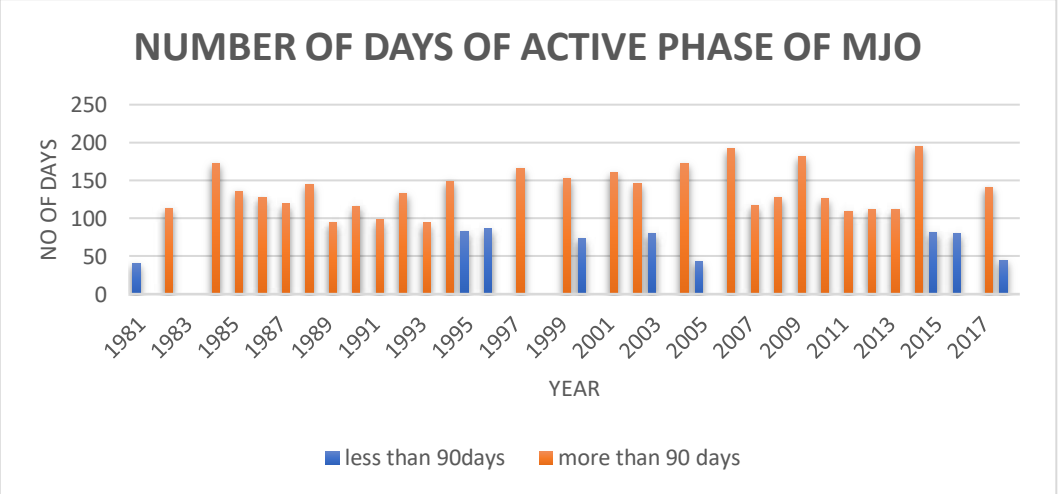

Figure 4.9 (a) Number of days of active phase of MJO from 1981-2018

Madden-Julian Oscillation (MJO) is an intra-seasonal oscillation characterised by eastward travelling disturbances of rainfall, clouds, pressure and winds that cross the globe. Figure 4.9 exhibit the number of days of the occurrence of MJO in each year from 1981-2018. After the 1990s, there was an increase in the number of days of MJO but after 2010, there were MJO events with a reduced number of days when compared to other years. In contrast, the MJO with the maximum number of days occurred during 2014 and then followed by 2006.

4.10 GREENHOUSE GAS

a)

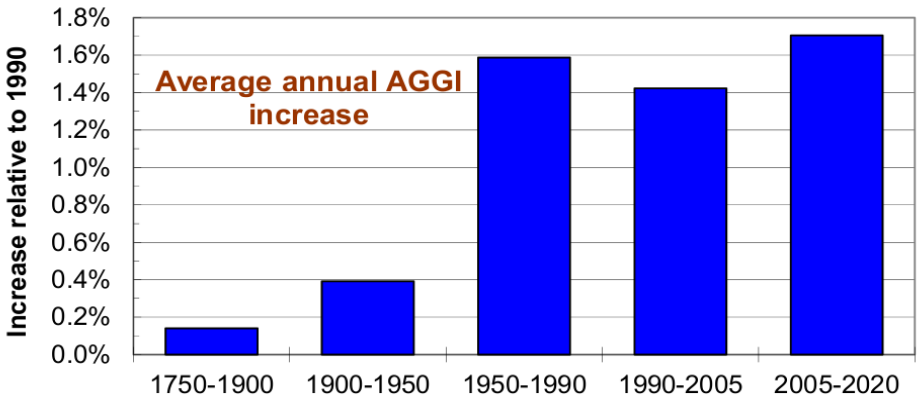

b)

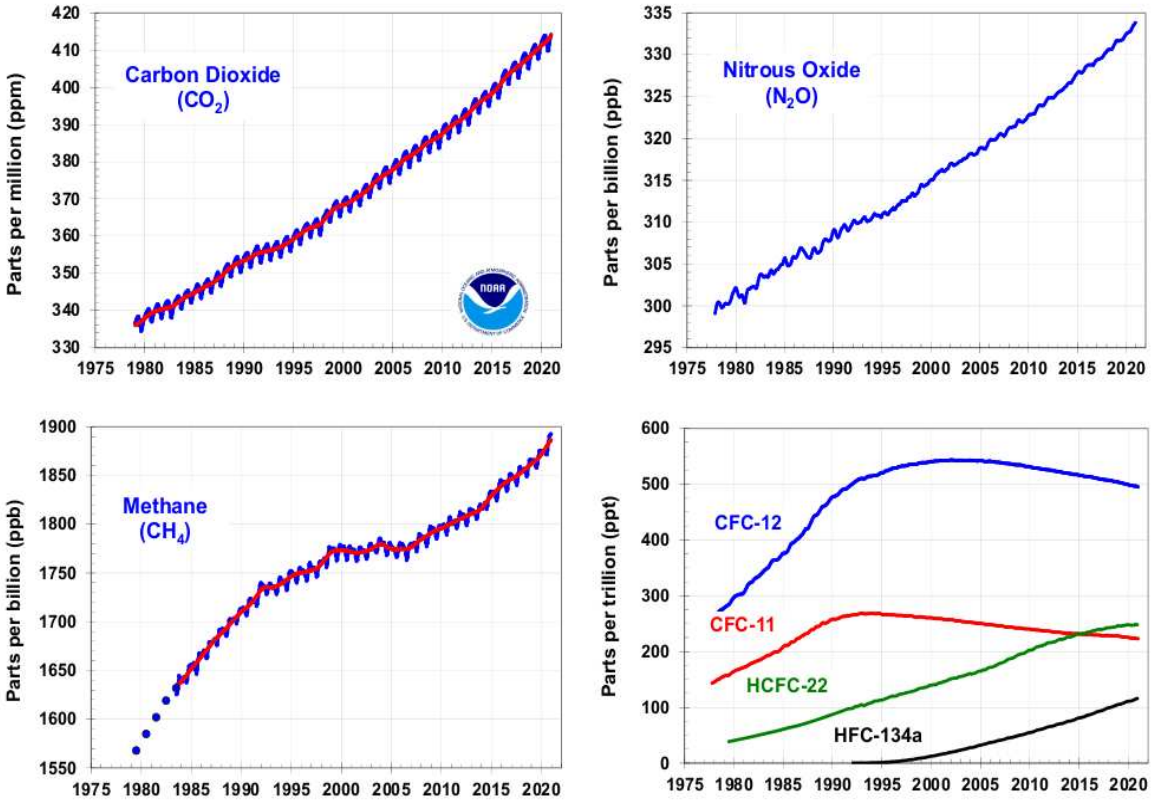

Figure 4.10 (a) Annual Greenhouse Gas Index from 1750-2020, (b) Global averaged abundance of greenhouse gases from 1979-2020 from NOAA

One of the dominant sources of anthropogenic climate change is the human emissions of carbon dioxide and other greenhouse gases. Figure 4.10 (a) represents the Annual Greenhouse Gas Index (AGGI) from 1750-2020 by National Oceanic and Atmospheric Administration (NOAA). The AGGI is the annual analysis from NOAA that examines the cumulative impact of greenhouse gases on the temperature of Earth. AGGI compares the effect of warming in each year due to greenhouse gases to that of 1990. 1990 was the year in which the signatories to the United Nations Kyoto Protocol committed to using as a baseline for emission contraction activities where the AGGI value was one. The figure represented the annual average greenhouse gas index increase relative to 1990. The AGGI has increased up to one after approximately 200 years, whereas from 1950 onwards there was a tremendous increase in the Greenhouse Gas Emissions.

Figure 4.10 (b) displayed the concentration as well as the trend of Greenhouse Gases in the atmosphere from 1979-2020. In 1979, the concentration of carbon dioxide was around 335 ppm whereas, in 2020, it was elevated up to around 415 ppm. In the 1980s, while the CO_2 levels climbed at a rate of nearly 1.6 ppm per year and 1.5 ppm per year in the 1990s, the rate has risen 2.4 ppm per year between 2009 and 2020. From 2020-2021, the CO_2 increase per year was 2.50 ± 0.08 ppm which was greater than the preceding decade's average and considerably larger than the prior two decades (NOAA). The concentration of nitrous oxide has risen over the years. In 1979, the concentration was around 298 ppb, wherein in 2020, it was found to be around 335 ppb. The methane concentration was found to have an overall increase, but from 1983-1999, there was a decrease in the methane concentration. In 1979, the concentration was around 1550 ppb whereas it approached 1900 ppb by 2020. In the interim of 1999-2006, the methane concentration was nearly constant whereas it started to elevate again from 2007. The representation of halogenated compounds including CFC, HFC, HCFC suggests that in the beginning, the CFCs had an increasing trend, but further there was a decrease in their concentration whereas the HCFC and the HFC displayed an increase in their concentration particularly after the 1990s.

4.11 FREQUENCY OF DEPRESSIONS, CYCLONIC STORMS AND SEVERE CYCLONIC STORMS OVER NORTHERN INDIAN OCEAN

a)

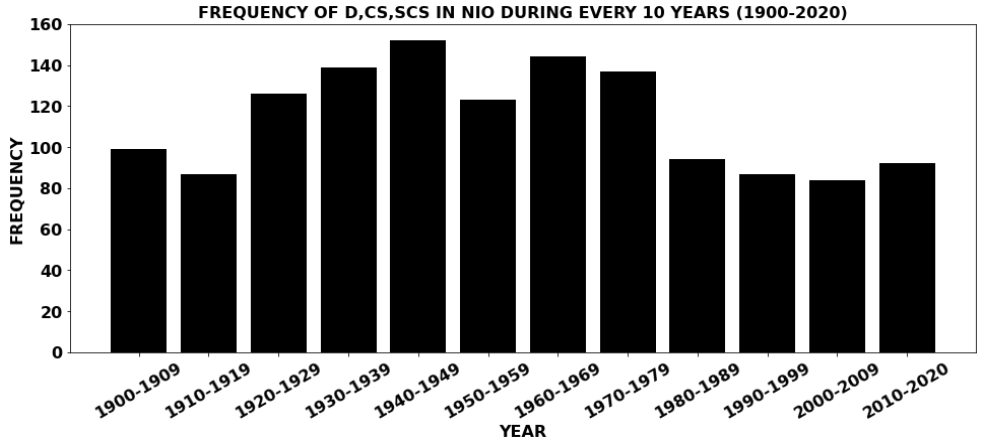

b)

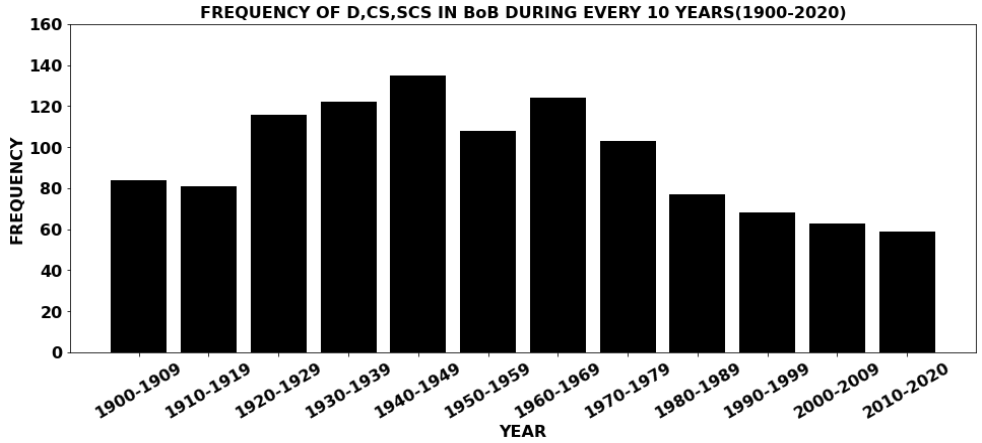

c)

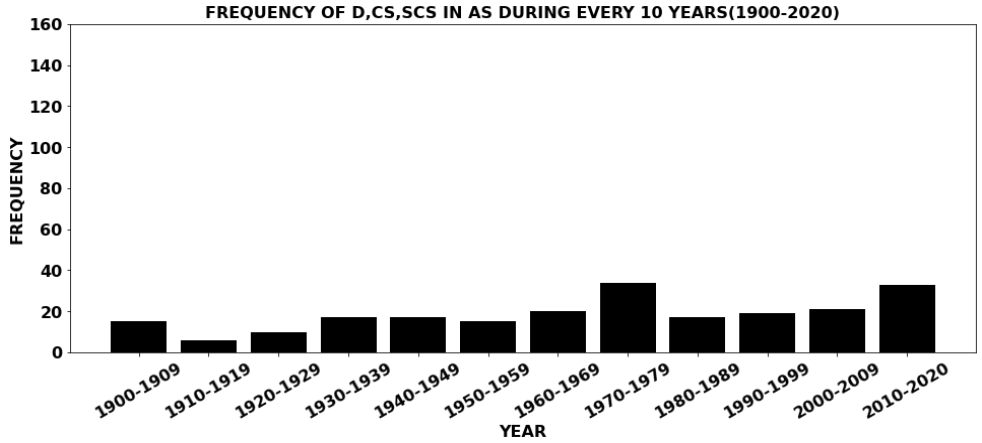

Figure 4.11 (a) Frequency of depressions, cyclonic storms and severe cyclonic storms over Northern Indian Ocean during each 10 year from 1900-2020, (b) Frequency of depressions, cyclonic storms and severe cyclonic storms over Bay of Bengal during each 10 year from 1900-2020, (c) Frequency of depressions, cyclonic storms and severe cyclonic storms over Arabian Sea in each 10 year from 1900-2020.

The frequency of Depressions, Cyclonic Storms and Severe Cyclonic Storms formed over the NIO every 10 years was analysed. Figure 4.11(a) illustrated the Frequency of cyclonic disturbances over the NIO. The frequency was analysed every ten years from 1900 to 2020. The figure revealed that the total number of cyclonic disturbances over the NIO initially had an increasing trend. The frequency of cyclonic disturbances was maximum in the course of 1940-1949 with the occurrence of about 152 cyclonic disturbances. There was a decline in the occurrence of cyclonic disturbances in the year following 1970, whereas it had a slight enhancement all along 2010-2020 compared to that of the previous year. In Figure 4.11 (b), the frequency of Depressions, Cyclonic Storms and Severe Cyclonic Storms over the BoB was depicted. On this spot, the maximum occurrence of 135 cyclonic disturbances was recorded in the interim of 1940-1949. There was a reduction in the incidence of Cyclonic disturbances over the BoB in the years after 1970. The appearance of Depressions, Cyclonic Storms and Severe Cyclonic Storms in the AS was laid out in Figure 4.11 (c). In this region, the occurrence of cyclonic disturbances was lesser, compared to that of the BoB. The emergence of cyclonic disturbance was very limited at the beginning, whereas development in the occurrence of cyclonic disturbances was examined over the years. The highest appearance of 34 cyclonic disturbances over the AS was throughout 1970-1979. There was a sudden decline in the formation of cyclonic disturbances in the course of 1980-1989, however thereafter an enhancement was detected with another maximum of 33 cyclonic disturbances throughout 2010-2020.

4.12 FREQUENCY OF DEPRESSIONS OVER NORTHERN INDIAN OCEAN

a)

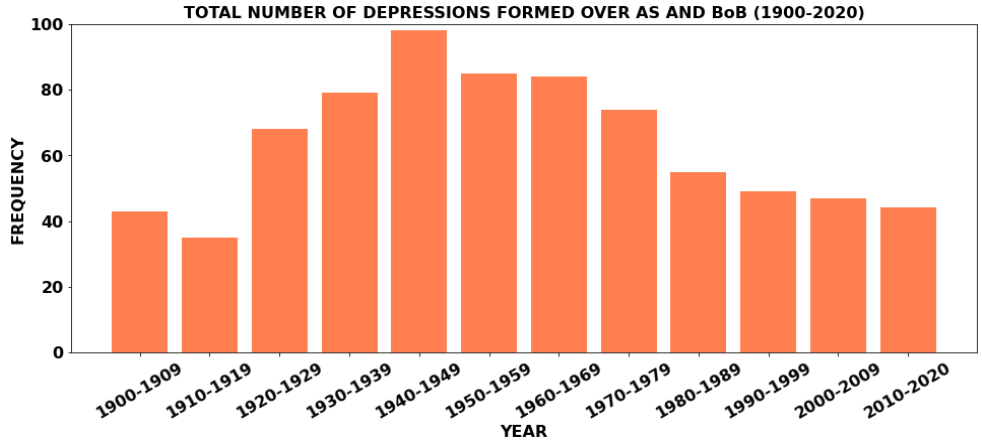

b)

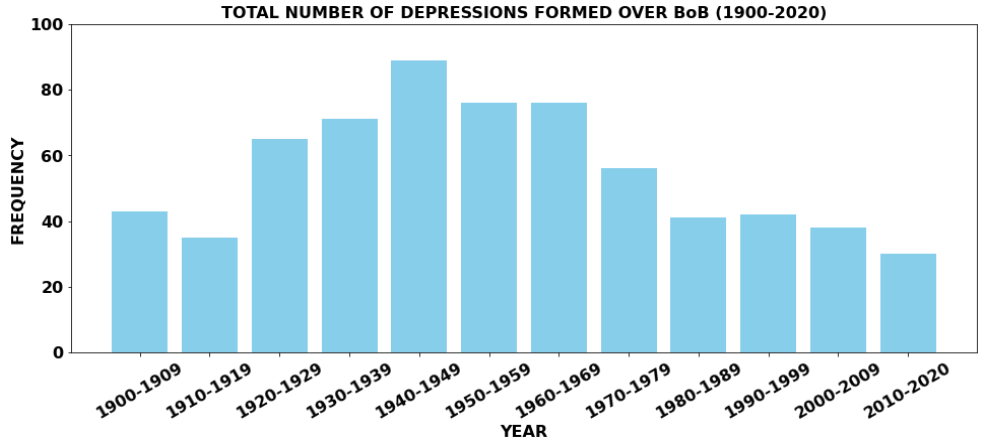

c)

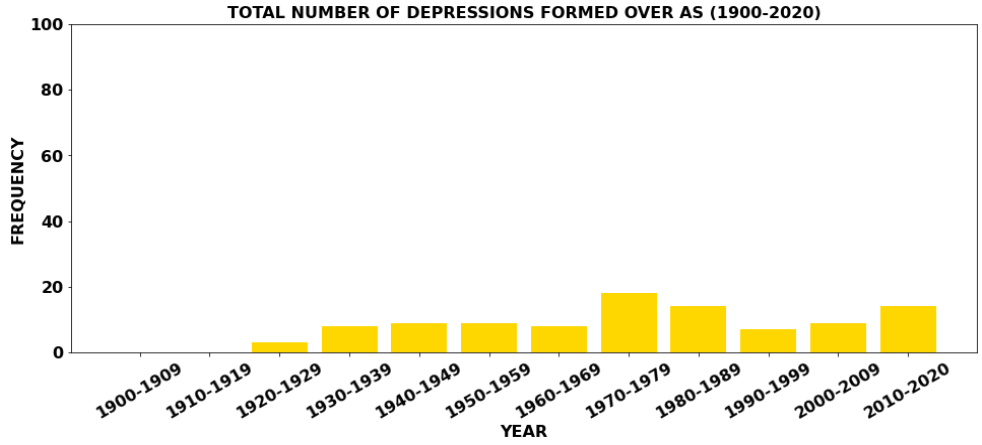

Figure 4.12 (a) Frequency of Depressions over Northern Indian Ocean in each 10 year from 1900-2020, (b) Frequency of Depressions over Bay of Bengal in each 10 year from 1900-2020, (c) Frequency of Depressions over Arabian Sea in each 10 year from 1900-2020.

The total Depressions formed over the NIO every ten years in the course of 1900-2020 was presented in Figure 4.12 (a). A considerable amount of depressions was developed in the NIO. Prior to 1950, there was an escalation in the emergence of depressions with the largest number of 98 depressions appeared in the time of 1940-49. The frequency of Depressions later 1950 has declined over the years with about 44 Depressions that was developed all along 2010-2020. Figure 4.12 (b) illustrated the frequency of Depressions every 10 years from 1900-2020 that developed over the BoB. There were about 89 depressions during 1940-1949, which was the period with the greatest number of Depressions ever recorded in the BoB. In BoB just before 1949, there was an enhancement in the frequency of Depressions over the years whereas it was identified to be declining after 1949 with the least occurrence of 30 Depressions in the interim of 2010-2020. The frequency of Depressions every 10 years from 1900-2020 over the AS was displayed in Figure 4.12 (c). The pattern of appearance of Depressions over the AS was completely different from that of the BoB. It was quite interesting to examine that there were no Depressions in the AS from 1900-1924. From 1925, few Depressions started to originate over the AS and a maximum of 18 depressions were observed all along 1970-1979. Later, the occurrence of depressions had an increment in comparison with that of years before 1970.

4.13 FREQUENCY OF CYCLONIC STORMS OVER NORTHERN INDIAN OCEAN

a)

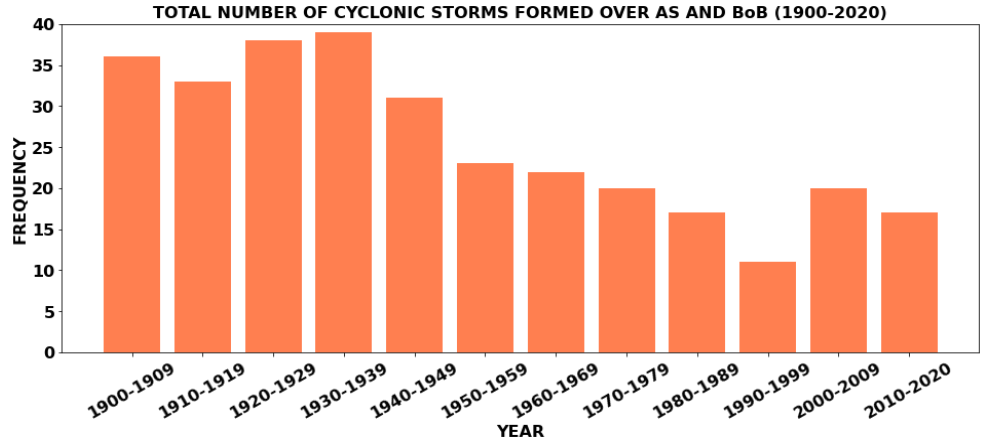

b)

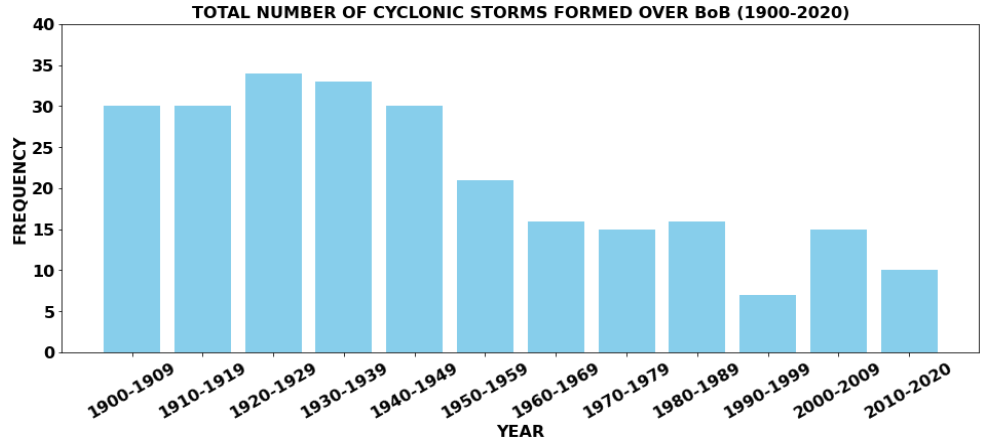

c)

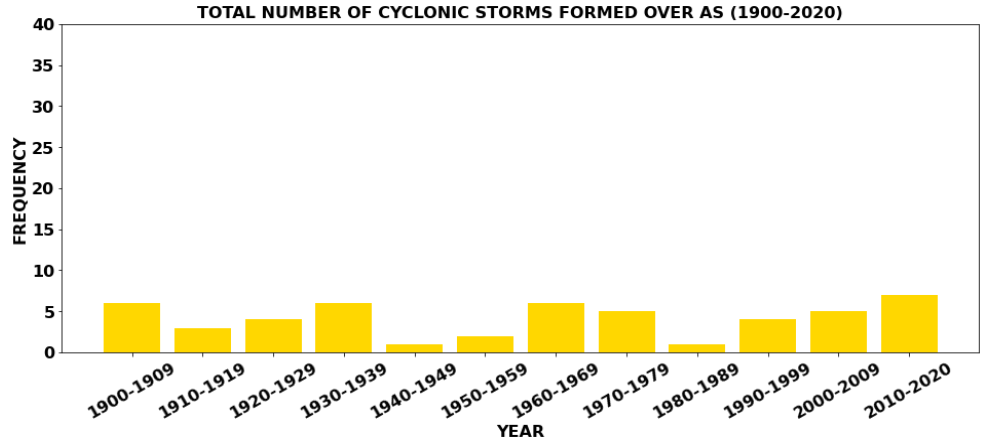

Figure 4.13 (a) Frequency of Cyclonic Storms over Northern Indian Ocean in each 10 year from 1900-2020, (b) Frequency of Cyclonic Storms over Bay of Bengal in each 10 year from 1900-2020, (c) Frequency of Cyclonic Storms over Arabian Sea in each 10 year from 1900-2020.

The frequency of Cyclonic Storms in the NIO every 10 years from 1900-2020 was presented in Figure 4.13 (a). The maximum formation of Cyclonic Storm in the NIO was noticed all along 1900-1939 with the highest number of 39 Cyclonic Storms formed in the course of 1930-1939. During 1940-1999, there was a decrement observed in the appearance of Cyclonic Storms whereas it had an advancement after 2000. In Figure 4.13 (b), the occurrence of Cyclonic Storms every 10 years from 1900-2020 over the BoB was illustrated. In this region, the maximum formation of Cyclonic Storms was observed in the interim of 1920-1929 with about the formation of 34 CS during that period. The frequency of CS was found to be high from 1900-1939. Later 1940, the development of CS had a decrement with the least number of CS formed in the course of 1990-1999. A different pattern of CS frequency was examined over the AS every ten years from 1900-2020 and was depicted in the Figure 4.13 (c). Most of the 10-year period, had the occurrence of about 6 CS, whereas the maximum of 7 CS was identified during 2010-2020. The least emergence of about 1 CS was observed in the course of 1940-1949 and 1980-1989.

4.14 FREQUENCY OF SEVERE CYCLONIC STORMS OVER NORTHERN INDIAN OCEAN

a)

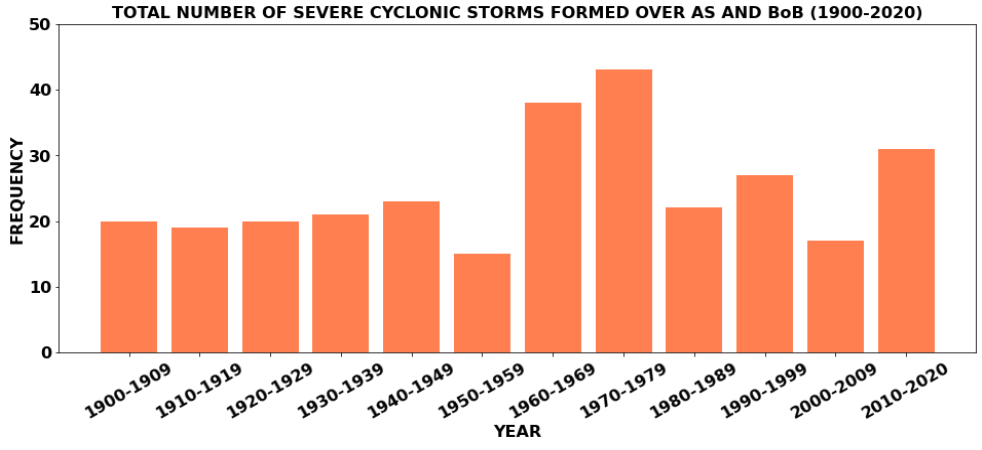

b)

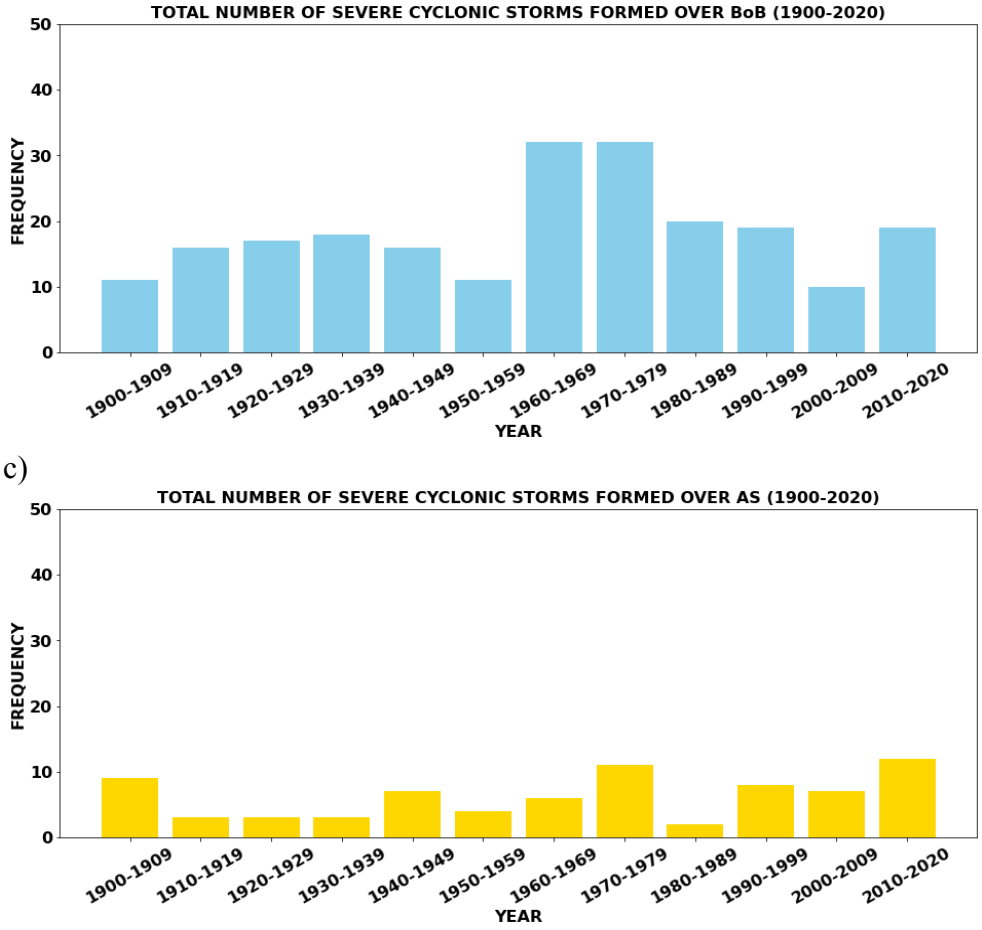

Figure 4.14 (a) Frequency of Severe Cyclonic Storms over Northern Indian Ocean in each 10 year from 1900-2020, (b) Frequency of Severe Cyclonic Storms over Bay of Bengal in each 10 year from 1900-2020, (c) Frequency of Severe Cyclonic Storms over Arabian Sea in each 10 year from 1900-2020.

The frequency of Severe Cyclonic Storms every 10 years from 1900-2020 in the NIO was represented in Figure 4.14 (a). There was an increasing trend observed in the occurrence of SCS over the years. The greatest number of SCS was recorded in the interim of 1970-1979 with the formation of about 43 SCS. Even though the 10-year period after 1979 did not have SCS as that of 1970-1979, an appreciable amount of SCS was identified in the NIO. The minimum occurrence of about 15 SCS over NIO was examined all along 1950-1959. Figure 4.14 (b) displayed the occurrence of SCS in the BoB every ten year from 1900-2020. In BoB, the development of SCS was very less in the time of 1900-1960. Thereafter 1960, there

was an increment in the appearance of SCS over BoB. The occurrence was maximum in the course of 1960-1969 and 1970-1979 with the development of 32 SCS. The formation of SCS after 1979 had a reduction, but a considerable amount of SCS was found in BoB after 1979 which was greater than that during 1900-1960. The least amount of 10 SCS in this region was found between 2000-2009. The occurrence of SCS every ten years from 1900-2020 over the AS was represented in Figure 4.14 (c). Over the AS, there was an enhancement in the appearance of SCS after 1970, whereas it had a decrement throughout 1980-1989. The greatest number of 12 SCS was developed in the interim of 2010-2020, followed by 11 SCS during 1970-1979. The minimum occurrence of 2 SCS was identified during 1980-1989.

4.15 FREQUENCY OF DEPRESSIONS, CYCLONIC STORMS AND SEVERE CYCLONIC STORMS IN NORTHERN INDIAN OCEAN DURING EACH MONTH

a)

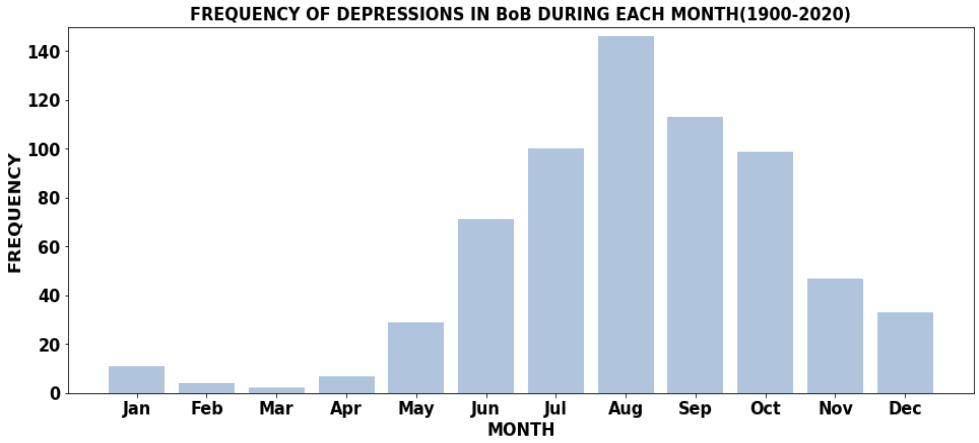

b)

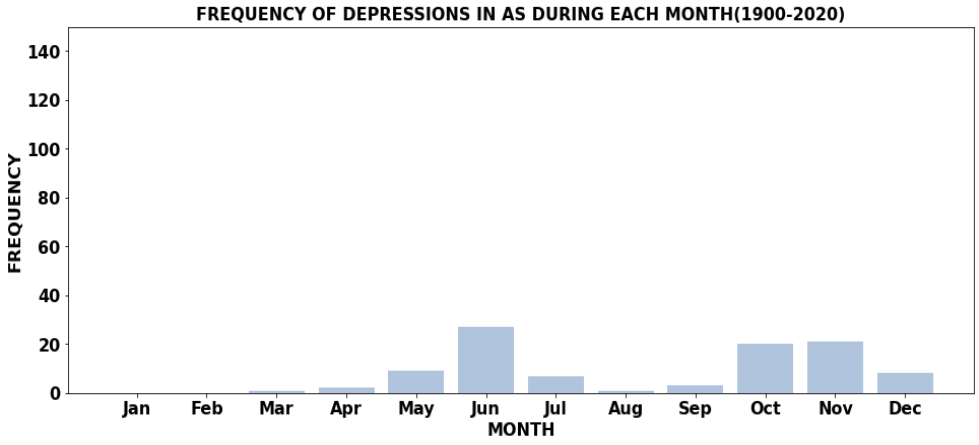

Figure 4.15 (a) Frequency of Depressions formed over Bay of Bengal during each month from 1900-2020, (b) Frequency of Depressions formed in Arabian Sea during each month from 1900-2020.

The Occurrence of Depressions in each month from 1900-2020 over the BoB was illustrated in Figure 4.15 (a). The development of Depressions was maximum in August with the formation of about 140 Depressions during that month from 1900-2020. The least appearance of depressions was identified in the course of March with two depressions from 1900-2020. The appearance of depressions was limited all along January, February, March and April, whereas the occurrence of depressions was considerable during June, July, September and November, but not as great as the formation all along August. Figure 4.15 (b) depicted the formation of depressions during each month from 1900-2020 in the AS. From 1900-2020, in January and February, depressions did not develop in the AS. The maximum occurrence of depressions from 1900-2020 was observed in June. During June, there was the formation of about 27 depressions. A Considerable amount of depressions was identified during October and November, which was less compared to that of depressions during June. In contrast to the greatest appearance of depressions during August in BoB, the formation of depression was very limited during August over the AS. The minimum frequency of depressions over the AS was recorded in the months of March, April, August and September.

c)

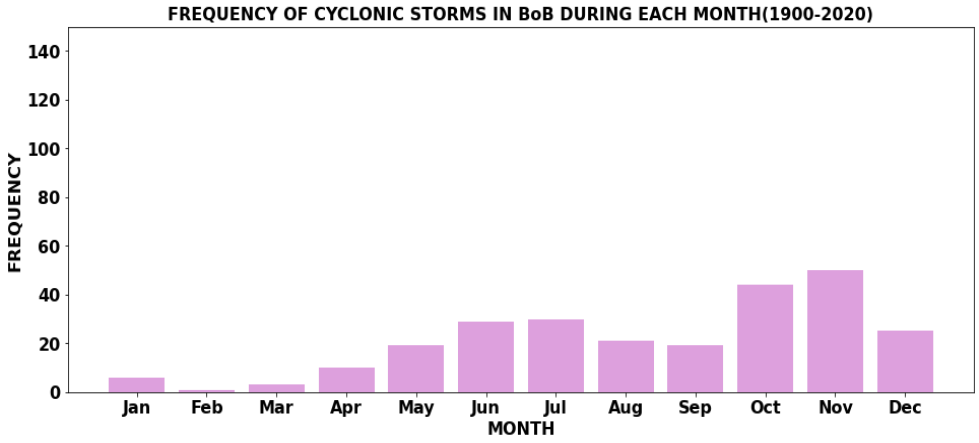

d)

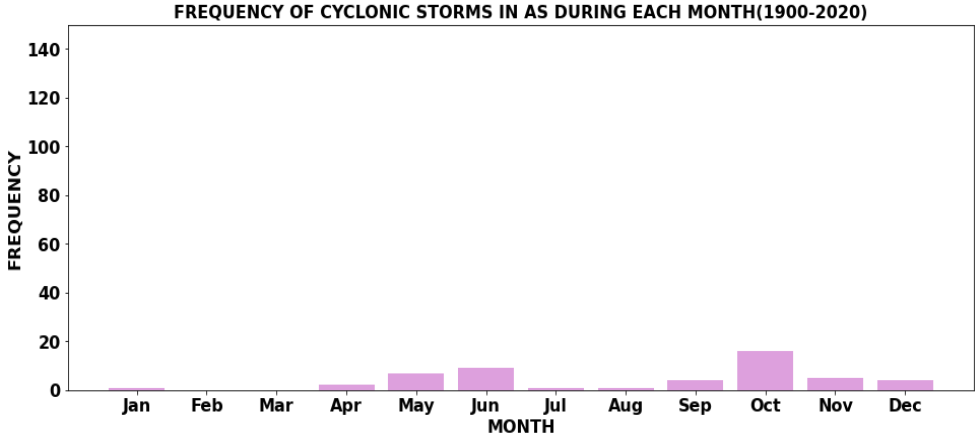

Figure 4.15 (c) Frequency of Cyclonic Storms formed in each month from 1900-2020 over Bay of Bengal, (d) Frequency of Cyclonic Storms formed in each month from 1900-2020 over Arabian Sea

The occurrence of Cyclonic Storms every month from 1900-2020 over the BoB was represented in Figure 4.15 (c). The frequency of CS was maximum during November followed by October. About 50 CS were formed over the BoB in November and 44 in October from 1900-2020. There were only 1 CS formed in the BoB in February in the course of 1900-2020. The formation of CS was very less in January, February, March and April, whereas the frequency during May, June, July, August, September and December was greater than that during January-

April, but not high as in November and October. Figure 4.15 (d) represented the development of CS in the AS during each month from 1900-2020. In comparison to the BoB, the frequency of CS in the AS is very small maximum of 16 CS was developed in the month of October from 1900-2020. Over the AS, CS was not formed throughout 1900-2020, in the month of February and March and only 1 CS was formed during January, July and August. The frequency of CS formed in October was almost double the number of CS formed during the other months.

e)

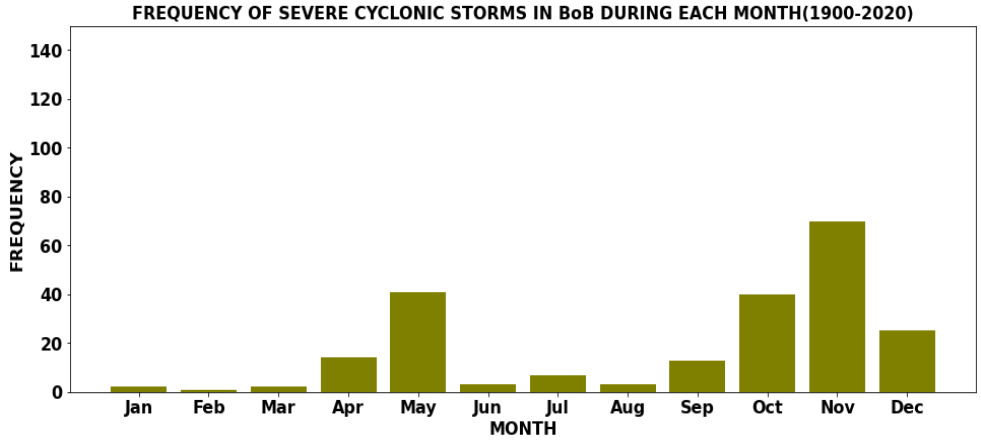

f)

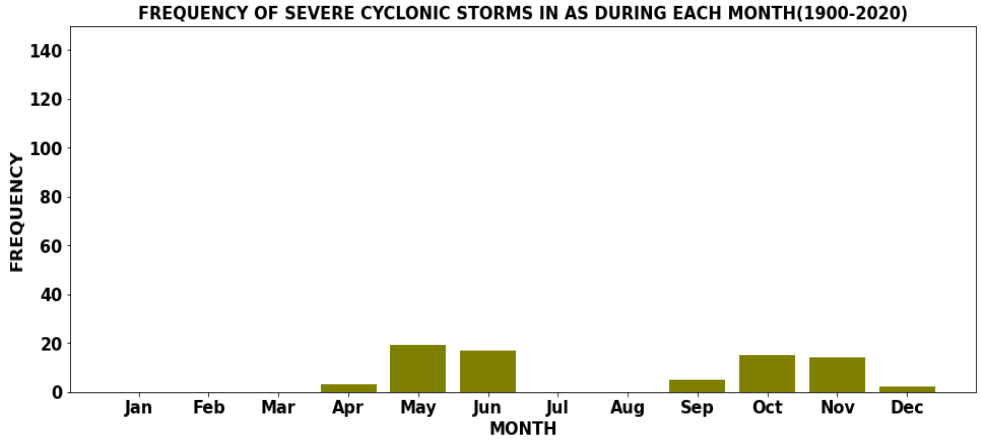

Figure 4.15 (e) Frequency of Severe Cyclonic Storms over Bay of Bengal in each month from 1900-2020, (f) Frequency of Severe Cyclonic Storms over Arabian Sea in each month from 1900-2020

The development of Severe Cyclonic Storms from 1900-2020 during every month over the BoB was laid out in Figure 4.15 (e). An appreciable number of SCS was observed over the BoB during May, October and November with a maximum of 70 SCS during November. The appearance of SCS was very less during January, February, March, June and August with the lowest of only 1 SCS during February all along 1900-2020. Figure 4.15 (f) presented the frequency of SCS during each month from 1900-2020 over the AS. At the time of January, February, March, July and August, there were no SCS formed over the AS. The maximum formation of SCS was in the course of May with 19 SCS. The occurrence of SCS was comparatively high along with May, during June, October and November.

4.16 FREQUENCY OF DEPRESSIONS, CYCLONIC STORMS AND SEVERE CYCLONIC STORMS FORMED OVER NORTHERN INDIAN OCEAN DURING EL NINO AND LA NINA YEARS

a)

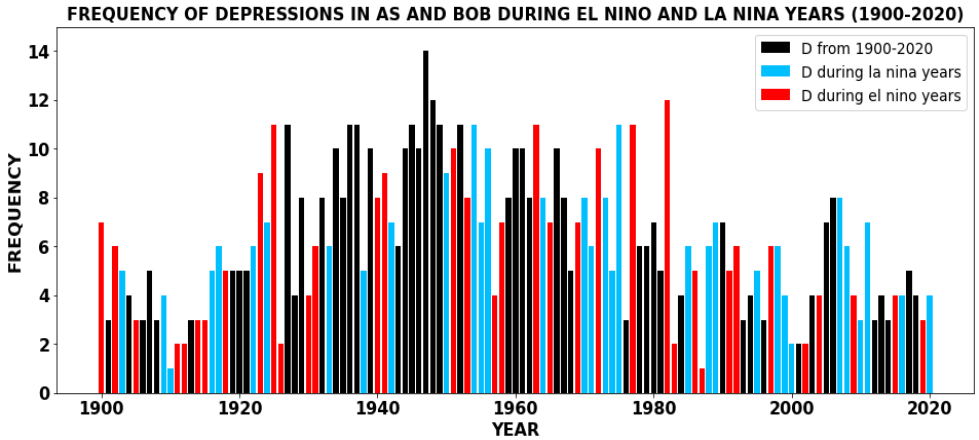

Figure 4.16 (a) Frequency of Depressions formed over Northern Indian Ocean from 1900-2020 during El Nino and La Nina years.

The warm phase of ENSO characterised by warming of the sea surface in the Tropical Pacific Ocean is labelled as El Nino. The occurrence of the depressions

in the NIO from 1900-2020 was displayed in the Figure 4.16 (a). The black coloured bar represented the frequency of depressions from 1900-2020 whereas the red and blue coloured bar exhibited the frequency of depressions at the time of El Nino and La Nina respectively. The maximum occurrence of 14 depressions was identified in NIO during 1947, whereas at the time of El Nino, a maximum of 12 depressions was observed in the course of 1982. La Nina is the cold phase of ENSO characterised by lower than the normal SST over the Tropical Pacific Ocean. The greatest number of 11 depressions had developed at the time of La Nina during 1954 and 1975. In comparison to the La Nina years, the frequency of depressions was greater all along the El Nino years. Later 1980, there was a decrement in the frequency of depressions in the course of El Nino, whereas an increment was observed in depressions formed during La Nina.

b)

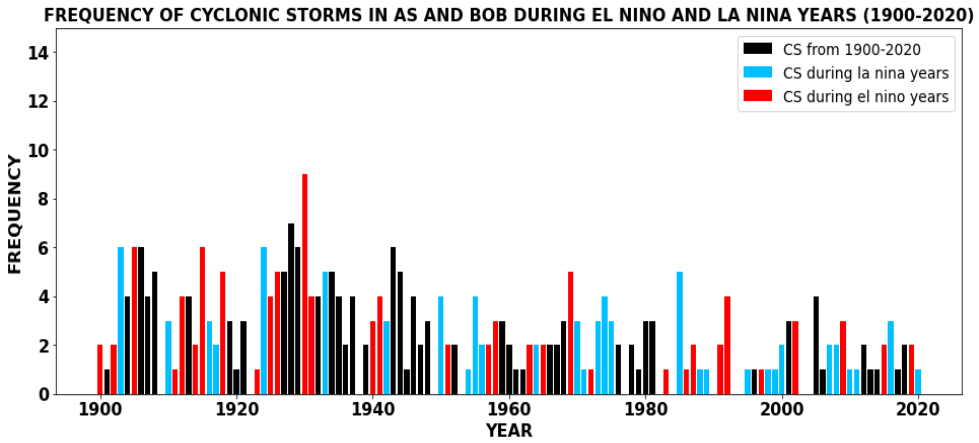

Figure 4.16 (b) Frequency of Cyclonic Storms over Northern Indian Ocean from 1900-2020 during El Nino and La Nina

Over the NIO, the frequency of Cyclonic Storms from 1900-2020 all along El Nino was laid out in Figure 4.16 (b) portray the Cyclonic Storms formed over the NIO during La Nina years. The bar coloured in black depicted the Cyclonic Storms over NIO from 1900-2020, whereas the red and blue coloured bar was the appearance of CS over NIO at the time of El Nino and La Nina respectively. The highest number of 9 CS over NIO was formed in the time of 1930, which was an El

Nino year. The greatest number of CS formed during La Nina was six in the course of 1903 and 1924. The frequency of CS during La Nina was not as high as that during El Nino. The appearance of CS from 1900-1940 was the maximum in the interim of El Nino, whereas in the time of La Nina, only a few CS appeared in NIO. Later 1960, the frequency of CS was greater during La Nina where it had diminished at the time of El Nino.

c)

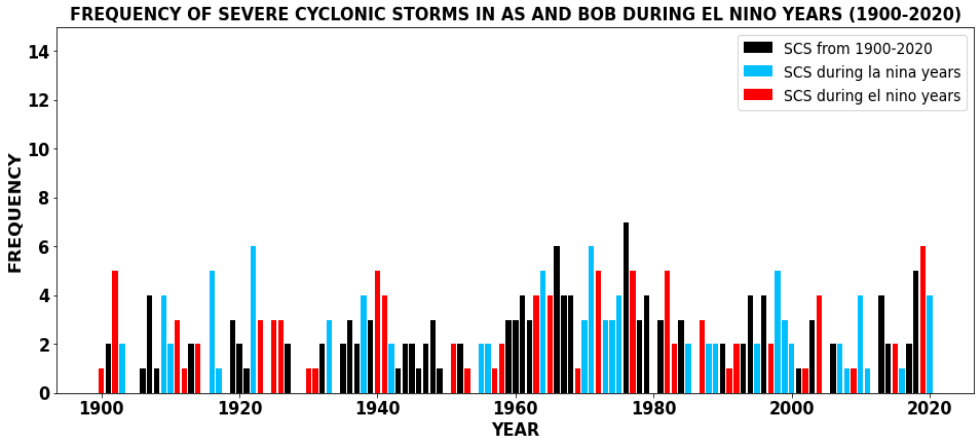

Figure 4.16 (c) Frequency of Severe Cyclonic Storms over Northern Indian Ocean during El Nino and La Nina years from 1900-2020

The Severe Cyclonic Storms over NIO from 1900-2020 during the El Nino year was illustrated in Figure 4.16 (c) represented the occurrence of SCS at the time of La Nina over NIO from 1900-2020. The black coloured bar depicted the SCS formed over NIO from 1900-2020 and the red and blue coloured bar was the SCS formed in the course of El Nino and La Nina respectively. The frequency of SCS was less in El Nino year, in comparison to that of SCS in La Nina year. Over NIO, the maximum number of 7 SCS was developed in 1976. During El Nino, the frequency was highest during 2019 with 6 SCS and during La Nina, the frequency was maximum all along 1922 and 1971 with 6 SCS. The SCS formation in NIO

during El Nino was found to reduce after 1960, whereas the SCS in the course of La Nina exhibited an advancement after 1960.

4.17 FREQUENCY OF DEPRESSIONS, CYCLONIC STORMS AND SEVERE CYCLONIC STORMS FORMED OVER NORTHERN INDIAN OCEAN DURING IOD YEARS

a)

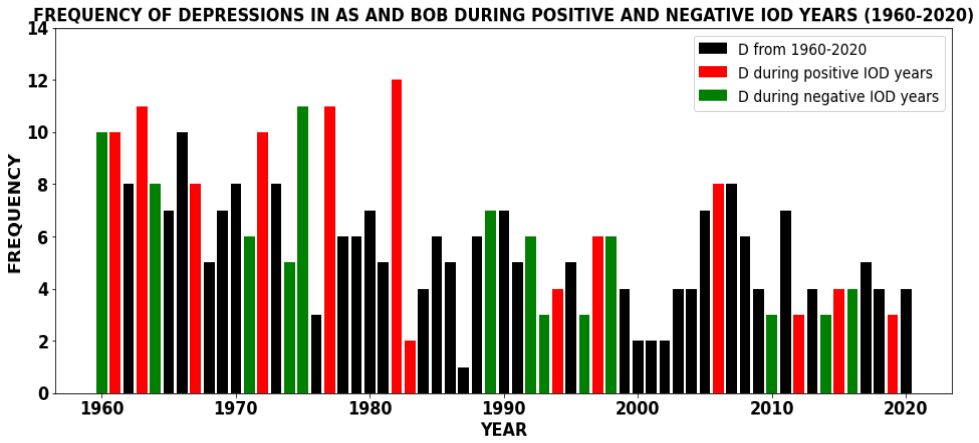

Figure 4.17 (a) Frequency of Depressions formed over Northern Indian Ocean during Positive and Negative IOD years from 1960-2020

Positive IOD is characterised by greater than average SST over the Western part of the Indian Ocean and Negative IOD is characterised by warmer SST over the Eastern Indian Ocean. The depressions formed over NIO from 1960-2020 during Positive IOD was illustrated in Figure 4.17 (a) represented the frequency of depressions formed over NIO during Positive and Negative IOD from 1960-2020. The black coloured bar depicted the depressions formed over NIO from 1960-2020 and the red and green coloured bar represented the depressions that appeared at the time of Positive and Negative IOD respectively. In the NIO, the maximum number of depressions was formed during the Positive IOD year 1982 with 12 depressions which were also recognised as an El Nino year. At the time of Negative IOD, the maximum of 11 depressions was formed during 1975 which was also a La Nina

Year. Later 1960, most of the Positive IOD year coincided with El Nino and Negative IOD with La Nina and it was observed that the years with the coincidence of IOD and ENSO events exhibited an enhancement in the frequency of depressions formed over the NIO.

b)

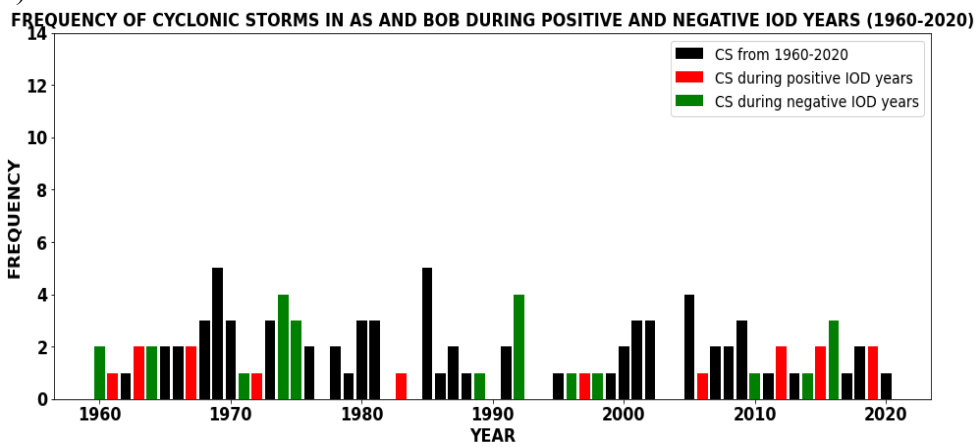

Figure 4.17 (b) Frequency of Cyclonic Storms over Northern Indian Ocean during Positive IOD years from 1960-2020

The occurrence of Cyclonic Storms over NIO in the course of Positive and Negative IOD from 1960-2020 was illustrated in Figure 4.17(b). The black coloured bar represented the formation of CS in NIO from 1960-2020 and the red and green coloured bar depicted the occurrence of CS at the time of positive and negative IOD years respectively. The number of CS each year at the time of positive IOD was less when compared to that of negative IOD years. At the time of negative IOD accompanied with La Nina, the number of CS was relatively high with about 4 CS during 1974 and 1992. The maximum occurrence of CS during positive IOD years was two.

c)

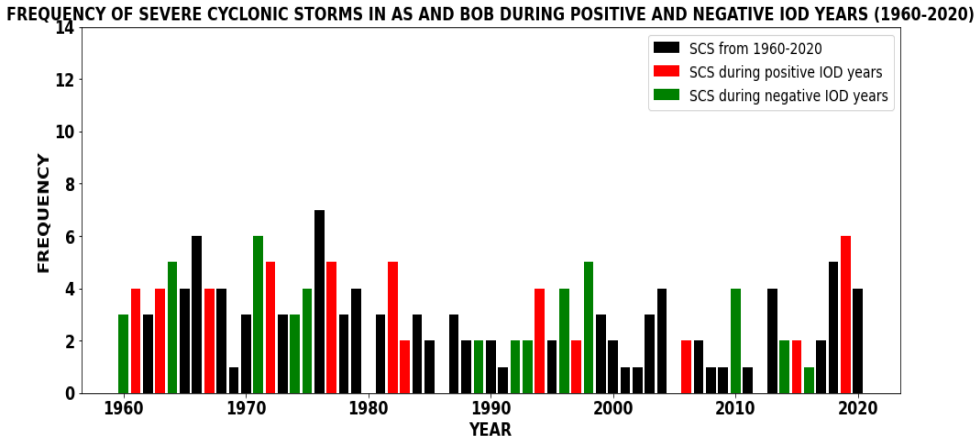

Figure 4.17 (c) Frequency of Severe Cyclonic Storms over Northern Indian Ocean from 1960-2020 during Positive and Negative IOD years

The frequency of Severe Cyclonic Storms over NIO from 1960-2020 during the Positive and Negative IOD year was illustrated in Figure 4.17 (c). The maximum number of SCS formed over NIO was 7 in 1976. The maximum number of SCS formed in NIO during Positive IOD was 6 in 2019 and that during Negative IOD was 6 in 1971. The occurrence of SCS later 1990 was highest during Negative IOD years than Positive IOD years.

4.18 DISTRIBUTION OF THE SURFACE CHLOROPHYLL

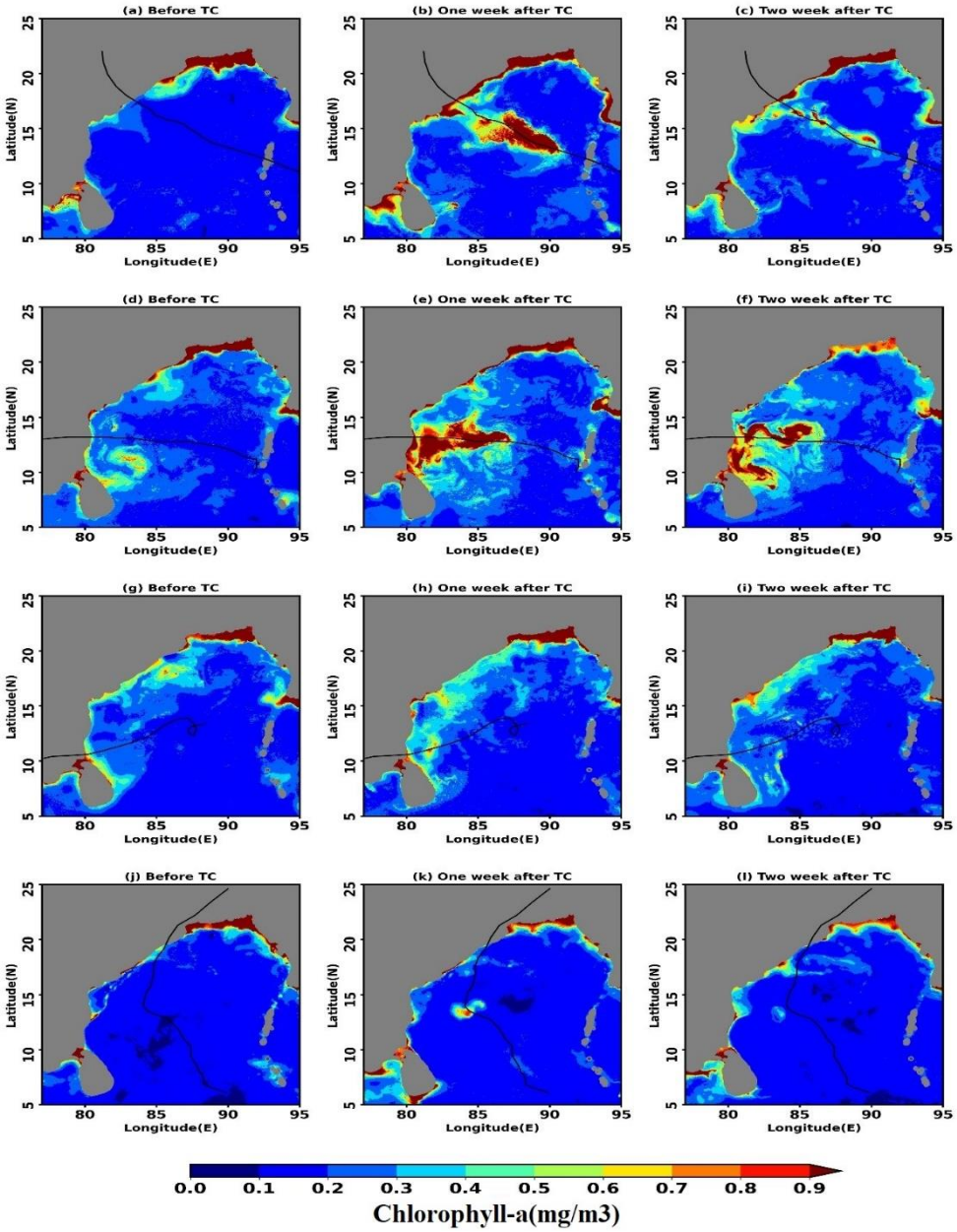

Figure 4.18 Chlorophyll concentration (mg/m3) 8 days average for one week before, one week after and two after the cyclones: (a-c) Hudhud, (d-f) Vardah, (g-i) Gaja and (j-k) Fani, respectively. Tracks of the cyclones were overlaid on each plot**.**

For this study, the region where the cyclone attains its maximum wind speed is considered as the impact zone for each cyclone. Figure 4.18(a-c) displayed the

intensity of chlorophyll-a concentration induced by the cyclone Hudhud before one week, after one week and after two weeks. Before the occurrence of the cyclone (September 27-October 03, 2014) the entire study area and the impact zone generally exhibited a lower value of chlorophyll-a (≈0.2mg/m^3). The impact zone region showed a drastic increase of chlorophyll-a concentration (>3 mg/m^3) one week after cyclone (October 16–23, 2014) and also a well-defined chlorophyll bloom all along the track of Hudhud was developed. During the end of October (October 24–31, 2014), chlorophyll-a was restored to the pre-existing values. Figure 4.18(d-f) represented the influence of cyclone Vardah on the chlorophyll-a concentration before one week, after one week and after two weeks of the cyclone. The figure presented that the Chlorophyll-a was significantly less before the cyclone development (27 November -December 05, 2016). Over this period, chlorophyll-a in the open ocean was < 0.2 mg/m^3 with slightly higher values along the coastal regions. One week after the cyclone (December 15–21, 2016), signatures of a strong chlorophyll bloom appeared. The chlorophyll-a increased significantly, reaching up to 2.8 mg/m^3 during this period. In the following week (December 22–29, 2014), a well-defined chlorophyll bloom all along the track of Vardah was identified. After two weeks of the cyclone, the chlorophyll-a existed and was <2.6 mg/m^3 in the impact zones and the coastal regions. Figure 4.18(g-i) illustrated the action of cyclone Gaja on the chlorophyll-a concentration before one week, after one week and after two weeks of the cyclone. Before the occurrence of Cyclone Gaja, the impact zone exhibited a lower value of chlorophyll-a (< 0.2 mg/m^3). Still, over the northern BoB region, slightly higher values were identified compared to the impact zone. There was no considerable increase of the Chlorophyll-a observed one week after the passage of the cyclone(≈0.8mg/m^3) and identified a peak in the coastal region. Figure 4.18(j-l) revealed the impact of the tropical cyclone Fani on the Chlorophyll-a concentration. During the pre-cyclonic period, the Chlorophyll-a indicated lower values in the entire study region (< 0.2 mg/m^3). In the post-cyclone week, a higher value in the centre of the cyclone track (≈0.9mg/m^3) was identified between 13^0N and 15^0N. The observed patch of the chlorophyll disappeared after two weeks.

4.19 DISTRIBUTION OF WIND AND EKMAN PUMPING VELOCITY

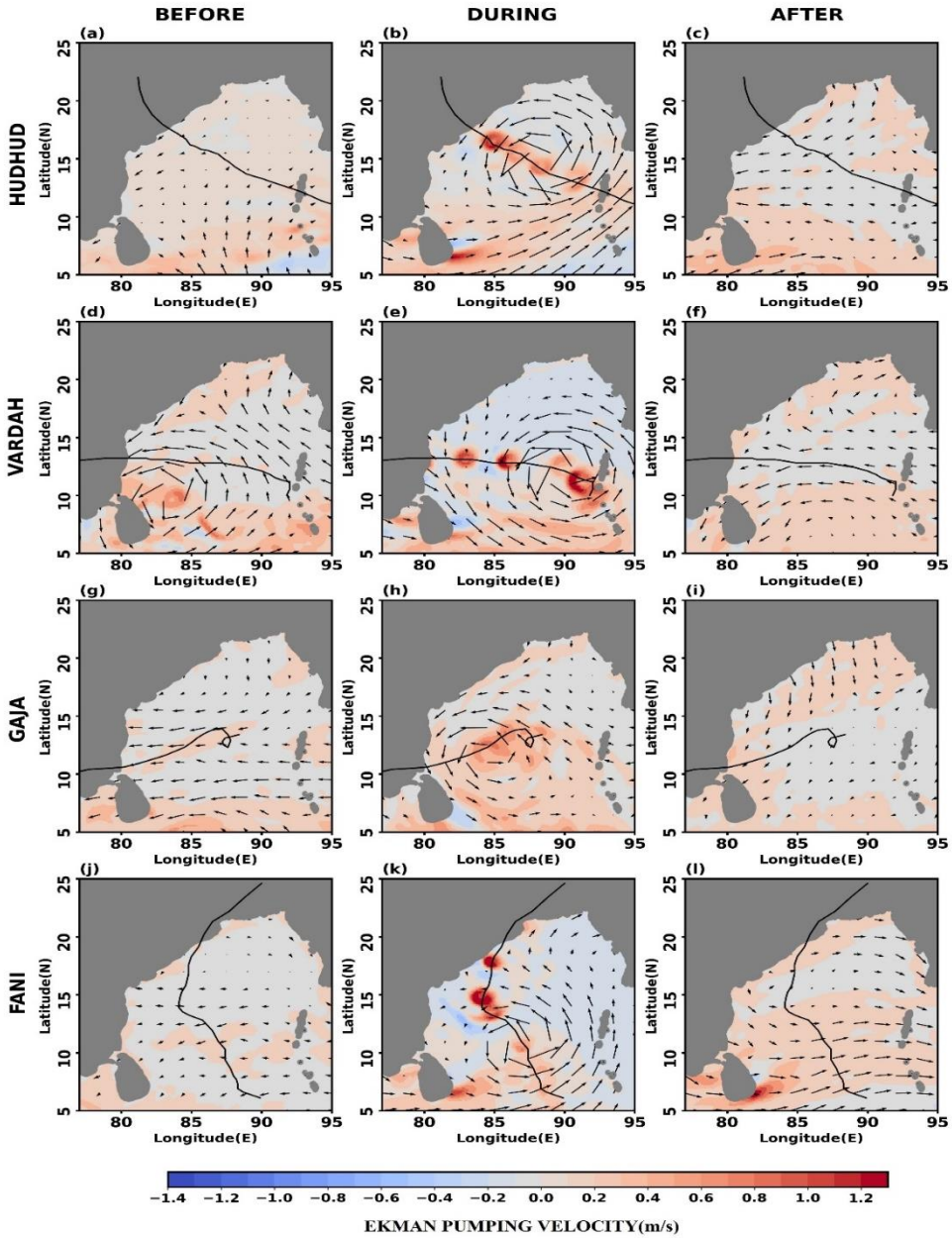

Figure 4.19. Ekman pumping velocity (EPVx10^{-9}) 8 days average for one week before the cyclone, during the cyclone and one week after the cyclones: (a-c) Hudhud, (d-f) Vardah, (g-i) Gaja and (j-k) Fani respectively. Tracks of the cyclones were overlaid on each plot.

Figure 4.19(a) represented the situation one week before the cyclone that exhibited the lower values with weaker upwelling and the windspeed <2m/s all over the study area. The condition during the cyclone was displayed in Figure 4.19(b), where a strong positive upwelling was examined along the cyclone track with a maximum value of Ekman pumping velocity (EPV) >2.5 m/s in the centre part of the impact zone, whereas the Southern BoB presented a strong downwelling near to the coast of Sri Lankan (≈-1.5 m/s). In Figure 4.19 (c), over the study area, the left and right sides of the cyclone track one week after the cyclone showed the weaker upwelling. The path exhibited lower negative values, and the winds appeared similar to the pre-cyclone condition with a wind speed of <2m/s. Figure 4.19(d-f) presented the EPV before, during and after the cyclone Vardah. Before the appearance of the cyclone, the region of the study exhibited moderate windspeed in the South-east direction, which indicated a weaker upwelling. During the cyclonic condition, the study region displayed a positive upwelling (>2 m/s), but the north of the study area showed a negative value and the wind speed was found to be greater than 10 m/s. In the case of post-cyclone, the entire cyclone track displayed a lower negative EPV and the right and left of the track had positive EPV with weak winds. Figure 4.19 (g-i) represented the EPV of the cyclone Gaja before, during and after the cyclone. The entire study region displayed a weaker easterly wind that implies lower positive EPV. During the time of cyclone, the impact zone of the cyclone experienced a moderate windspeed (<10 m/s) that resulted in a weaker positive EPV. After the cyclone, the condition was the same as the situation a week after cyclone Hudhud and Vardah, i.e., the track exhibited a negative EPV and the right and the left sides showed positive EPVs. Figure 4.19 (j-l) illustrated the EPV of cyclone Fani before, during and after the cyclone. The weaker wind reveals that the study area experienced neutral EPV, but at the time of the cyclone, the cyclone's track presented strong upwelling with values < 2m/s. The period after the cyclone, it demonstrated positive EPV with weaker winds.

4.20 NITRACLINE AND EUPHOTIC ZONE DEPTH OVER THE IMPACT ZONE

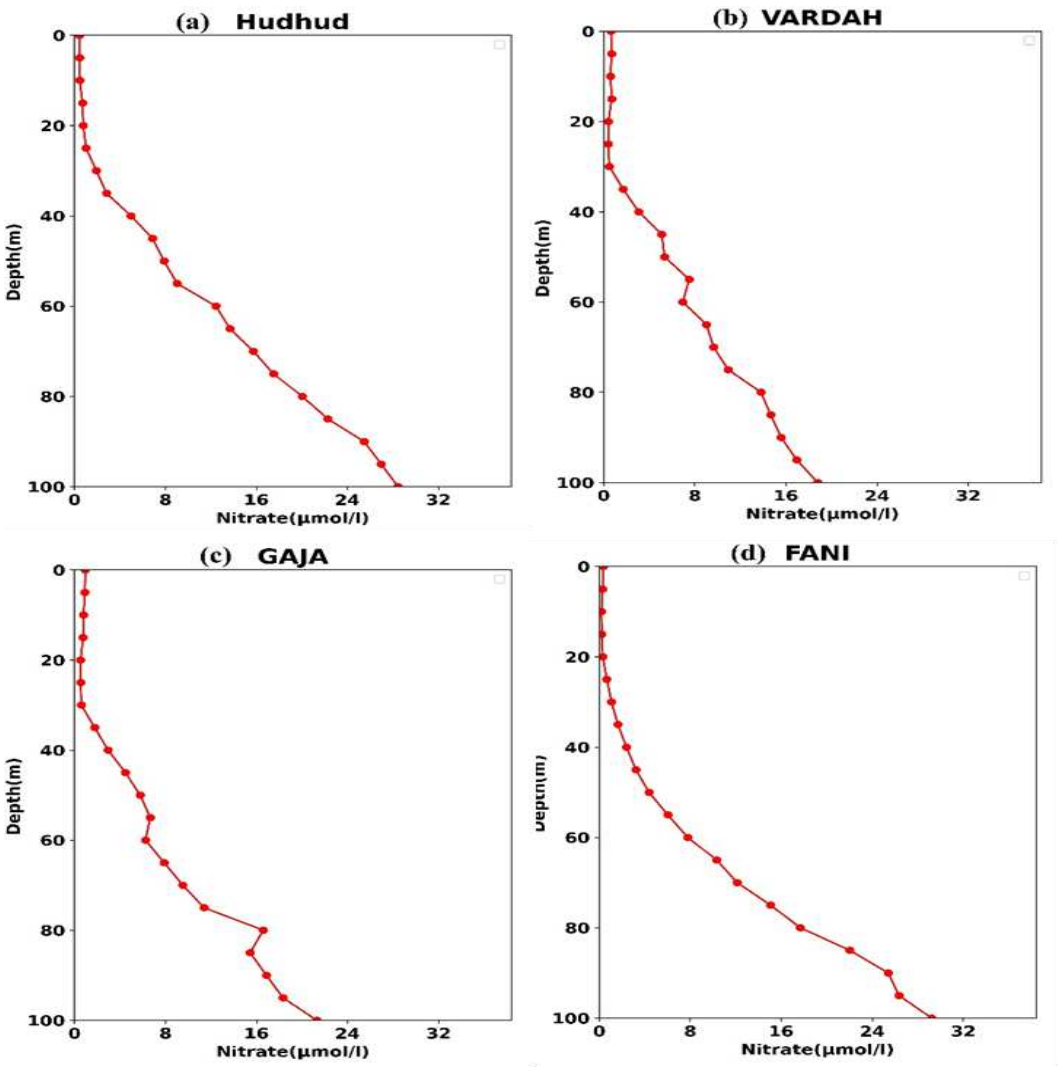

Figure 4.20 Vertical profiles of climatological nitrate concentration (μmol/l) averaged over the impact zone for (a) Hudhud, (b) Vardah, (c) Gaja, (d)Fani in the upper 100 m depth

According to Cermano *et al*., 2008, productivity is negatively correlated with the depth of the nitracline. It can be noted that when the nitracline is shallower, the chlorophyll-a values were higher whereas in the deep nitracline regions, the

chlorophyll-a is relatively lower. The nitracline depth is a significant parameter that controls the chlorophyll-a amplitude. This depth was extracted from the climatological nitrate profile corresponding to each cyclone's respective month of occurrence averaged over their impact zone. The vertical nitrate profiles of each cyclone averaged over their respective impact zones are displayed in Figure (4.20 a-d). From the figures, it was evident that the nitracline depth was 15m,25m,30m and 30m respective to the cyclones. The mean nitracline depth calculated for each cyclone was almost shallow (15 to 30 m).

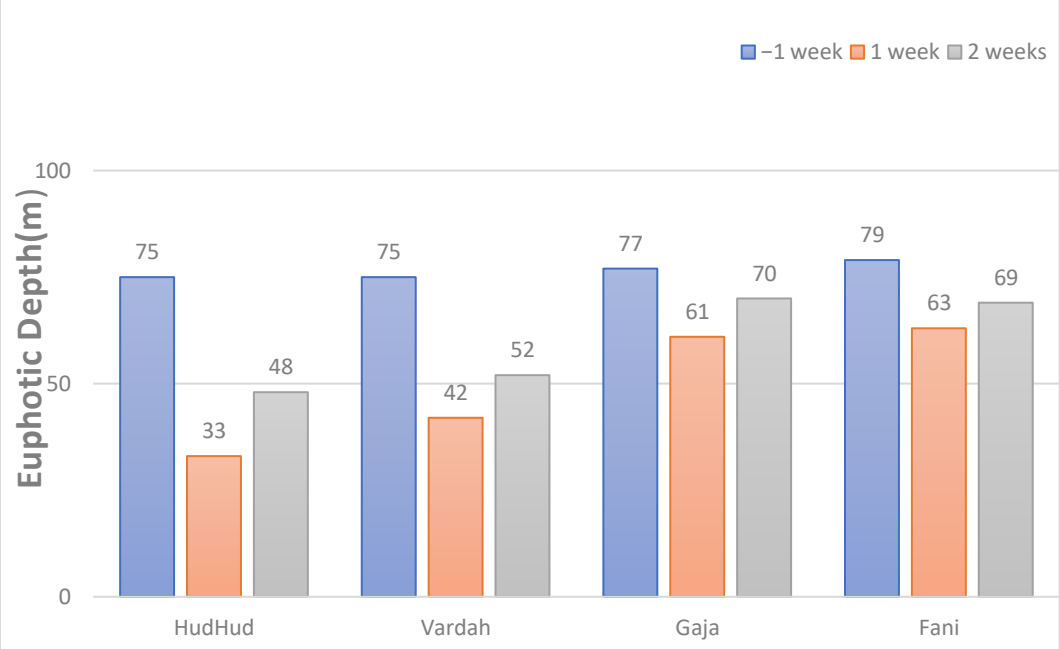

Figure 4.20 (i) Euphotic depth in the impact zone for the cyclones (a) Hudhud, (b) Vardah, (c) Gaja, (d)Fani

One of the parameters which influence the chlorophyll-a amplitude is the Euphotic depth. It was calculated from the surface chlorophyll-a using the equation (2). Figure 4.20 (i) shows that the euphotic depth one week after the cyclone Hudhud and the Vardah exhibited a closer shallow distance between the depth of the euphotic and the climatology monthly. It presented an increase of the

chlorophyll-a concentration after the passage of these cyclones, and also the Cyclone Gaja and the cyclone Fani resulted in very deep euphotic zone depth, whereas it resulted in a lower concentration of the chlorophyll-a after the passage of the cyclones.

4.21 IMPACT ON PRIMARY PRODUCTIVITY

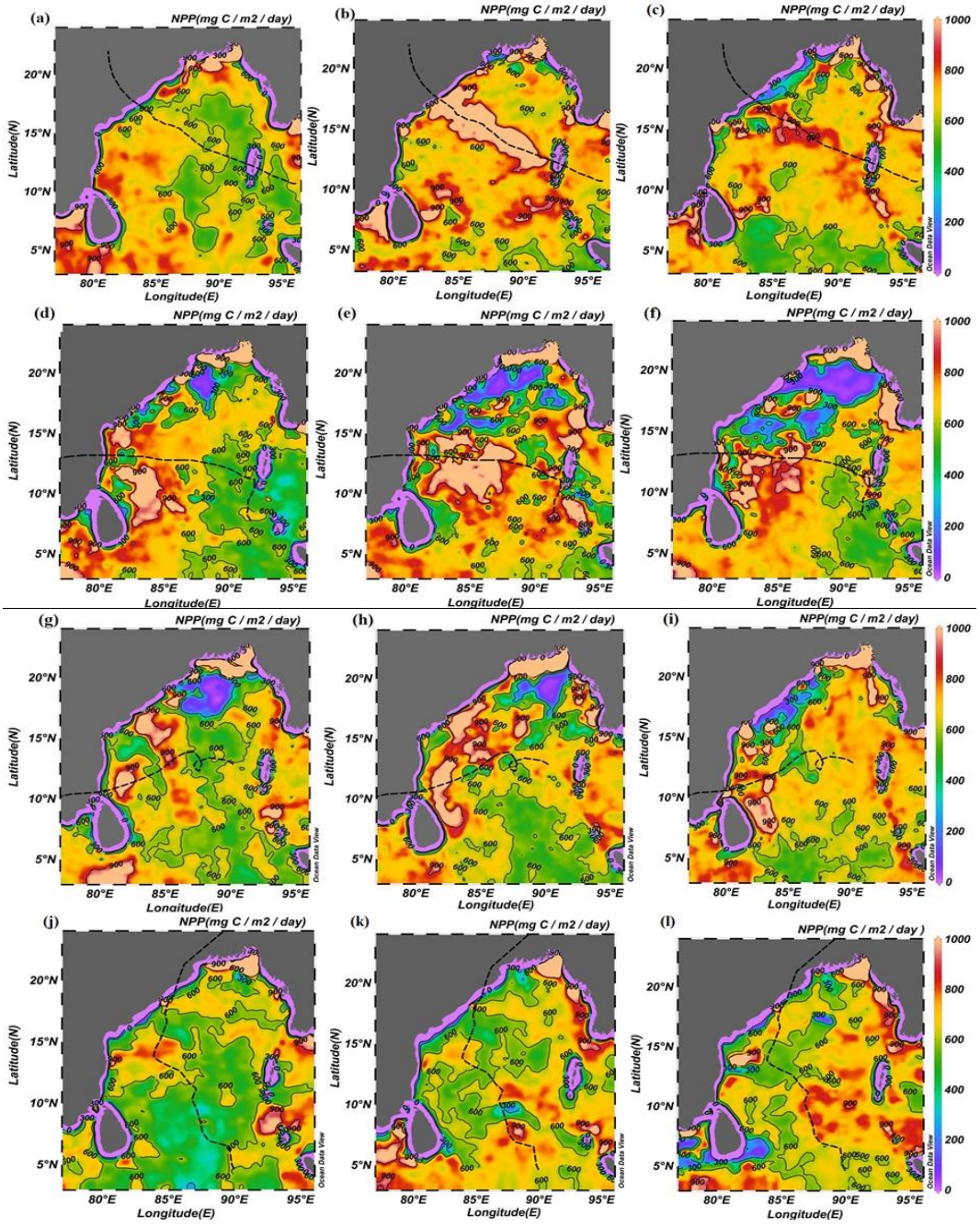

Figure 4.21. Net primary productivity 8 days average for one week before, after one week and two weeks after the cyclones: (fig. a-c) Hudhud, (fig. d-f) Vardah, (fig. g-i) Gaja and (fig. j-k) Fani respectively. Tracks of the cyclones were overlaid on each plot.

Figure 4.21(a-c), represented the cyclone Hudhud which exhibited an increasing pattern of the NPP range and existed along with the cyclone's track. The maximum primary productivity occurred in the domain 84E to 90E. The right and left sides of the track also presented the higher values of NPP. There was a linear relationship between the cyclone intensity and Net primary productivity. In the pre cyclone period, the entire BoB displayed a normal condition of the NPP, but after two weeks of the cyclone, a higher NPP also prevailed. The highest range of NPP for the cyclone was 2338 mg C / m2 / day. In Figure 4.21 (d-f), the coastal region for the western BoB presented an increase in the primary production after one week. Small patches of the higher NPP was observed in the central BoB region (<1000 mg C / m2 / day). In the post cyclonic condition, the region within 82E-85E shows higher primary productivity values, and the lower NPP was identified in the top head of the north-eastern BoB region. Figure 4.21(g-i) exhibited that the NPP range gradually increased from pre-cyclone to post-cyclone. One week after the cyclone, the coast of Tamil Nadu showed the highest peak in the NPP. In Figure 4.21(g-i), at the time of pre and the cyclonic condition, the head of the BoB had the lower values of the NPP, but the post cyclonic condition, the higher productivity was observed in this region. At the time of cyclone, the top portion of the cyclone track exhibited higher productivity (<1000 mg C / m2 / day); however, it disappeared in the post cyclonic condition. In Figure 4.21(j-l), the range of the NPP varied from 330-880 mg C / m2 / day. Before the cyclone, entire Central BoB regions displayed a uniformity in the NPP, and it was approximately 600 mg C / m2 / day, whereas, in the Northern BoB and the Southern BoB regions, there were slightly higher values of NPP than that of the central BoB. During the cyclone, the central BoB region exhibited slightly higher values along the track.

CHAPTER 5
DISCUSSION

SST influences the air-sea interactions and regulates the climate worldwide (Ghasemi, 2020). The SST variation over both the AS and the BoB was examined. The study revealed that the SST variation over both these basins was different and all the boxes considered in the study area had various patterns of SST whereas all the boxes had an increasing pattern of SST. This indicated that the local factors, as well as the global phenomena are responsible for the enhancement in the sea surface temperature. According to Jaswal *et al*., 2012, throughout the year, the SST of BoB and the AS was observed to be greater than the surface air temperature, whereas the AS exhibited a contrast at the time of monsoon. The study conducted by Dinesh Kumar et al. in 2016 revealed that starting with 1880, there was a definite rising pattern of SST in both the BoB and the AS with a greater SST over the BoB. In the present study, even though the high temperature was recorded in the BoB, the increase in temperature from 1960 onwards was high in the AS. From 1940-1960, there was a decrement in the SST, which may be due to the cooling exhibited by the presence of aerosols. In the AS, the rapid rise in temperature did not take place equally (D'Mello and Kumar, 2018). In the interim of pre-monsoon season, the presence of weak winds and the clear skies over the AS culminated in greater insolation which lead to large heat gain and less heat loss through latent heat. With the commencement of the monsoon, the mixing and upwelling generate cooling of the AS. A strong south-north gradient was exhibited by both the AS and the BoB. The difference in SST amid the Northern and Southern BoB and AS and the higher SST over the region closer to the equator was attributed to the thermal ridge, which moves along the equator, which demonstrates the impact of Pacific waters over that region. One of the reasons for the elevated SST over the Southern AS was the presence of a warm pool from the Kerala Coast along the thermal ridge that covers the southwest portion of the Indian peninsula. The SST of the AS is heavily season dependent, whereas the BoB SST remains almost constant throughout (Jaswal *et al*, 2012). The seasonal variation in temperature was observed to be the maximum in

the northern region. The enhanced SST over the regions close to the equator may be attributed to the diminished influence of trade winds over this region. Despite the thermal inertia and the emissions and increased concentration of CO_2, until 1995 the natural decadal pattern in SST was sustained by the cause of Upwelling, however, late 1995, the cooling by upwelling was incapable to counteract the warming of SST induced by the CO_2 (Kumar, 2009). The sustained temperature elevation in this region was by virtue of the drop in the LHF emitted into the atmosphere (D'Mello and Kumar, 2018). The fluctuations in LHF was more connected to the variations in the wind. The Northern AS and BoB displayed greater LHF variation, which was similar to that of the SST variations. Regions with greater windspeed exhibit an enhancement in the LHF (Jones et al., 1995). There was also a decline in windspeed over certain regions that culminated in reduced evaporation and as a response, there occurred rapid heating. In addition, the SST rise was also examined by virtue of enhancement in the Specific Humidity, which generated a decline in the discharge of LHF, that in turn curtail the release of NHF, leading to an ascent in the SST (D'Mello and Kumar, 2018). The SHF is exacerbated by strong winds and considerable variations in the temperature (Cyriac *et al*., 2016). Over the AS, there was a decrement in the SST with an enhancement in the windspeed whereas, over the BoB, it was altered by cause of stratification (Reddy *et al*., 2018). The AS has an enhancement in the windspeed when compared to the BoB, as a result of the presence of the Findlater jet (Shenoi *et al*., 2002). The quantity, frequency, intensity and type of precipitation varies throughout the year and across the decades (Trenberth, 2011). The variation in Specific Humidity was greater over the Northern AS and BoB, whereas the variation in the southern region was minimum. The enhanced wind speed over the Northern region culminated in the enhanced evaporation that elevated the LHF and Specific Humidity over that region, with the reduction in the SST. The Arabian Sea experiences precipitation that is lower than that of the evaporation and BoB receives greater precipitation that exceeds the evaporation (Shenoi *et al*., 2002). The greater temperature of the oceans is commonly associated with greater precipitation and convection. The air-

sea interaction is another component to be investigated in the fluctuations of precipitation over the Indian Ocean. (Chen *et al*., 2012).

According to the research done by An and Wang, 2000, in the late 1970s, the frequency of the ENSO phase indicated an improvement. At the time of the mature phase of El Nino, the easterly wind anomalies over the Western Pacific and Indonesia are attributed to the Indian Ocean warming (Kug and Kang, 2006). Elevated Ocean temperature and aberrant convection systems often emerge in the Indian Ocean, however not with the similar magnitude and intensity as in the Pacific Ocean. From 1960 onwards, warming was identified over the Indian Ocean in the course of El Nino years (Medha Khole, 2003). Prior to the 1970s, there was basin-wide cooling of the Indian Ocean, whereas after the 1990s, there was the weakening of basin-wide cooling all along the La Nina years and the variation in the cooling was attributed to the climate shift in the mid-1970s (Singh *et al*., 2013). The La Nina results in greater precipitation, stronger winds and the variation in the SSTA was influenced mainly by the La Nina occurrences. The reason for the greater influence of La Nina was not clear and can be later investigated. The warming of the Indian Ocean was preceded by some of the El Nino events and the Indian Ocean cooling by La Nina events where the cooling is only slightly connected to the La Nina occurrences (Kug *et al.,* 2005). The probability of occurrence of El Nino and La Nina presented that the occurrence of strong El Nino events was higher than that of La Nina events. The return period was greater for strong and very strong El Nino and La Nina events, which presented greater reliability with limited risk. The decrease in the SSTA variation over the Northern BoB when compared to the other boxes was by virtue of the enhancement in the Net Heat Flux (Chanda *et al*., 2018). According to various research, the temperature rises over the Indian Ocean crop up several months after El Nino attained its mature phase and also it has characteristics that are season dependent (Ohba and Ueda, 2007). According to Chanda *et al*., 2018, the SSTA over the Indian Ocean was not analogous to that of the ONI Index. In the warming scenario, the precipitation that appears in response to the El Nino may intensify, which complicate the ENSO teleconnections (Yeh *et al*., 2018).

El Nino Southern Oscillation episodes over the Pacific Ocean have been considered as a potential stimulus for the IOD whereas other research indicated that IOD is unrelated to ENSO and is a natural variation in the Indian Ocean (Nagura and Konda, 2007). In the interim of IOD occurrences, the SST anomalies are strongly associated with the surface wind anomalies in the Central Equatorial Indian Ocean (Saji and Yamagata, 2003). According to Abram et al. 2020, the appearance of the IOD events has become more intense and frequent, which was exceptional throughout the pre-industrial times. This further lead to a positive IOD like mean state with enhanced warming and repressed warming over the Western Equatorial Indian Ocean and Eastern Equatorial Indian Ocean respectively. If the current trend persists, the occurrence of Positive IOD events will shortly go beyond the extent of last millennium variability (Abram *et al*., 2020). Later 1970s, most of the Positive IOD events appeared with the El Nino episodes which might be as a result of elevated anticyclonic vorticity over the Western Indian Ocean, that offset the Indian monsoon flow that contribute to lowered surface wind stress and consequently boosting the temperature of Western Indian Ocean as a response of Pacific Warming (Wood *et al*., 2020)

The MJO appears to be stronger when there prevails a warmer SST for the reason that the tropical SST heavily influences the MJO activities (Roxy *et al*., 2019). The present study showed an enhancement in the SST over the years as well as the increase in the number of days of the active phase of MJO. The advancement in the MJO since the 1970s was correlated to the protracted temperature rise in the oceans. Despite the fact of growing SST in the Indo-Pacific, the MJO effects are likely to be even more responsive to the SST of West Pacific presumably due to the comparatively larger SST trend in the interim of November-April. The phase duration of MJO over the Maritime Continent and West Pacific had an enhancement while that of the Indian Ocean was found to diminish. Even though temperature increase is pronounced over the Indian Ocean, they do not have much relation with the phase duration of MJO (Roxy *et al*., 2019). The powerful MJO occurrences can alter the SST by 1–2°C. The greatest convection arises due to an increase in SST

and further the improved convection contributes to the lowering of SST (Maloney and Kiehl, 2002).

The greatest warming is induced by the elevation in human greenhouse gas emissions. The ocean's thermal inertia inhibits the worldwide responses to the forcing (Hansen and Sato, 2004). Enhancing greenhouse gas emissions and climate change are putting tremendous pressure on the oceans. As Ocean receives most of the heat from the atmosphere, they get warmer quickly. Since 1993, the global average ocean temperature has almost doubled. Marine heatwaves have increased in frequency and endure longer by cause of ocean warming and the Marine heatwaves become responsible for the large-scale coral bleaching that culminates in reef deterioration. Sea Level Variations, productivity, stratification, ocean circulation, species translocation, oxygen content has been attributed to the warming of the ocean. In comparison to the preindustrial period, one-third of the human CO_2 emissions are consumed by the oceans and the surface layers have become more acidic (Yadav and Gjerde, 2020). The industrial revolution was commenced by 1750. The concentration of carbon dioxide at the time of 1750 was about 280 ppm, while by 2005, there was a tremendous increase in the carbon dioxide, with a concentration of about 380 ppm. In the interim of 1870-2014, the global SST has elevated by 0.72^{o}C (Genner *et al*., 2017). The greenhouse gas concentration had a tremendous increment from 1950, which can be due to industrialisation. The enhancement in the GHG from 1950 culminated in the increase in the SST over the NIO.

Tropical Cyclones of the NIO is responsible for 7% of Cyclones that form worldwide, with 80% of NIO Cyclones originating over the BoB (Wahiduzzaman *et al*., 2016, Bhardwaj and Singh, 2019). According to research, the incidence of Tropical Cyclones with increased intensity in the NIO is expanding (Bhardwaj and Singh, 2019). NIO experienced the greatest occurrence of Tropical Cyclones in the year 2019 with 8 Tropical Cyclones, where five of them appeared over the AS and in 2018, three out of seven Tropical Cyclones in 2018 arose over the AS (Deshpande *et al*., 2021). The present study displayed that the frequency of

cyclonic disturbances in the BoB had an increasing trend till 1970, but further, there was a reduction. The greater formation of cyclonic disturbances in was observed as a result of the large surface area of warm temperature that persisted all over the BoB. In contrast, there was an increment in the frequency of cyclonic disturbances that appeared over the AS. The number of cyclonic disturbances that developed over the AS was much less than that formed over the BoB. The pattern of depressions and Cyclonic Storms over the BoB was exhibiting a declining trend from 1970 and the pattern in the NIO was similar to that of BoB, for the reason that the majority of the depressions and Cyclonic Storms of NIO were contributed by BoB, although the frequency of Severe Cyclonic Storms of BoB and that of the NIO exhibited an enhancement. This conclusion was identical to the findings of Balaji *et al*., 2018, where they found that in NIO, the frequency of cyclones during every year resembled the occurrence of cyclones over the BoB. Across both BoB and NIO, the decrement is almost comparable (Balaji *et al*., 2018). Over the AS, the frequency of depressions, cyclonic storms as well as severe cyclonic storms was having an increment from 1960. Despite the fact that the overall amount of Cyclonic Disturbances over the BoB exhibited a declining trend, global warming escalated the severity of Tropical Cyclones in this region (Bhaskar Rao *et al*., 2019). As reported by Deo *et al*., 2011, the deadliest Tropical Cyclones have become much more intense with tremendous development over the NIO and North Atlantic Ocean.

It is been discussed that, over the AS, the latest catastrophic Tropical Cyclones occurred primarily by reason of anthropogenic forcing and not the natural climatic factors. Confirming to research, the enhanced emissions of sulphate and anthropogenic black carbon contributed to the severity of cyclones over the AS in the course of April-June, primarily by diminishing the vertical wind shear (Murukami *et al.,* 2017). Recently, cyclogenesis appears to be more frequent over the AS, although its frequency was observed to diminish over the BoB. Improvement in cyclogenesis in NIO correlates to the increment in SST and decrement in vertical wind shear (Deo *et al*., 2011). The occurrence of Tropical Cyclones over NIO is less frequent when in comparison with the Tropical Cyclones

developed over the other basins, however over the last 300 years, eight out of ten catastrophic Tropical Cyclones appeared in the NIO which produced extensive damages and mortality. Amid the warming period induced by global warming, the incidence of Severe Cyclonic Storms over NIO had an increment of about 41%, which clearly indicate that the destructions caused by these storms will be immense by cause of the shallow depth of BoB, low flat coastal terrain and the densely populated coastal areas (Singh *et al*., 2019). The formation of Tropical Cyclones was found to decrease as a result of increment in upper tropospheric temperature by global warming, which weakens the Hadley circulation.

Analogous to the results obtained by Singh *et al*., 2019, this study also displayed that the incidence of depressions over the BoB was the maximum throughout August, with the second-highest appearance of Depressions in the course of September and then October, whereas, over the AS, maximum depressions developed during June and was followed by November and October. Similarly, the occurrence of Cyclonic Storms was found to be maximum during November and then during October and the SCS was identified to be the highest in the interim of November, followed by May and then October. Over the AS, the CS occurrence was high throughout October and the SCS was the highest in the course of May. The intensity of tropical cyclones is expanding as a result of the long climate feedback mechanism which occurs by reason of the increase in the temperature. The rise in temperature enhances the moisture that entraps the longwave radiation that further strengthens the boost in temperature which eventually contribute to an increment in the severity of Tropical Cyclones (Singh *et al*., 2019). The moderate wind shear at the time of peak Summer monsoon will limit the intensification of depressions and deep depressions over the AS. The frequency of cyclonic disturbances over the AS at the time of August was limited by virtue of the cooling of SST after the monsoon withdrawal, whereas the BoB temperature remained high which supported the formation of cyclonic disturbances (Jaswal *et al*., 2012).

The large-scale parameters that contribute to an environment that encourage the formation and intensification of cyclones are influenced by ENSO, where the conditions for tropical cyclones are suitable at the time of La Nina (Eric and Chan, 2012). The conditions are beneficial at the course of La Nina, because of abnormally high relative humidity, increased relative vorticity and low wind shear (Singh and Roxy, 2020). Confirming to research, in the interim of El Nino, the incidence of Tropical Cyclones was observed to be lesser over BoB throughout May and November which was perceived as severe cyclone months and also the occurrence of the cyclones was observed to be greater in the time of La Nina and was lesser in the course of El Nino. According to the analyses, the development of intense cyclones was recorded at the time of La Nina and Positive IOD years (Mahala *et al*., 2015). Over the BoB, the low-level vorticity and the Tropical Cyclone Heat Potential that are conducive for the formation of Tropical Cyclone, during El Nino was not as high as that at the time of La Nina (Sattar and Cheung, 2019). During Positive IOD events over the Indian Ocean, the warmers SST prevails over the Western Tropical Indian Ocean, which diminish the convection and generates low level anticyclonic atmospheric circulation which is disadvantageous for the development of Tropical Cyclones and the situation overturns at the time of negative IOD (Yuan and Cao, 2013). The impact of ENSO and IOD on the cyclones of the Arabian Sea is not widely discussed. In the present study, over the NIO, the frequency of Cyclones was found to be the maximum in the course of La Nina. Considering the IOD events, the occurrence of Tropical Cyclones was the highest at the time when the negative IOD events cooccurred with La Nina (Mahala *et al*., 2015).

Four different cyclones (Hudhud, Vardah, Gaja and Fani) with higher wind speed and those cateogrised under the very severe cyclones and the extremely severe cyclones were analysed. They all travelled more than six days before the landfall. Except for Cyclone Fani other three were formed in the post-monsoon season and also they affected the Andaman region and also the Indian Penisula. The cyclone Fani formed in the premonsoon season and it was formed over the central BoB region and also had its effect on the Indian Penisula. The cyclone-

induced surface Chl-a increasing can result from the uplift of the higher Chl-a water at the deeper layer to the surface and the upwards nutrients supplying for the growth of the phytoplankton. It has been documented that only half of the Cyclones generated the Chlorophyll-a blooms and contributed to the marine primary productivity (Pan *et al*., 2017; Lin *et al*., 2012). One of the critical indicators to evaluate ocean biogeochemistry is the concentration of Chlorophyll-a within the upper water column (Jayaram *et al*., 2021). The entrainment of nutrients from the deeper layers is primarily accounted for the impact of Tropical Cyclones on the chlorophyll content. The advancement in primary production is associated with the rise in chlorophyll and accessibility of irradiance (Rao *et al*., 2006). The increased concentration of Chlorophyll-a might persist from a few days to a month. Confirming to studies, the Tropical cyclone intensity, translation speed, forcing period as well as the pre-oceanic variables including Mixed layer depth, Eddy and stratification have a part in the generation of the Chlorophyll blooms (Yu *et al*., 2018). The Ekman Pumping Velocity (EPV) is the metric that is used to assess the process of upwelling. Upwelling is represented by positive EPV, while downwelling is denoted by negative EPV (Vidya and Das, 2017).

The nitracline depth is defined as the depth where the nitrate concentrations begin to increase from near-zero levels. As most of the Tropical Cyclone affected regions are nitrogen-limited, the nitracline depth is a natural indicator used for evaluation of nitrate concentration and is analogous to the thermocline where the SST responses are investigated (Menkes *et al*., 2016). The cyclone induced production of phytoplankton is regulated by the mixed layer depth and the fluctuations in the nitracline (Vidya and Das, 2017). The depth of the euphotic zone (Ze) is defined as the depth at which the photon flux equals 1% of the flux measured just above the air–sea interface. In accordance with research, there has been an expansion of phytoplankton by virtue of nutrient supply in the euphotic zone. The euphotic zone nutrient availability is a result of mixing and upwelling in subsurface layers and the lower part of the mixed layer (Seelanki *et al*., 2021). Owing to enhanced nutrient input, the phytoplankton biomass increase has been identified to be associated with the super cyclones. After and at the time of the cyclone, light is

one of the fundamental components influencing the primary production in the ocean (Sarma *et al*., 2019).

CHAPTER 6

SUMMARY AND CONCLUSION

Tropical Cyclones are considered to be one of the catastrophic and life-threatening events, as it is accompanied by the heavy winds, torrential rainfall and storm surges. India is one of the most vulnerable countries to weather-related extreme events like a cyclone, which is considered to be one of the natural disasters that cause enormous damages and destructions over NIO rim countries. The study analysed the long-term trends in the NIO Tropical Cyclones from 1900-2020. On average, the NIO that includes the BoB and the AS accounts for 7% of global Tropical Cyclones. The SST is one of the important parameters essential for the formation of Tropical Cyclones. The SST over the NIO was exhibiting an increase over the years. The BoB had the highest recorded SST, whereas the AS displayed the highest increase in the SST over the years from 1960. The analyses presented that the SST rise throughout the NIO was not uniform. It displayed variations within a small range and thus the SST warming cannot be attributed to the global factors alone, however, the local phenomena also play a major role in the fluctuations in the NIO sea surface temperature. The SST over certain region exhibited a reduction in the interim of 1940-1970. This cooling was attributed to the elevation in aerosol concentration. Certain research believed that the cooling appears as a result of the increase in aerosol concentration that diminishes the amount of sunlight entering the earth surface. The variations in the Latent Heat Flux was attributed to the fluctuations in the wind speed. The Latent Heat Flux had a decrement as the wind speed declined. There were considerable fluctuations in the precipitation and wind speed over the years throughout the NIO. The increase in the wind speed results in an increase in the evaporation and latent heat over the AS and BoB. The SST of the AS was heavily season dependent, whereas the SST of BoB remained high throughout the year.

ENSO resulted in substantial warming and cooling of the Indian Ocean. There observed an enhancement in the occurrence of El Nino and La Nina events after 1970. There was the occurrence of 3 Very Strong El Nino, 4 Strong El Nino and 2 Strong La Nina events in the interim of 1970-2020. The SST anomaly over the Indian Ocean at the time of El Nino and La Nina displayed that the SST anomaly prior to 1980 was negative, whereas later 1980, the SST anomaly was positive even during the La Nina years. The probability of occurrence of strong and very strong El Nino and La Nina years was observed to increase in the following years. The IOD also have a serious influence on the SST of the Indian Ocean. Later 1990, there was an advancement in the incidence of both Positive and Negative IOD. The SST also have a strong impact on the occurrence of the active phase of MJO. Later 1990, most of the years exhibited an enhancement in the number of active days of MJO. Climate change is one of the most alarming issues today, and it is as much as local as it is global. This results in anthropogenic global warming due to increased greenhouse gas emissions which affect the ocean and atmospheric variables that are mandatory for the formation of tropical cyclones. The increment in the GHG from 1950 as a result of human-induced emissions, culminated in the rise in SST.

The analyses concluded that there is an enhancement in the intensity of cyclones over the NIO with a slight increase in the frequency of cyclones over the AS. The depressions over the BoB had a declining trend, whereas the AS exhibited a slight increase. It was interesting to observe that the AS did not have depressions in the course of 1900-1924. The cyclonic storm has a slight decrement over the BoB, whereas the Severe Cyclonic Storm was observed to advance over both the AS and the BoB. The conditions suitable for the formation of Tropical Cyclones was examined in the interim of La Nina. The study exhibited that the maximum occurrence of the Tropical cyclone was at the time of cooccurrence of La Nina and the Negative IOD.

The study also attempted to investigate the contribution of oceanic parameters to the evolution of the surface Chla in response to the Tropical Cyclone forcing and also investigated the impact of cyclones on the primary productivity in the BoB

from 2010-2020. The analyses revealed that there is strong variability in the amplitude of chlorophyll blooms induced by Cyclone Hudhud and the Cyclone Vardah, whereas the other two cyclones presented a weak response. It was observed that the intensity of chlorophyll concentrations is independent of the intensity of the translation speed. The higher positive values of the Ekman pumping velocity is an indication of the upwelling and also results in the enhancement of the deeper waters in the cyclone track. The lower the Euphotic and nitracline depths, it was observed to be conducive for inducing stronger chlorophyll blooms under cyclone forcing. The TC contribution to primary production was found to be weak, although only the cyclone Hudhud showed a positive relationship with the cyclone intensity and primary productivity the increasing range from 410.43 to 2338.98 mg/C/m2/day.

REFERENCES

Abram, N.J., Hargreaves, J.A., Wright, N.M., Thirumalai, K., Ummenhofer, C.C., and England, M.H. 2020. Palaeoclimate perspectives on the Indian Ocean dipole. *Quat. Sci. Rev.* 237: 106302.

An, S.I. and Wang, B. 2000. Interdecadal change of the structure of the ENSO mode and its impact on the ENSO frequency. *J. Clim.* 13(12): 2044-2055.

Aneesh, S. and Sijikumar, S. 2018. Changes in the La Niña teleconnection to the Indian summer monsoon during recent period. *J. Atmos. Sol. Terr. Phys*. 167: 74-79.

Babin, S. M., Carton, J. A., Dickey, T. D., & Wiggert, J. D. (2004). Satellite evidence of hurricane-induced phytoplankton blooms in an oceanic desert. *J. Geophys. Res. Oceans*. 109(C3).

Balaguru, K., Taraphdar, S., Leung, L.R., and Foltz, G.R. 2014. Increase in the intensity of postmonsoon Bay of Bengal tropical cyclones. *Geophys. Res. Lett.* 41(10): 3594-3601.

Balaji, M., Chakraborty, A., and Mandal, M. 2018. Changes in tropical cyclone activity in North Indian Ocean during satellite era (1981–2014). *Int. J. Clim.* 38(6): 2819-2837.

Behrenfeld, M.J. and Falkowski, P.G. 1997. Photosynthetic rates derived from satellite-based chlorophyll concentration. *Limnol. Oceanogr*. *42*(1): 1-20.

Bhardwaj, P. and Singh, O. 2020. Climatological characteristics of Bay of Bengal tropical cyclones: 1972–2017. *Theor. Appl. Climatol.* 139(1): 615-629.

Bras, R.L., 1990. *Hydrology: an introduction to hydrologic science*. Addison Wesley Publishing Company, 643p.

Byju, P. and Kumar, S.P. 2011. Physical and biological response of the Arabian Sea to tropical cyclone Phyan and its implications. *Mar. Environ. Res.* 71(5): 325-330.

Cermeño, P., Dutkiewicz, S., Harris, R. P., Follows, M., Schofield, O., and Falkowski, P. G. 2008. The role of nutricline depth in regulating the ocean carbon cycle. *Proc. Natl. Acad. Sci.* 105(51): 20344-20349.

Chacko, N. 2017. Chlorophyll bloom in response to tropical cyclone Hudhud in the Bay of Bengal: Bio-Argo subsurface observations. *Deep Sea Res. Part I: Oceanogr. Res. Pap.* 124: 66-72.

Chanda, A., Das, S., Mukhopadhyay, A., Ghosh, A., Akhand, A., Ghosh, P., Ghosh, T., Mitra, D. and Hazra, S. 2018. Sea surface temperature and rainfall anomaly over the Bay of Bengal during the El Niño-Southern Oscillation and the extreme Indian Ocean Dipole events between 2002 and 2016. *Remote Sens. Appl.: Soc. Environ.* 12: 10-22.

Chen, M., Wang, W., Kumar, A., Wang, H., and Jha, B. 2012. Ocean surface impacts on the seasonal-mean precipitation over the tropical Indian Ocean. *J. Clim.* 25(10): 3566-3582.

Chow, V.T. 1964. *Handbook of Applied Hydrology*. McGraw-Hill Book Company, New York. 1495p.

Chowdary, J.S. and Gnanaseelan, C. 2007. Basin-wide warming of the Indian Ocean during El Niño and Indian Ocean dipole years. *Int. J. Climatol.* 27(11): 1421-1438.

Cyriac, A., Ghoshal, T., Shaileshbhai, P.R., and Chakraborty, A. 2016. Variability of sensible heat flux over the Bay of Bengal and its connection to Indian Ocean Dipole events. *Ocean Sci. J.* 51(1): 97-107.

Dare, R.A. and McBride, J.L. 2011. Sea surface temperature response to tropical cyclones. *Mon. Weather Rev.* 139(12): 3798-3808.

Deo, A.A., Ganer, D.W., and Nair, G. 2011. Tropical cyclone activity in global warming scenario. *Nat. Hazards*. 59(2): 771-786.

Deshpande, M., Singh, V.K., Ganadhi, M.K., Roxy, M.K., Emmanuel, R., and Kumar, U. 2021. Changing status of tropical cyclones over the north Indian Ocean. *Clim. Dyn.* 1-23.

D'Mello, J.R. and Prasanna Kumar, S. 2018. Processes controlling the accelerated warming of the Arabian Sea. *Int. J. Climatol.* 38(2): 1074-1086.

Emanuel, K. 2003. Tropical cyclones. *Annu. Rev Earth Planet Sci.* 31(1): 75-104.

Falkowski, P. G. 1994. The role of phytoplankton photosynthesis in global biogeochemical cycles. *Photosyn. Res.* 39(3): 235-258.

Frank, W.M. 1977. The structure and energetics of the tropical cyclone I. Storm structure. *Mon. Wea. Rev*, 105(1): 1119-1135.

Genner, M. J., Freer, J. J., and Rutterford, L. A. 2017. Biological responses to ocean warming. UK Government's Foresight Future of the Sea Project

Ghasemi, A.R. 2020. Influence of northwest Indian Ocean sea surface temperature and El Niño–Southern Oscillation on the winter precipitation in Iran. *J. Water Clim. Chang.* 11(4): 1481-1494.

Girishkumar, M.S. and Ravichandran, M. 2012. The influences of ENSO on tropical cyclone activity in the Bay of Bengal during October–December. *J. Geophys. Res. Oceans*. 117(C2).

Goni, G., DeMaria, M., Knaff, J., Sampson, C., Ginis, I., Bringas, F., Mavume, A., Lauer, C., Lin, I.I., Ali, M.M., and Sandery, P. 2009. Applications of satellite-derived ocean measurements to tropical cyclone intensity forecasting. *Oceanography*. 22(3): 190-197.

Hansen, J. and Sato, M. 2004. Greenhouse gas growth rates. *Proc. Natl. Acad. Sci.* 101(46): 16109-16114.

Hashimoto, T., Stedinger, J.R. and Loucks, D.P. 1982. Reliability, resiliency, and vulnerability criteria for water resource system performance evaluation. *Water Resour. Res*. *18*(1): 14-20.

Hoell, A., Funk, C., and Barlow, M. 2014. La Niña diversity and northwest Indian Ocean rim teleconnections. *Clim. Dyn.* 43(9-10): 2707-2724.

Interagency Advisory Committee on Water Data, https://acwi.gov/m9201.html

Jaswal, Ashok., Singh, Virendra., and Bhambak, S. 2012. Relationship between sea surface temperature and surface air temperature over Arabian Sea, Bay of Bengal and Indian Ocean. *J. Indian Geophys. Union*. 16: 41-53.

Jayaram, C., Bhaskar, T.U., Chacko, N., Prakash, S. and Rao, K.H. 2021. Spatio-temporal variability of chlorophyll in the northern Indian Ocean: A biogeochemical argo data perspective. *Deep Sea Res. Part II Top. Stud. Oceanogr.* 183: 104928.

Jones, C.S., Legler, D.M., and O'Brien, J.J. 1995. Variability of surface fluxes over the Indian Ocean: 1960–1989. *Global Atmos. Ocean Syst*. 3: 249-272.

Khole, M. 2003. Variability of sea surface temperature over Indian Ocean during El-Nino and La-Nina years. *Mausam*. 54(4): 829-836.

Kikuchi, K. and Wang, B. 2010. Formation of tropical cyclones in the northern Indian Ocean associated with two types of tropical intraseasonal oscillation modes. *J. Meteorol. Soc. Japan. Ser. II*. 88(3): 475-496.

Knutson, T.R., McBride, J.L., Chan, J., Emanuel, K., Holland, G., Landsea, C., Held, I., Kossin, J.P., Srivastava, A.K., and Sugi, M. 2010. Tropical cyclones and climate change. *Nat. Geosci. 3*(3): 157-163.

Krishna, K.M. 2009. Intensifying tropical cyclones over the North Indian Ocean during summer monsoon—Global warming. *Glob. Planet. Change*. 65(1-2): 12-16.

Krishnan, R., Sanjay, J., Gnanaseelan, C., Mujumdar, M., Kulkarni, A., and Chakraborty, S. 2020. *Assessment of climate change over the Indian region:*

A report of the Ministry of Earth Sciences (MOES), Government of India, Springer Nature, 226p.

Kug, J.S. and Kang, I.S. 2006. Interactive feedback between ENSO and the Indian Ocean. *J. Clim.* 19(9): 1784-1801.

Kug, J.S., An, S.I., Jin, F.F. and Kang, I.S. 2005. Preconditions for El Niño and La Niña onsets and their relation to the Indian Ocean. *Geophys. Res. Lett.* 32(5).

Kumar, P.D., Paul, Y.S., Muraleedharan, K.R., Murty, V.S.N., and Preenu, P.N. 2016. Comparison of long-term variability of Sea Surface Temperature in the Arabian Sea and Bay of Bengal. *Reg. Stud. Mar. Sci.* 3: 67-75.

Kumar, S.P., Roshin, R.P., Narvekar, J., Kumar, P.D., and Vivekanandan, E. 2009. Response of the Arabian Sea to global warming and associated regional climate shift. *Mar. Environ. Res.* 68(5): 217-222.

Kumari, P.V., Jayappa, K.S., Thomas, S., and Gupta, A. 2021. Decadal variations of sea surface temperature in the eastern Arabian Sea and its impacts on the net primary productivity. *Spatial Information Research*. 29(2): 137-148.

Kuttippurath, J., Sunanda, N., Martin, M.V., and Chakraborty, K. 2021. Tropical storms trigger phytoplankton blooms in the deserts of north Indian Ocean. *NPJ Clim. Atmos. Sci.* 4(1): 1-12.

Landsea, C.W. 2000. Climate variability of tropical cyclones: past, present and future. *Storms*. 1: 220-241.

Liang, W., Tang, D., & Luo, X. 2018. Phytoplankton size structure in the western South China Sea under the influence of a 'jet-eddy system'. *J. Mar.Syst.* 187: 82-95.

Lin, I. I. 2012. Typhoon-induced phytoplankton blooms and primary productivity increase in the western North Pacific subtropical ocean. *J. Geophys. Res. Oceans.* 117(C3).

Lin, I., Liu, W.T., Wu, C.C., Wong, G.T., Hu, C., Chen, Z., Liang, W.D., Yang, Y., and Liu, K.K. 2003. New evidence for enhanced ocean primary production triggered by tropical cyclone. *Geophys. Res. Lett.* 30(13).

Liu, Y., Tang, D., Tang, S., Morozov, E., Liang, W. and Sui, Y. 2020. A case study of Chlorophyll a response to tropical cyclone Wind Pump considering Kuroshio invasion and air-sea heat exchange. *Sci. Total Environ.* 741: 140290.

Mahala, B.K., Nayak, B.K., and Mohanty, P.K. 2015. Impacts of ENSO and IOD on tropical cyclone activity in the Bay of Bengal. *Nat. Hazards*. 75(2): 1105-1125.

Maloney, E.D. and Kiehl, J.T. 2002. MJO-related SST variations over the tropical eastern Pacific during Northern Hemisphere summer. *J. Clim.* 15(6): 675-689.

Maneesha, K., Prasad, D.H., and Patnaik, K.V.K.R.K. 2021. Biophysical responses to tropical cyclone Hudhud over the Bay of Bengal. *J. Oper. Oceanogr.* 14(2): 87-97.

Matthews, A.J. 2000. Propagation mechanisms for the Madden-Julian oscillation. *Quart. J. R. Met. Soc*. 126(569): 2637-2651.

Mays, L.W. 2001. *Water Resources Engineering.* Wiley, 761p.

Menkes, C.E., Lengaigne, M., Lévy, M., Éthé, C., Bopp, L., Aumont, O., Vincent, E., Vialard, J., and Jullien, S. 2016. Global impact of tropical cyclones on primary production. *Global Biogeochem. Cycles.* 30(5): 767-786.

Montgomery, M.T. and Farrell, B.F. 1993. Tropical cyclone formation. *J. Atmos. Sci.* 50(2): 285-310.

Murakami, H., Vecchi, G.A. and Underwood, S. 2017. Increasing frequency of extremely severe cyclonic storms over the Arabian Sea. *Nat. Clim. Chang*. 7(12): 885-889.

Nagura, M. and Konda, M., 2007. The seasonal development of an SST anomaly in the Indian Ocean and its relationship to ENSO. *J. Clim. 20*(1): 38-52.

National Oceanic and Atmospheric Administration (NOAA), Global Monitoring Laboratory Earth System Research Laboratories, https://gml.noaa.gov/aggi/

Ng Eric.K. and Chan, J.C. 2012. Interannual variations of tropical cyclone activity over the north Indian Ocean. *Int. J. Climatol.* 32(6): 819-830.

Ohba, M. and Ueda, H. 2007. An impact of SST anomalies in the Indian Ocean in acceleration of the El Niño to La Niña transition. *J. Meteorol. Soc. Japan. Ser. II*. 85(3): 335-348.

Pan, G., Chai, F., Tang, D., and Wang, D. 2017. Marine phytoplankton biomass responses to typhoon events in the South China Sea based on physical-biogeochemical model. *Ecol. Modell.* 356: 38-47.

Patra, P.K., Kumar, M.D., Mahowald, N., and Sarma, V.V.S.S. 2007. Atmospheric deposition and surface stratification as controls of contrasting chlorophyll abundance in the North Indian Ocean. *J. Geophys. Res. Oceans*. 112(C5).

Philander, S.G.H. 1983. El Nino southern oscillation phenomena. *Nature*. 302(5906): 295-301.

Qasim, S.Z. 1977. Biological productivity of the Indian Ocean. *Indian J. Mar. Sci.* 6(2): 122-137.

Rahul, S. and Gnanaseelan, C. 2012. Net heat flux over the Indian Ocean: trends, driving mechanisms, and uncertainties. *IEEE Geosci. Remote Sens. Lett.* 10(4): 776-780.

Raj Parampil, S., Bharathraj, G.N., Harrison, M., and Sengupta, D. 2016. Observed subseasonal variability of heat flux and the SST response of the tropical Indian Ocean. *J. Geophys. Res. Oceans.* 121(10): 7290-7307.

Rao, A.D., Upadhaya, P., Ali, H., Pandey, S. and Warrier, V. 2020. Coastal inundation due to tropical cyclones along the east coast of India: an influence of climate change impact. *Nat. Hazards*. 101(1): 39-57.

Rao, D.V.B., Srinivas, D., and Satyanarayana, G.C. 2019. Trends in the genesis and landfall locations of tropical cyclones over the Bay of Bengal in the current global warming era. *J. Earth Syst. Sci.* 128(7): 1-10.

Rao, K.H., Smitha, A., and Ali, M.M. 2006. A study on cyclone induced productivity in south-western Bay of Bengal during November-December 2000 using MODIS (SST and chlorophyll-a) and altimeter sea surface height observations. *Indian J. Mar. Sci*. 35(2).

Reddy, B.N.K., Venkatesan, R., Osuri, K.K., Mathew, S., Kadiyam, J., and Joseph, K.J. 2018. Comparison of AMSR-2 wind speed and sea surface temperature with moored buoy observations over the Northern Indian Ocean. *J. Earth Syst. Sci.* 127(1): 1-11.

Roxy, M.K., Dasgupta, P., McPhaden, M.J., Suematsu, T., Zhang, C., and Kim, D. 2019. Twofold expansion of the Indo-Pacific warm pool warps the MJO life cycle. *Nature*. 575(7784): 647-651.

Roy Chowdhury, R., Prasanna Kumar, S., Narvekar, J., and Chakraborty, A. 2020. Back-to-back occurrence of tropical cyclones in the Arabian Sea during October–November 2015: Causes and responses. *J. Geophys. Res. Oceans*. 125(6).

Saji, N.H. and Yamagata, T.J.C.R. 2003. Possible impacts of Indian Ocean dipole mode events on global climate. *Clim. Res*. *25*(2): 151-169.

Salas, J.D. and Obeysekera, J. 2014. Revisiting the concepts of return period and risk for nonstationary hydrologic extreme events. *J. Hydrol. Eng. 19*(3): 554-568.

Sarma, V.V.S.S., Srinivas, T.N.R., Kumari, V.R., Prasad, M.H.K., Dalabehera, H.B., Satyanarayana, U., Rao, G.D., Rao, D.B., Paul, Y.S., Murty, V.S.N.,

and Krishna, M.S. 2019. Suppressed biological production in the coastal waters off Visakhapatnam, India under the impact of the very severe cyclonic storm Hudhud. *J. Earth Syst. Sci.* 128(6): 1-11.

Sattar, A.M. and Cheung, K.K. 2019. Comparison between the active tropical cyclone seasons over the Arabian Sea and Bay of Bengal. *Int. J. Climatol*. 39(14): 5486-5502.

Sebastian, M. and Behera, M.R. 2015. Impact of SST on tropical cyclones in North Indian Ocean. *Procedia Engineering*. 116: 1072-1077.

Seelanki, V., Nigam, T., and Pant, V. 2021. Upper-ocean physical and biological features associated with Hudhud cyclone: A bio-physical modelling study. *J. Mar. Syst.* 215: p103499.

Shenoi, S.S.C., Shankar, D., and Shetye, S.R., 2002. Differences in heat budgets of the near-surface Arabian Sea and Bay of Bengal: Implications for the summer monsoon. *J. Geophys. Res. Oceans*. 107(C6): 5-1.

Singh, K., Panda, J., Sahoo, M., and Mohapatra, M. 2019. Variability in tropical cyclone climatology over North Indian Ocean during the period 1891 to 2015. *Asia-Pac. J. Atmos. Sci.* 55(2): 269-287.

Singh, P., Chowdary, J.S., and Gnanaseelan, C. 2013. Impact of prolonged La Niña events on the Indian Ocean with a special emphasis on southwest Tropical Indian Ocean SST. *Glob and Planet Change*. 100: 28-37.

Singh, O.P. 2007. Long-term trends in the frequency of severe cyclones of Bay of Bengal: observations and simulations. *Mausam*. 58(1): 59-66.

Singh, O.P., Khan, T.A., and Rahman, M.S. 2000. Changes in the frequency of tropical cyclones over the North Indian Ocean. *Meteorol. Atmosph. Phys.* 75(1): 11-20.

Singh, V.K. and Roxy, M.K. 2020. A review of the ocean-atmosphere interactions during tropical cyclones in the north Indian Ocean. *arXiv preprint arXiv:2012.04384*.

Stedinger, J.R., Vogel, R.M. and Foufoula-Georgious, E. 1993. *Frequency Analysis of Extreme Events in Handbook of Hydrology*. McGraw-Hill, New York.

Sukresno, B. 2010. Empirical orthogonal functions (EOF) analysis of SST variability in Indonesian water concerning with ENSO and IOD. *International Archives of the Photogrammetry, Remote Sensing and Spatial Information Science Journal*. 38(8): 116-121.

Tomita, H. and Kubota, M. 2004. Variability of surface heat flux over the Indian Ocean. *Atmos. Ocean*. 42(3): 183-199.

Trenberth, K.E. 2011. Changes in precipitation with climate change. *Clim. Res.* 47(1-2): 123-138.

Tsuboi, A. and Takemi, T. 2014. The interannual relationship between MJO activity and tropical cyclone genesis in the Indian Ocean. *Geosci. Lett.* 1(1): 1-6.

Vidya, P.J. and Das, S. 2017. Contrasting Chl-a responses to the tropical cyclones Thane and Phailin in the Bay of Bengal. *J. Mar. Syst.* 165: 103-114.

Viessman, W. and Lewis. G. 2003. *Introduction to hydrology*. Pearson Education Inc., New York, 612p.

Wahiduzzaman, M., Oliver, E.C., Wotherspoon, S.J., and Luo, J.J. 2020. Seasonal forecasting of tropical cyclones in the North Indian Ocean region: The role of El Niño-Southern Oscillation. *Clim. Dyn.* 54(3): 1571-1589.

Wood, K.M., Klotzbach, P.J., Collins, J.M., Caron, L.P., Truchelut, R.E., and Schreck, C.J. 2020. Factors affecting the 2019 Atlantic hurricane season and the role of the Indian Ocean Dipole. *Geophys. Res. Lett.* 47(13).

Xu, H., Tang, D., Liu, Y. and Li, Y., 2019. Dissolved oxygen responses to tropical cyclones" Wind Pump" on pre-existing cyclonic and anticyclonic eddies in the Bay of Bengal. *Mar. Pollut. Bull.* 146: 838-847.

Yadav, S.S. and Gjerde, K.M. 2020. The ocean, climate change and resilience: Making ocean areas beyond national jurisdiction more resilient to climate change and other anthropogenic activities. *Mar. Policy*. 122: 104184.

Ye, H., Kalhoro, M.A., Sun, J., and Tang, D. 2018. Chlorophyll blooms induced by tropical cyclone Vardah in the Bay of Bengal. *Indian J. Mar. Sci.* 47(7): 1383-1390.

Yeh, S.W., Cai, W., Min, S.K., McPhaden, M.J., Dommenget, D., Dewitte, B., Collins, M., Ashok, K., An, S.I., Yim, B.Y., and Kug, J.S. 2018. ENSO atmospheric teleconnections and their response to greenhouse gas forcing. *Reviews of Geophysics*, (1): 185-206.

Yoo, S.H., Yang, S., and Ho, C.H. 2005. Variability of the Indian Ocean SST and Its Impacts on Asian-Australian Monsoon Climate. *J. Geophys. Res.* 111(D3).

Yu, L., Jin, X. and Weller, R.A., 2006. Role of net surface heat flux in seasonal variations of sea surface temperature in the tropical Atlantic Ocean. *Journal of Climate*, 19(23), pp.6153-6169.

Yu, L., Jin, X. and Weller, R.A. 2007. Annual, seasonal, and interannual variability of air–sea heat fluxes in the Indian Ocean. *J. Clim.* 20(13): 3190-3209.

Yu, L., Wen, J., Chang, C.Y., Frankenberg, C. and Sun, Y. 2019. High-resolution global contiguous SIF of OCO-2. *Geophys. Res. Lett*. *46*(3): 1449-1458.

Yuan, J. and Cao, J. 2013. North Indian Ocean tropical cyclone activities influenced by the Indian Ocean Dipole mode. *Sci. China Earth Sci.* 56(5): 855-865.

Zhang, C. 2013. Madden–Julian oscillation: Bridging weather and climate. *Bull. Am. Meteorol. Soc.* 94(12): 1849-1870.

Zhang, G.J. and Mcphaden, M.J. 1995. The relationship between sea surface temperature and latent heat flux in the equatorial Pacific. *J. Clim.* 8(3): 589-605.

Zhao, H., and Wang, Y. 2018. Phytoplankton increases induced by tropical cyclones in the South China Sea during 1998–2015. *J. Geophys. Res. Oceans*. 123(4): 2903-2920.

ABSTRACT

Tropical Cyclone is one of the extreme natural events, which is a low-pressure system over tropical or subtropical waters with organized convection and definite cyclonic circulation. The Northern Indian Ocean is separated into two basins by the Indian Subcontinent landmass: the Arabian Sea and the Bay of Bengal. The objectives of the study were to analyze the long-term variability of SST, cyclogenesis, and their intensification, along with their association with ENSO and IOD events and to analyze the biological production by virtue of Tropical Cyclones over the Arabian Sea and Bay of Bengal. The SST and the frequency and intensity of cyclones over the Indian Ocean were analyzed for a period of 120 years (1900-2020) and the effect of severe cyclones Hudhud, Vardah, Gaja and Fani on biological production were studied. The SST over the Northern Indian Ocean had an increasing trend with the highest SST over the BoB and more pronounced warming over the AS. The enhancement in SST was by reason of fluctuations in wind, evaporation, heat flux, humidity and precipitation. The frequency of the Tropical Cyclones was greatest over the Bay of Bengal with an increase in the intensity of cyclones over the years with a decrease in the appearance of less intense storms, while the Arabian Sea exhibited an enhancement in both frequency and intensity of cyclones. The analyses identified an enhancement in the occurrence of strong ENSO events later 1970 along with an increment in the co-occurrence of ENSO and IOD events. The development of Tropical Cyclones was identified to be the highest at the time of cooccurrence of La Nina and Negative IOD. The Cyclone Hudhud and Vardah presented an elevated Chlorophyll concentration, while the Cyclone Fani and Gaja was not much conducive for the enhanced biological production.